



NTNU – Trondheim
Norwegian University of
Science and Technology

Speeding up SURF Imaging

New Methods to Increase Frame Rate in
Multi-Pulse Ultrasound Imaging Modalities

Ola Finneng Myhre

Master of Science in Electronics

Submission date: September 2013

Supervisor: Lars Magne Lundheim, IET

Co-supervisor: Bjørn Atle Johan Angelsen, ISB

Norwegian University of Science and Technology
Department of Electronics and Telecommunications

Problem Description

The ability of medical ultrasonography to convey images of anatomical structures to clinicians in real-time is one of its most powerful and important characteristics. Real-time, non-invasive observation of organs facilitates quick and accurate diagnosis of patients. However, when imaging deep anatomical structures, the frame rate of conventional ultrasound may drop below 30 Hz, causing movement on the screen of the instrument to seem choppy to the user. If the number of acquisitions required to create each image is increased, the frame rate may become as low as 10 Hz or less, and the real-time characteristic of the imaging system is lost.

Another major concern for clinicians that use ultrasound is image quality. The image quality of conventional ultrasound is limited by the presence of multiple scattering artefacts, or reverberations. The presence of reverberations can destroy the contrast resolution of an imaging system, and generally becomes more pronounced in patients with thick body walls with a higher percentage of fat. In cardiac diagnostics, this has provoked the development of an invasive, more time-consuming and expensive imaging method which images the heart by inserting an ultrasound transducer into the oesophagus of the patient. A new technique called second order ultrasound field (SURF) imaging shows promise in improving ultrasound contrast resolution without having to be invasive.

SURF imaging uses at least twice as many acquisitions to create an image, compared to conventional imaging. This means that the maximum frame rate of a SURF system is lower than that of a conventional system. There is thus a trade-off between contrast resolution and frame-rate. This thesis discusses new methods that may be used to increase the frame rate of SURF imaging, so that SURF imaging achieves better contrast resolution while preserving frame rate and real-time characteristics.

Assignment given: February 18th, 2013
Supervisors: Professor Bjørn Angelsen
Professor Lars Lundheim

Abstract

Any good medical ultrasound imaging system must be able to resolve anatomical structures properly, and simultaneously provide adequate frame rate so that moving structures can be studied with ease. In a conventional imaging system these properties are related by a trade-off, but is it possible to have one and the other by applying more advanced post-processing to acquired RF data? Two new methods, beam RF interpolation (BRI) and beam delay interpolation (BDI), are presented to solve this trade-off issue, using the SURF imaging technique to improve contrast resolution, and the new methods to increase frame rate. *In vitro* data was acquired using a standard imaging phantom, and a modified SURF imaging system, and processing of the data was done off-line. The results show that the new methods have potential to contribute to increasing frame rate and contrast resolution, but hardware issues necessitate verification of the results using different equipment.

Sammendrag

Ethvert godt system for medisinsk ultralydavgivning må kunne gjengi anatomiske strukturer korrekt og samtidig gi tilstrekkelig bildefrekvens slik at bevegelig anatomi kan studeres. I et vanlig system må man foreta et kompromiss slik at man enten får god bildekvalitet eller høy bildefrekvens, men er det mulig å få begge deler ved å bruke mer avansert post-prosessering på innhentet RF data? To nye metoder, stråleinterpolasjon (BRI) og stråleforsinkelseinterpolasjon (BDI), blir presentert for å løse dette avveingsproblemet. Ved hjelp av SURF avbildningsteknikken kan man bedre bildekvaliteten, og ved hjelp av nye metodene kan man samtidig bevare bildefrekvensen. *In vitro* data ble hentet inn ved hjelp av et standard avbildningsfantom, og et modifisert SURF avbildningssystem. Prosessering av innhentet data ble gjort i ettetid. Resultatene viser at de nye metodene har potensiale til å bidra til å bevare bildefrekvens samtidig som bildekvaliteten bedre, men problemer med hardware i avbildningssystemet gjør det nødvendig at resultatene verifiseres med annet utstyr.

Preface

It is my impression that large projects, more often than not, tend to get side-tracked. Particularly when the people involved have little experience, or there is little managerial oversight. Unfortunately, the following project was no exception.

Initially, the task seemed simple; to modify an already functional ultrasound scanner to make it work with a new, also seemingly functional, ultrasound transducer. The system could then be used to study a new technique that could potentially speed up data acquisition. By really applying myself, I might even have gotten the technique to work in real-time on the scanner within the five months that the project as this was supposed to last. And who knows what may have been, had it not been for the first point in that list of todo's.

It would not be proper to use this space to complain about all of the things that went wrong and seemed to be conspiring in order to regularly make this period of my life miserable. Suffice to say, the signal processing that was to be the centrepeice of this thesis, did not get the amount of time or attention that is was supposed to.

For in retrospect, I am grateful for the uphill battle. I have learned so much more about engineering from the practical exercise that these last months turned out to be, than I would have, given some ordinary, theoretical problem to solve. I have learned volumes about software; from syntax to system structure, about hardware; from design to experimental testing, and about the practical problem solving in the lab; with its frustrations and near magic highs. This project has made me realize that, even though my certificate may say otherwise, I know that my education to become an engineer has only just begun, and will probably never end.

Acknowledgements

First of all, I would like to thank Professor Bjørn Angelsen for allowing me to work on this project. Although it had proven at times to be frustrating and even sleep-depriving, it has left me with an understanding of ultrasound theory, processing and instrumentation which I would not be without. I would also like to thank my supervisor, Professor Lars Lundheim for his concrete feedback on the text and for being a fine benchmark on which to test language and readability. Without his help, I fear that the text would have been unbearable to read. Thank God we moved so much of it into the appendices!

I have been fortunate enough to be able to receive help from researchers and engineers with invaluable knowledge about the SURF technology; thank you, Laurens, Tonni, Thor-Andreas, Ole Martin, Johannes, and Tollef, for our discussions and your help.

I would also like to thank my close friends; Christina, Elisabeth, Fride, Geir and Simon for your patience, support, and friendship. I apologize for my incessant moping and moaning, and promise to repay you in full. Preferably in alcohol. Seriously; I really could not have managed without you.

I am also very grateful to the Student Society in Trondheim and all the people I have worked with and befriended there, for allowing me to take part in so much adventure, and making my time in Trondheim that much more eventful and memorable.

At the risk of being profoundly cheesy, I have to thank my late father. Without having him as an inspiration, I do not think that I ever would have entered the field of engineering, or medical technology. His untimely death has given me the determination to devote my life to cripple the disease that killed him.

Finally; my mother. Words are simply not enough.

Contents

Problem Description	i
Abstract	iii
Sammendrag	v
Preface	vii
Acknowledgements	ix
1 Introduction & Background	1
1.1 Echocardiography	1
1.1.1 Transthoracic Echocardiography (TTE)	2
1.1.2 Transesophageal Echocardiography (TEE)	4
1.2 Pulse-echo Imaging	5
1.2.1 Backscatter Imaging	5
1.2.2 Multiple Scattering	6
1.3 Tissue Harmonic Imaging	7
1.4 SURF Imaging	8
1.5 Thesis Contribution	8
1.6 Thesis Outline	9

2	Theory & Background	11
2.1	Non-Linear Waves in Heterogeneous Media	12
2.2	Dual-Band Pulse Complexes	14
2.3	Non-linear Interaction Effects	17
2.3.1	Non-linear Propagation Delay	17
2.3.2	Non-linear PFD	19
2.3.3	Non-linear PFM	19
2.4	Geometrical Effects	20
2.4.1	SURF Aberration	20
2.4.2	Focus-dependent Phase Relation	20
2.5	Scattering	21
2.5.1	First Order Scattering	23
2.5.2	Third Order Scattering	24
3	Processing	27
3.1	Pulse Reverberation	29
3.2	Estimation of Non-Linear Propagation Delay (NPD)	31
3.3	Estimation of First and Third Order Delays	33
3.4	Beam Interpolation Scheme	34
3.4.1	Beam RF Interpolation (BRI)	35
3.4.2	Beam Delay Interpolation (BDI)	37
3.5	Reverberation Suppression	39
4	Phantom Recordings	41
4.1	The CIRS Phantom	43
4.2	Signal Envelope	45
4.3	Signal Envelope after Noise Suppression	48

5 Discussion	51
5.1 Effects of Hardware Malfunction	51
5.2 Interpolation Method Quality	52
5.3 Practical Experiences	54
5.4 Conclusions	54
5.5 Future Work	54

Appendices

A Imaging System	71
A.1 Hardware	71
A.2 Skolmen	73
A.2.1 Transducer stack	73
A.2.2 Specifications and Acoustic	77
A.3 Software	77
A.3.1 The Sonix Imaging Software	78
A.3.2 The SURF Library	78
B Skolmen Design Specification	81
B.1 Design Specifications	81
B.2 Electro-acoustic Transfer Functions	82
B.3 Electrical Characteristics	82
B.4 Diffraction Foci	85
C XML Documentation	87
C.1 Sonix	87
C.1.1 Probes.xml	87
C.1.2 GEN-General	89
C.2 SURF	93
C.2.1 Probe.xml	93
C.2.2 Applications.xml	95
C.2.3 Application files	96

D Imaging Parameters	99
E Software Adjustments	103
E.1 Geometrybase	103
E.2 Beamformer	106
E.3 LF Pulser Driver	110
F Measurement Parameters	111
F.1 2D Pressure Measurement	111
F.2 Phantom Recordings	112
G Measurements	115
G.1 Equipment List	116
G.2 LF Pulser Voltage	117
G.3 2D Near-Field Pressure	119
G.3.1 Measuring the HF and LF near-field	120
G.3.2 The Influence of Non-linear Effects	121
G.4 Verification of Pulse Forms	125
G.5 Experiments on Array Function	126
G.5.1 Persuing the Elements	127
G.5.2 Purging the Pulser	130
G.5.3 LF Cross Coupling	131
G.5.4 Concluding Remarks	133
H Additional Measurements	135
H.1 Wave Front Curvatures	135
H.2 LF RMS Pressure Profiles	137

List of Figures

1.1	Example sector scan images	3
2.1	Dual-band pulse complexes	14
2.2	LF pressure affecting HF pulse forms	18
2.3	Illustration of first and third order scattering.	22
3.1	Block diagram of processing chain	28
3.2	Non-linear propagation delay simulation	33
3.3	The CIPLSE block diagram.	33
3.4	BRI schematic	37
3.5	BDI schematic	39
4.1	CIRS phantom schematic	44
4.2	BRI envelope, line density 64	46
4.3	BRI envelope, line density 128	46
4.4	BDI envelope, line density 64	47
4.5	BDI envelope, line density 128	47
4.6	BRI suppression, line density 64	49
4.7	BRI suppression, line density 128	49
4.8	BDI suppression, line density 64	50
4.9	BDI suppression, line density 128	50

A.1	A schematic overview of the hardware components in the dual-band imaging system.	72
A.2	Dual-band transducer stacks	73
A.3	<i>Skolmen</i> transfer functions – Pulsar voltage to surface vibration velocity	76
A.4	Beam form in LF pulser memory	79
B.1	Transfer function of elements of the HF array in <i>Skolmen</i>	83
B.2	Transfer function of elements of the LF array in <i>Skolmen</i>	83
B.3	Estimated mean input impedance of the HF elements in <i>Skolmen</i>	84
B.4	Estimated mean input impedance of the LF elements in <i>Skolmen</i>	84
G.1	LF near-field spatio-temporal peak pressure amplitude	117
G.2	LF element efficiency	118
G.3	Minimum maximum imaging depth	119
G.4	12 dB beam profiles of closely spaced elements	120
G.5	Measured and simulated RMS beam profiles of the HF array	122
G.6	Measured and simulated RMS beam profiles of the LF array	123
G.7	Measured HF pulse in the near field of the transducer	125
G.8	Measured LF pulse in the near field of the transducer	125
G.9	Measured HF pressure spectrum	126
G.10	Measured LF pressure spectrum	126
G.11	LF RMS Pressure and wave front curvature	127
G.12	LF channel voltages, simultaneous excitation	128
G.13	LF channel voltages, individual excitation	129
G.14	Individual LF element profiles, azimuth	130
G.15	Probe housing cross-coupling circuit diagram	132
G.16	Illustration of array elements	133
H.1	HF wave front curvatures	136

H.2	LF wave front curvatures	136
H.3	The beam profiles of the LF array, at a depth of 0 mm	138
H.4	The beam profiles of the LF array, at a depth of 20 mm	138
H.5	The beam profiles of the LF array, at a depth of 40 mm	138

List of Tables

4.1	Interpolation performance	43
A.1	Description of terms in impedance formulae	75
A.2	Description of important Sonix imaging parameters used in the text.	78
B.1	Design specifications of <i>Skolmen</i>	82
B.2	The proposed stack design for <i>Skolmen</i>	85
B.3	<i>Skolmen</i> diffraction focusing depths	85
D.1	SURF mode transmission parameters.	100
D.2	SURF mode processing parameters.	101
D.3	SURF parameters supplied by Sonix.	102
G.1	2D near-field measurement grid specification.	121
G.2	LF intra-array DC resistance	132

Nomenclature

β_n	The non-linearity parameter of a material
κ	The compressibility of a material
$\nu(\mathbf{r}_s)$	The backscattering coefficient at \mathbf{r}
$\phi(\mathbf{r}, t)$	The acoustic momentum potential at a point \mathbf{r} at a time t
ρ	The mass density of a material
$\tau(\mathbf{r})$	Non-linear propagation delay of the high frequency wave in a SURF complex
$\zeta(\mathbf{r})$	The relative variation in the non-linearity parameter in a heterogeneous medium
$\psi(\mathbf{r}, t)$	The displacement of a particle relative to the point \mathbf{r} , at a time t .
$\mathbf{a}(\mathbf{r}, t)$	The acceleration of a particle with an equilibrium position at \mathbf{r} , at a time t .
$\mathbf{u}(\mathbf{r}, t)$	The velocity of a particle with an equilibrium position at \mathbf{r} , at a time t .
c_0	The average propagation velocity of a sound wave in a heterogeneous medium
$p(\mathbf{r}, t)$	The pressure in the point \mathbf{r} , at the time t
AED	Average envelope deviation
AMI	Acute myocardial infarction
BDI	Beam Delay Interpolation
CIPLSE	Constrained Incremental Polynomial Least Squares Estimator
HF	High Frequency
ISB	Department of Circulation and Medical Imaging

LA	Left atrium
LF	Low Frequency
LV	Left ventricle
NPD	Non-linear propagation delay
PFD	Pulse form distortion
PFM	Pulse form modification
PI	Pulse inversion
RBI	Beam RF Interpolation
RPM	Radial pulse modulation
SED	Standard envelope deviation
SNR	Signal-to-noise ratio
SURF	Second order ultrasound field
TEE	Transesophageal echocardiography
TGC	Time gain compensation
TTE	Transthoracic Echocardiography
USCA	Ultrasound Contrast Agent

Introduction & Background

The main topic of this thesis is the application of two new techniques which may be utilised to speed up data acquisition in ultrasound imaging. One of the methods, previously unpublished, is specific to the second order ultrasound field (SURF) imaging technique, which has been developed by Professor Angelsen's group at the department of Circulation and Medical Imaging (ISB), the Faculty of Medicine (DMF), the Norwegian University of Science and Technology (NTNU). The new techniques are motivated by the low frame rate in cardiac imaging, and the low sensitivity of the imaging modality to certain cardiac ailments, particularly when imaging the heart non-invasively through the chest wall.

The text will cover the acoustic theory of non-linear ultrasound, and the expansion of this theory to describe the SURF imaging method. It also describes two new techniques that can be used to speed up data acquisition, and presents results from using these methods on *in vitro* data.

During the work, there were significant issues with the equipment that was used to acquire data. Pin-pointing the problem proved to be less trivial than anticipated, and there is therefore a large appendix consisting of hardware and software documentation, including performance tests, and the end of the text. Firstly, however; an introduction to the exciting field of ultrasound imaging, and the tricky business of properly capturing the heart.

1.1 Echocardiography

From *The Free Dictionary* [1], ultrasound imaging of the heart, *echocardiography*, has the following definition:

"Echocardiography is a diagnostic test that uses ultrasound waves to create an image of the heart muscle. Ultrasound waves that rebound

or echo off the heart can show the size, shape, and movement of the heart's valves and chambers as well as the flow of blood through the heart. Echocardiography may show such abnormalities as poorly functioning heart valves or damage to the heart tissue from a past heart attack."

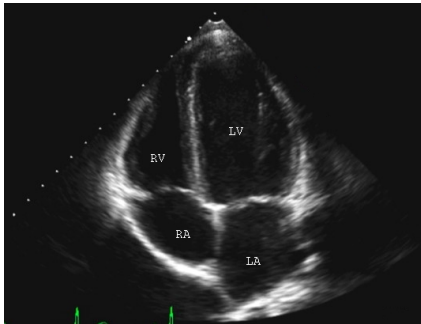
There are two main imaging methods that are used to image the heart; transthoracic echocardiography (TTE) and transesophageal echocardiography (TEE). The techniques have different advantages and limitations that are of interest to understand the motivation of the present thesis. However, the field of echocardiography as a diagnostic tool is huge, and reviewing the capabilities of the two methods for all applications is beyond the scope of this text. For a more general overview of the applications of the two techniques, the papers by Matsuzaki et al. [2] and Hillis and Bloomfield [3] can be recommended as starting points.

The following sections will focus on the difference in performance between TTE and TEE when imaging certain structures in the heart. The SURF imaging method has potential to improve the diagnostic yield when imaging these structures, and particularly in detecting the presence of thrombus in the left ventricular apex.

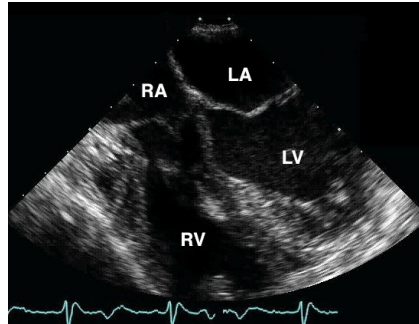
1.1.1 Transthoracic Echocardiography (TTE)

Transthoracic echocardiography is a method of ultrasound imaging that visualizes the heart of a patient, by transmitting and receiving sound waves through the chest, or *thorax*, of the patient. It is a non-invasive technique that uses phased array ultrasound transducers with transmit and receive beams that are typically electronically steered to collect data at multiple angle increments within a sector with a typical opening angle of 90° . Such an image is often referred to as a sector scan, and a typical example of such a scan is shown in Fig. 1.1a.

The application of TTE to detect for instance abnormal masses in the apical region of the left ventricle (LV) [4–9], or mitral valve prolapse [10] began to gather clinical momentum in the late 1970s and early 1980s. The studies on the technique that were made in this period reported that it exhibited excellent sensitivity and specificity in these applications. However, as pointed out by Stratton et al. [7], the technique had limitations because of the presence of image artefacts resulting from multiple scattering from the transducer, the chest wall of the patients, or from areas of dense tissue in the myocardium of the patients. To diagnose valvular defects or apical masses, it was advantageous for clinicians to assess the structures of the heart and its chambers from several points of view. Regardless of these limitations, TTE quickly became and remains the preferred method of cardiologists to detect left ventricular thrombi [11].



(a) A transthoracic sector scan. This view is known as an apical four chamber view. Source: <http://med.stanford.edu/criticalcare/fellowships/ultrasound.html>.



(b) A transesophageal sector scan. This view is known as a midesophageal four chamber view. Source: http://depts.washington.edu/anesth/education/community/tee/tee_2008_2.shtml. Image reprinted by courtesy of Donald Oxorn, MD, University of Washington Department of Anesthesiology & Pain Medicine, Seattle, WA, 2013.

Figure 1.1: Example sector scan images of a human heart, taken with phased array transducers. The probe is located at the right angle at the top of the image. Visible in both the images are; **LV**, the left ventricle; **LA**, the left atrium; **RV**, the right ventricle; and **RA**: the right atrium. Additionally, one can clearly see the mitral and tricuspid valves, the septum and the myocardium. Note the position of the anatomy relative to the transducer position; the images have been obtained in opposite directions. The images were selected for the thesis because of their high fidelity.

New studies conducted since the turn of the millennium have revealed that TTE often lacks sensitivity to ventricular masses when ultrasound contrast agents are not used to help delineate them [12–16]. Although the specifics pertaining to the imaging methods are somewhat poorly documented in these studies, discussions by Thanigaraj et al. [12] and Mansencal et al. [14] suggest that the suboptimal sensitivity of TTE could be attributed to the presence of multiple scattering artefacts in the apical region of the LV. In fact, 28 out of 48 patients that were suspected of having LV thrombus after TTE examination in the study by Thanigaraj et al. [12] turned out to be falsely positive due to imaging artefacts.

By applying a venous injection of ultrasound contrast agent the sensitivity of TTE can be increased, but, as pointed out by Mansencal et al. [14], systematic use of such agents can result in large cost implication. Prevalence of acute myocardial infarction (AMI) in the United States of America alone is 1.2 million [17] and in the literature it is widely accepted that the presence of LV thrombus in patients having suffered AMI should be investigated, as these masses are a frequent complication associated with AMI. The application of contrast agents in these examinations would increase the overall treatment cost.

1.1.2 Transesophageal Echocardiography (TEE)

Transesophageal echocardiography is an invasive imaging technique which takes advantage of the close posterior proximity of the heart to the oesophagus. By inserting a tube with an attached array transducer into the oesophagus of a patient, the transducer will be able to transmit sound waves through the oesophagus and into the heart. As the transmitted sound only passes through a small amount of tissue before reaching the heart, multiple scattering effects are less pronounced in this imaging modality compared to TTE. Furthermore, the limited transmission distance reduces the amount of absorption that the wave is subjected to, which in turn allows for utilisation of higher frequencies, and the modality can thus produce images with higher resolution compared to that of TTE.

Two-dimensional TEE was first introduced in the early 1980s in papers by Hisanaga et al. [18, 19], Rajagopalan et al. [20] and Souquet et al. [21]. Initial testing of imaging on patients was subsequently done by Schlüter et al. [22], with concluding expectations that the technique would provide increased sensitivity to atrial defects relating to thrombi, the septum, and valvular structures. Throughout the following decade many studies evaluated the performance of TTE and TEE and it was reported that TEE outperformed TTE in locating small LV thrombi [23], valvular vegetation [24], left atrial (LA) thrombi [24, 25], the left atrial appendage (LAA) with thrombi [24, 26–29], LA spontaneous echo contrast (SEC) [24, 27, 29, 30], atrial septal aneurysms (ASA) [24, 25, 29, 31], and mitral (MV) and tricuspid (TV) valvular prolapses and myxoma [24, 25, 28, 30, 31]. Including doppler and contrast agent modes, many of the studies also found that TEE was more sensitive to detecting a patent foramen ovale (PFO) in both orientations.

The transesophageal method thus provides superior image quality in a number of situations, but, setting image quality aside, there are aspects that make the use of TEE less preferable in clinical situations. Firstly, TEE is an invasive technique, which requires consent from the patient before use. Furthermore, the procedure of swallowing the probe may be uncomfortable for patients, and is frequently precluded by a period of fasting and administration of local anaesthesia.

Although TEE generally is capable of providing better quality sonograms of the heart than TTE, the apical region of the left ventricle can be a challenge for both techniques. TTE has issues with multiple scattering artefacts, whereas attenuation and diffraction tend to reduce image quality when using TEE. Obtaining better image quality in the left ventricular apex is one of the challenges addressed by the methods of this thesis.

1.2 Pulse-echo Imaging

In ultrasound imaging, the main technique for observing anatomical structures is pulse-echo imaging. Sound beams are transmitted consecutively in different directions, and the echoes which are produced as the sound wave travels through a medium of continuously varying density and compressibility, give the information that is used to produce images.

The sound wave emitted from a transducer is usually focused at a certain depth, either by mechanically or electronically steered focusing. As the transducer receives echoes, it is made most sensitive to the region from which the echo is emanating at a given time, *i.e.* its focus varies with time, following the propagation of the transmitted wave. This technique is called dynamic focusing and can only be achieved by administering different time delays to individual elements on electronically steered arrays of transducers. By focusing in this manner, the beam width at each depth is reduced to a minimum, producing the best possible resolution in the entire image.

Using non-invasive probes to obtain images presents issues with focusing of the ultrasonic beams. Large tissue inhomogeneity in the body wall cause the wave front of the pulse to be distorted, due to the variation in propagation velocity and interference from multiple scattering between the layers in the body wall. These effects are known as phase front aberration, and reverberation artefacts, respectively, and can generate a lot of noise in ultrasound images.

1.2.1 Backscatter Imaging

The basic assumptions in pulse-echo measurements are that range and time are related by the average sound velocity, c , in the tissue and that the sound waves scatter only once as they propagate through the tissue. Thus, it can be assumed

that an echo arriving from a scatterer at a certain distance, r_x , will be incident on the transducer at a time, t_x , after it was initially transmitted. Since the wave must travel from the transducer to the scatterer and back again, the two quantities are related by

$$t_x = \frac{2r_x}{c} \quad (1.1)$$

The second assumption is more complex in mathematical terms, but the concept is simple; a wave that originates from a scatterer as a result of the transmitted wave passing it by, does not interact with the inhomogeneity of the medium. Alternatively, the scattered waves that are produced by its interaction with the medium are so insignificant that they can be omitted from further considerations. This is called the Born approximation [32], after the Nobel laureate Max Born, and can be expressed in terms of the acoustic momentum potential ϕ as

$$\phi_B(\mathbf{r}, \omega) = \phi_i(\mathbf{r}, \omega) + \iiint_V g(\mathbf{r} - \mathbf{r}_0, \omega) \{k_\omega^2 \beta(\mathbf{r}_0) \phi_i(\mathbf{r}_0, \omega) - \nabla_0 [\gamma(\mathbf{r}_0) \nabla_0 \phi_i(\mathbf{r}_0, \omega)]\} d\mathbf{r}_0 \quad (1.2)$$

In this expression, which springs out from Huygens' principle and the Rayleigh-Sommerfeld diffraction integral, the integral term represents all the scattered waves in the volume V that result from insonifying the tissue with an incident wave, $\phi_i(\mathbf{r}, \omega)$. The total field is thus the sum of the incident field and the scattered waves. The integral term is a convolution in space between a spherically expanding wave, known as a Green's function, $g(\mathbf{r}, \omega)$, and the scattered wave at each point in space. $k_\omega = 2\pi/\lambda$, where λ is the wave length, is the wave number of the incident wave, and ω is the angular frequency. The vector $\mathbf{r} = [x, y, z]$ denotes an observation point in space, whereas the vector $\mathbf{r}_0 = [x_0, y_0, z_0]$ is the convolution parameter, iterating over all points in the volume V . $\nabla_0 = [\partial/\partial x_0, \partial/\partial y_0, \partial/\partial z_0]$ denotes the spatial gradient with respect to \mathbf{r}_0 . The scattering occurs due to the interaction between the incident wave and the relative fluctuations in compressibility $\beta(\mathbf{r})$ and mass density $\gamma(\mathbf{r})$, and the resulting scattered field is the sum of these interactions. A more compact notation is

$$\phi_B(\mathbf{r}, \omega) = \phi_i(\mathbf{r}, \omega) + \phi_{s1}(\mathbf{r}, \omega) \quad (1.3)$$

where the subscript of the last term denotes that the scattered field is of the first order.

1.2.2 Multiple Scattering

Although the Born approximation and range-time relations provide fair approximations of the acoustic fields and echoes in pulse-echo imaging, they remain approximations and assumptions, and do not hold in some situations. In patients with large inhomogeneous regions in the body wall, for instance, the assumptions fail. When the imaging system uses these assumptions, this failure appears as

noise in the image, creating ambiguity as to whether displayed shapes are related to anatomy or no more than noise artefacts.

The reason for this image corruption is that scattered waves contribute to the total acoustic field and should not be neglected as in the Born approximation. The exact calculation of the total field is similar to the integral equation of Eq. (1.2), excepting that the expression for the total momentum potential field must be used in the integral of the equation. Since the integral operator is linear, the solution for the total field can be written

$$\phi(\mathbf{r}, \omega) = \phi_i(\mathbf{r}, \omega) + \sum_{j=1}^{\infty} \phi_j^s(\mathbf{r}, \omega) \quad (1.4)$$

where $\phi_j^s(\mathbf{r}, \omega) = S(\phi_{j-1}^s(\mathbf{r}, \omega))$, $\phi_0^s(\mathbf{r}, \omega) = \phi_i(\mathbf{r}, \omega)$, and $S(\cdot)$ is the scattering integral of Eq. (1.2).

When transmitting an ultrasound beam, the transmitted wave will travel mainly in the forward direction so the first order backscattered waves will be directed backwards towards the transducer. These reflections will thus be observed by the system. The second order reflections will travel in the same direction as the transmitted beam and will not be directly observed. However, the scattering of these waves, the third order scattering, will travel back towards the transducer. A pulse-echo imaging system will thus only observe odd order scattering. This is detailed further in Sec. 2.5.

The combination of signal components from various odd orders of scattering is what produces the unwanted reverberation noise. The most dominant of these components is the one stemming from third order scattering, and this thesis is mainly focused on the effects of this scattering, and how to suppress it.

1.3 Tissue Harmonic Imaging

The suppression of reverberation noise in ultrasound imaging has been an area of research since the 1980's and remains one of the challenges facing the development in ultrasound today. Currently, the most common method for suppressing reverberation noise is tissue harmonic imaging, which exploits the non-linear distortion of transmit pulses as they propagate into tissue [33–36]. This effect occurs due to the non-linear elasticity of the tissue and is cumulative as the pulse travels deeper into the tissue [37–39]. Scattered waves are not distorted by non-linear propagation since the pressure amplitudes of these waves are small enough that propagation is strictly linear. However, the distortion that has accumulated in the transmitted pulse in its flight from the transducer to a given scatterer will determine the shape of the scattered wave. Thus, one can determine from which depth a scattered wave has emanated by examining the form of the received wave. Non-linear propagation produces second harmonic signal components in

the transmitted pulse, so in practice harmonic imaging uses a band pass filter to examine the second harmonic signal components of the received signal, and produce an image. At a given depth, signal components from third order scattering will have a smaller amount of second harmonic frequency components than signal components from first order scattering. Thus, harmonic imaging reduces the effect of reverberation noise on image quality.

1.4 SURF Imaging

Second order ultrasound field (SURF) imaging, or radial pulse modulation (RPM) is a technique that was developed at the Department of Circulation and Medical Imaging (ISB), NTNU, to improve contrast resolution when using ultrasound contrast agents. The technique is based on transmitting a low frequency (LF) wave at 0.2 MHz to 1.2 MHz and a high frequency (HF) wave at 1.0 MHz to 10.0 MHz, simultaneously. The LF wave is used to manipulate the material in which the waves are propagating, and the HF pulse is an imaging pulse, similar to those used in conventional ultrasound imaging. The LF pulse in effect changes the ambient pressure in which the HF pulse is travelling, causing the medium to behave differently, depending on whether the LF pressure is negative or positive, and depending on its amplitude. The technique aims to utilise the non-linear character of tissue to improve image quality. The acoustic theory on which the technique is based will be detailed in Ch. 2.

Exploiting the advantages and tackling the challenges of SURF imaging are areas of ongoing research at ISB. The technique has the potential to increase contrast resolution in contrast enhanced ultrasound by manipulating contrast agent sizes and resonance frequencies [40]. It can also be utilized in order to suppress pulse reverberations, which is the application which will receive the most attention in this thesis.

1.5 Thesis Contribution

In order to use SURF imaging to suppress reverberation noise, one must transmit two pulse complexes in each imaging direction. The technique is thus similar to pulse inversion (PI). Increasing the amount of transmitted pulses means that the achievable frame rate is reduced, thereby deteriorating the real-time characteristic which makes ultrasound such a preferred imaging modality. Obtaining images in real-time is particularly important in cardiac ultrasound, in order to capture the natural movement of cardiac structures. Unfortunately, echocardiography has a required maximum imaging depth of around 15 cm, which means that low frame rate quickly can become an issue. Doubling acquisition time in echocardiography is therefore particularly destructive to real-time observation.

This thesis focuses on how to utilize the SURF technique in applications where the imaging depth is large, and frame rate is a concern. One solution to maintaining high frame rate with SURF imaging could be by interpolating data acquired by transmitting in two or more directions to create artificial image data. By halving the amount of imaging directions, frame rate could be preserved in SURF imaging.

Two new methods for interpolating spatially sparsely sampled data are presented and compared. Their performance is measured by comparison to regularly acquired data.

By increasing the frame rate of SURF imaging, it could be possible to increase the contrast resolution of transthoracic echocardiography, in particular in the region surrounding the left ventricular apex, thereby reducing the need for examinations with its more invasive and expensive transesophageal counterpart.

1.6 Thesis Outline

Chapter 2 will outline the acoustic theory that is fundamental for SURF imaging and processing

Chapter 3 will explain the processing that is used in SURF imaging, and present new methods to increase data acquisition.

Chapter 4 presents the results that were obtained by applying the new methods to acquired *in vitro* data

Chapter 5 discusses the results and points to future work.

Appendices A–B contain information on the imaging system used to acquire data.

Appendices C–F contain software modifications and documentation of parameters that are used by the imaging system.

Appendices G–H document the various measurements that were made to verify the function of the imaging system.

Theory & Background

To describe the effects of radial pulse modulation, the wave equation for non-linear bulk compression waves is convenient to begin with as a theoretical basis. Some excellent texts on the subject include books by Angelsen [41], Cobbold [42], Hamilton and Blackstock [43], and Naugolnykh and Ostrovsky [44]. The following sections will outline the theory into which these texts delve so deeply, attempting to leave the reader with enough theoretical background to understand the following chapters, while avoiding more confusing or unnecessarily detailed information on the subject of non-linear wave propagation.

Initially, the quadric approximation to the non-linear wave equation for inhomogeneous media will be presented, before the effects of propagating two pulses together in a single pulse complex are summarized. Mathematical models of linear and non-linear scattering, and the phenomenon of pulse reverberation, or multiple scattering, are described. Methods that may be used to suppress multiple scattering artefacts while conserving scattering of the first order will be presented, along with some methods to speed up data acquisition for said methods.

The derivations and descriptions in the following sections are based on a Lagrangian coordinate system, as opposed to an Euler description, and mostly follows Angelsen [41]. The Lagrangian system is based on relating the displacement of a particle in space to an equilibrium position, *i.e.* to the position that the particle would relax to, were there no forces acting upon it. This relaxed position is denoted by the vector \mathbf{r} . The displacement of the particle at \mathbf{r} at a time t , can be expressed as a vector $\psi(\mathbf{r}, t)$, and its velocity and acceleration vectors can consequently be written as

$$\mathbf{u}(\mathbf{r}, t) = \frac{\partial \psi(\mathbf{r}, t)}{\partial t} \quad \mathbf{a}(\mathbf{r}, t) = \frac{\partial \mathbf{u}(\mathbf{r}, t)}{\partial t} = \frac{\partial^2 \psi(\mathbf{r}, t)}{\partial t^2} \quad (2.1)$$

The use of Lagrangian coordinates thus simplifies the expression of velocity and acceleration vectors, compared to the Eulerian alternative. Furthermore, since

there is no net transport of mass by a traveling wave, and the particles which interact in the wave oscillate around equilibrium positions, the Lagrangian description is well suited to describe wave propagation.

2.1 Non-Linear Waves in Heterogeneous Media

When dealing with ultrasonic imaging beams, a plane wave approximation of wave propagation is reasonable. The transmitted waves travel in one main propagation direction with relatively smooth phase fronts, so that transverse particle displacement is negligible.

Writing in terms of Lagrangian particle displacement, $\psi(\mathbf{r}, t)$, and pressure $p(\mathbf{r}, t)$, Newton's second law can be approximated as[45, 46]

$$-\nabla p(\mathbf{r}, t) = \rho \frac{\partial^2 \psi(\mathbf{r}, t)}{\partial t^2}, \quad (2.2)$$

and when considering a second order approximation, the constitutive material equation for a non-linear, isotropic medium can be written[46, pp. 12.21]

$$-\nabla \psi(\mathbf{r}, t) = (1 - \beta_n \kappa p(\mathbf{r}, t)) \kappa p(\mathbf{r}, t) + h_{ab}(t) \underset{t}{*} \kappa p(\mathbf{r}, t), \quad (2.3)$$

where the asterisk denotes a convolution in time, so that

$$h_{ab}(t) \underset{t}{*} \kappa p(\mathbf{r}, t) = \kappa \int_{-\infty}^{\infty} h_{ab}(\tau) p(\mathbf{r}, t - \tau) d\tau \quad (2.4)$$

In these two equations, p is the pressure on a small volume, ΔV , ρ is the mass density within that volume, and ψ describes the displacement of particles on its surface. The function h_{ab} describes the absorption in the medium within the volume, the parameter κ describes the linear compressibility of the material, and $\beta_n = 1 + B/2A$ describes its non-linear elasticity.

The equations in Eq. (2.2) and (2.3) can be combined to express the second order non-linear wave equation with absorption. To do this, it is advantageous to separate the material parameters into slowly varying and rapidly fluctuating terms, so that

$$\rho(\mathbf{r}) = \rho_a + \rho_f(\mathbf{r}) \quad (2.5)$$

$$\kappa(\mathbf{r}) = \kappa_a + \kappa_f(\mathbf{r}) \quad (2.6)$$

$$\beta_n(\mathbf{r}) = \beta_{na} + \beta_{nf}(\mathbf{r}) \quad (2.7)$$

where the subscripts a and f denote average values and fast variations, respectively. Assuming that shear stresses can be neglected so that the pressure, $p(\mathbf{r}, t)$ and the acoustic momentum potential, $\phi(\mathbf{r}, t)$ can be related as[45, pp. 4.10]

$$p(\mathbf{r}, t) = \frac{\partial \phi(\mathbf{r}, t)}{\partial t} \quad (2.8)$$

writing the relative variations mass density as $\gamma(\mathbf{r}) = \rho_f(\mathbf{r})/\rho_a$, and noting that

$$\frac{1}{\rho} = \frac{1}{\rho_a} - \frac{\gamma(\mathbf{r})}{\rho_a} \quad (2.9)$$

a non-linear wave equation of the second order can be expressed for the acoustic momentum potential of the field in an ultrasonic beam, in a heterogeneous, absorbing medium. To simplify notation, the independent field variables \mathbf{r} and t have been omitted from the expression for the wave equation. In the following equation $\phi = \phi(\mathbf{r}, t)$, $\gamma = \gamma(\mathbf{r})$, $\beta = \beta(\mathbf{r})$, $\beta_{nf} = \beta_{nf}(\mathbf{r})$, and $h_{ab} = h_{ab}(t)$. By letting $\kappa_f^2 \rightarrow 0$, the wave equation can be written

$$\begin{aligned} \nabla^2 \phi - \frac{1}{c_0^2} \frac{\partial^2 \phi}{\partial t^2} - h_{ab} * \frac{1}{c_0^2} \frac{\partial^2 \phi}{\partial t^2} &= \frac{\beta}{c_0^2} \left(\frac{\partial^2 \phi}{\partial t^2} + h_{ab} * \frac{\partial^2 \phi}{\partial t^2} \right) + \\ \nabla(\gamma \nabla \phi) - \frac{2\sigma_{na}}{c_0^2} [(1 + 2\beta)(1 + \varsigma)] &\frac{\partial \phi}{\partial t} \frac{\partial^2 \phi}{\partial t^2} \end{aligned} \quad (2.10)$$

where $\varsigma = \varsigma(\mathbf{r}) = \beta_{nf}(\mathbf{r})/\beta_{na}$. A similar equation, where $\kappa_f^2 \neq 0$ has been derived by Hansen et al. [47]. By noting that the convolution term on the right hand side of the equation is negligible in magnitude compared to the non-absorbed scattering term, and differentiating the entire equation with respect to time, a wave equation for the pressure field can be formulated as shown for instance by Angelsen [46, pp. 12.40, eq. 12.144]

$$\underbrace{\nabla^2 p - \frac{1}{c_0^2} \frac{\partial^2 p}{\partial t^2}}_{\text{Linear propagation terms}} - \underbrace{h_{ab} * \frac{1}{c_0^2} \frac{\partial^2 p}{\partial t^2}}_{\text{Linear absorption terms}} = \underbrace{\frac{\beta}{c_0^2} \frac{\partial^2 p}{\partial t^2} + \nabla(\gamma \nabla p)}_{\text{Linear scattering terms}} - \underbrace{\frac{\sigma_{na} + \sigma_{nf}}{c_0^2} \frac{\partial^2 p^2}{\partial t^2}}_{\text{Non-linear propagation \& scattering terms}} \quad (2.11)$$

where $\sigma_{nf} = \sigma_{nf}(\mathbf{r}) = \sigma_{na} [2\beta(\mathbf{r}) + (1 + 2\beta(\mathbf{r}))\varsigma(\mathbf{r})]$. The scattering of the quadric term of the wave equation is separated into a parameter describing the average non-linearity of the propagation $\sigma_{na}(\mathbf{r})$, and a parameter describing the rapid variations of the non-linear scattering in the tissue, $\sigma_{nf}(\mathbf{r})$. The decomposition of the non-linear material parameters makes it possible to separate cumulative forward propagation distortion and local non-linear scattering. The effects are approximately described by the average, and the rapidly varying non-linear scattering term, respectively.

2.2 Dual-Band Pulse Complexes

Having derived the non-linear wave equation for a pressure field in Eq. (2.11), it can now be examined when the pressure field is constituted by two separate fields, as is the case in SURF imaging.

The pulses constituting the complex should have center frequencies satisfying a ratio of $\sim 1:7$ to $\sim 1:10$. By satisfying this requirement one can to some extent avoid detrimental effects of co-propagation, such as pulse form distortion (PFD) and the introduction of frequencies resulting from non-linear interaction between the low frequency (LF) and high frequency (HF) fields. These effects will be elaborated on in Sec. 2.3.

The low frequency manipulation pulse is used to manipulate the elasticity of the medium, and the high frequency observation pulse is used to observe the parameters of the medium. The scattering of the observation pulse in the medium will be dependent on the pressure and polarity of the manipulation pulse, as well as the pulses' relative position in the propagating complex. Examples of such complexes are shown in Fig. 2.1, where Gaussian pulses have been used to illustrate the concept.

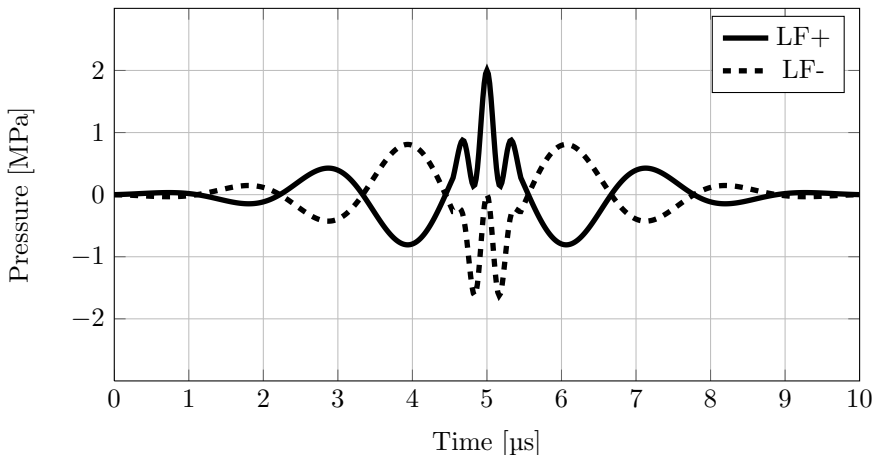


Figure 2.1: Dual-band pulse complexes with different LF polarity, using gaussian pulses. The centre frequencies of the LF and HF pulses are 0.45 MHz and 2.75 MHz, respectively. The amplitude of each pulse in the complex is 1 MPa.

Typically, for instance when imaging ultrasound contrast agents in contrast enhanced ultrasound (CEUS) imaging, two pulse complexes are transmitted along each image line, and the received signals are subtracted to isolate the non-linear propagation and scattering, which is strong from contrast agents [40, 48, 49]. A similar subtraction technique can be used to characterize and suppress reverber-

ation noise from multiple scattering [50, 51] in ordinary tissue modalities like brightness (B-mode) or motion (M-mode) mode.

Analysing the field that results from transmitting multiple complexes reveals that the propagation velocity of the HF pulse is dependent on the pressure of the co-propagating LF pulse, and that various distortion effects will shape the HF pulse as it travels through tissue.

By writing the pressure field of the pulse complex as a sum of the LF and HF pressure fields, $p(\mathbf{r}, t) = p_L(\mathbf{r}, t) + p_H(\mathbf{r}, t)$, and inserting into the wave equation of Eq. (2.11), the total field can be expressed as

$$\begin{aligned} \nabla^2 p_H - \frac{1}{c_0^2} \frac{\partial^2 p_H}{\partial t^2} - h_{ab} \ast_t \frac{1}{c_0^2} \frac{\partial^2 p_H}{\partial t^2} + \nabla^2 p_L - \frac{1}{c_0^2} \frac{\partial^2 p_L}{\partial t^2} - h_{ab} \ast_t \frac{1}{c_0^2} \frac{\partial^2 p_L}{\partial t^2} = \\ \frac{\beta}{c_0^2} \frac{\partial^2 p_H}{\partial t^2} + \nabla(\gamma \nabla p_H) + \frac{\beta}{c_0^2} \frac{\partial^2 p_L}{\partial t^2} + \nabla(\gamma \nabla p_L) - \\ \frac{\sigma_{na} + \sigma_{nf}}{c_0^2} \left[\frac{\partial^2 p_H^2}{\partial t^2} - 2 \frac{\partial^2 (p_L p_H)}{\partial t^2} + \frac{\partial^2 p_L^2}{\partial t^2} \right] \quad (2.12) \end{aligned}$$

Fortunately, this equation can be simplified, since the main point of interest is the propagation of the observation pulse, and the effect that the manipulation pulse has on it. The differentiation of the pressure in time implies that linear scattering is proportional to the squared frequency of the incident pressure wave, so with adequate frequency separation of the pulses in the complex the linear scattering of the HF pulse is two orders of magnitude larger than that of the LF pulse. In other terms

$$\nabla(\gamma \nabla p_H) \gg \nabla(\gamma \nabla p_L) \quad (2.13)$$

$$\frac{\beta}{c_0^2} \frac{\partial^2 p_H}{\partial t^2} \gg \frac{\beta}{c_0^2} \frac{\partial^2 p_L}{\partial t^2} \quad (2.14)$$

$$\frac{\sigma_{nf}}{c_0^2} \frac{\partial^2 p_H^2}{\partial t^2} \gg \frac{\sigma_{nf}}{c_0^2} \frac{\partial^2 p_L^2}{\partial t^2} \quad (2.15)$$

As stated in the end of Sec. 2.1, the average non-linear material parameter describes the cumulative distortion of the wave as it travels through the medium. The amount of distortion in the wave is related to the wavelength of the wave. Waves with larger wavelength will have larger distances separating the peaks and troughs of the wave from its zero-crossings, hence the peaks use a longer propagation distance to "catch up" to the zero-crossings. Similarly, it will take a longer propagation distance for the zero-crossings to "catch up" to the troughs of the wave. The propagation distance required to achieve acoustic shock is thus

proportional to the wavelength of the propagating wave [37]. Therefore, the effect of non-linear propagation distortion is negligible on the LF wave since it typically only propagates a limited amount of wavelengths into the tissue. Thus

$$\frac{\sigma_{na}}{c_0^2} \frac{\partial^2 p_L^2}{\partial t^2} \approx 0 \quad (2.16)$$

However, the HF wave travels a larger amount of wavelengths over the same distance as the LF pulse, so the effect of forward non-linear distortion becomes apparent. This distortion attenuates the fundamental band of the HF pulse, as it produces second-harmonic frequency components in the travelling wave. This term must thus remain in the wave equation.

The non-linear terms describing the interaction between the two constituents of the pulse complex can be approximated by assuming that the time derivative of the manipulation pulse is too small in the region of the observation pulse that it can be neglected, *i.e.*

$$\frac{\partial^2 (p_L p_H)}{\partial t^2} \approx p_L \frac{\partial^2 p_H}{\partial t^2} \quad (2.17)$$

With these considerations, the wave equation of Eq. (2.12) can be approximated as

$$\begin{aligned} \nabla^2 p - \frac{1}{c_0^2} \frac{\partial^2 p_L}{\partial t^2} - \frac{1}{c^2(p_L)} \frac{\partial^2 p_H}{\partial t^2} - h_{ab} \ast_t \frac{1}{c_0^2} \frac{\partial^2 p}{\partial t^2} + \frac{\sigma_{na}}{c_0^2} \frac{\partial^2 p_H^2}{\partial t^2} = \\ \frac{\beta - 2\sigma_{nf} p_L}{c_0^2} \frac{\partial^2 p_H}{\partial t^2} + \nabla(\gamma \nabla p_H) - \frac{\sigma_{nf}}{c_0^2} \frac{\partial^2 p_H^2}{\partial t^2} \end{aligned} \quad (2.18)$$

where $c^2(p_L) = c_0^2 (1 + 2\sigma_{na} p_L)$, as shown by Angelsen and Hansen [52] and by Angelsen and Tangen [53]. The propagation is thus directly dependent on the pressure of the low frequency wave. Physically, the manipulation pulse compresses or relaxes the material as the HF propagates through it, depending on where the HF pulse is located in relation to the LF pulse. As the material is compressed or relaxed, the material parameters are modified, causing the propagation velocity of the HF wave to increase or decrease, respectively.

The modification of the propagation velocity of the observation pulse can be used in reverberation suppression by assuming that the effect only occurs along the trajectory of the transmitted beam. After the wave is scattered the LF pressure is so low, due to the low magnitude of scattering, that its manipulation of the HF wave is considered to be negligible. The significance of this will be detailed further in the following sections.

2.3 Non-linear Interaction Effects

The SURF technique, which was detailed in Sec. 2.2, introduces non-linear interaction effects between the HF imaging pulse and the LF manipulation pulse. The HF pulse will be modified as the pulse complex propagates and the modulation is composed of the following effects.

- Non-linear propagation delay
- Non-linear pulse form distortion (PFD)
- Non-linear pulse form modification (PFM)

The following sections will detail the mechanisms that cause these effects to occur and the effect that they have on the imaging system.

2.3.1 Non-linear Propagation Delay

In Sec. 2.2, it was shown in Eq. (2.18) that the propagation velocity, c , of the HF wave is dependent on the local LF pressure, p_L where the HF wave is located, through the relation

$$c^2(\mathbf{r}, p_L(\mathbf{r})) = c_0^2 (1 + 2\sigma_{na}(\mathbf{r})p_L(\mathbf{r})) \quad (2.19)$$

which can be approximated by Taylor expansion so that

$$c(\mathbf{r}, p_L(\mathbf{r})) \approx c_0 (1 + \sigma_{na}(\mathbf{r})p_L(\mathbf{r})) \quad (2.20)$$

By assuming that the wavelength of the LF pulse is sufficiently large compared to the wavelength of the HF pulse, and that the HF pulse is centred in a peak compression or rarefaction of the LF wave, the HF pulse will propagate with approximately constant LF pressure. Angelsen and Tangen [53] use the LF pressure at the centre of gravity of the HF pulse to calculate an estimated non-linear propagation delay along HF pulse trajectories $\Gamma(\mathbf{r})$ that are orthogonal to the HF wave-fronts so that the time of flight for the HF pulse to a point in space \mathbf{r} , can be expressed as

$$t(\mathbf{r}) = \int_{\Gamma(\mathbf{r})} \frac{1}{c(\mathbf{s}, p_L)} d\mathbf{s} \quad (2.21)$$

$$t(\mathbf{r}) \approx \int_{\Gamma(\mathbf{r})} \frac{1}{c_0} d\mathbf{s} - \int_{\Gamma(\mathbf{r})} \frac{\sigma_{na}(\mathbf{s})p_L(\mathbf{s})}{c_0} d\mathbf{s} \quad (2.22)$$

where the relation $1/(1 + \sigma_{na}(\mathbf{r})p_L(\mathbf{r})) \approx (1 - \sigma_{na}(\mathbf{r})p_L(\mathbf{r}))$ has been used, since $|\sigma_{na}(\mathbf{r})p_L(\mathbf{r})| \ll 1$.

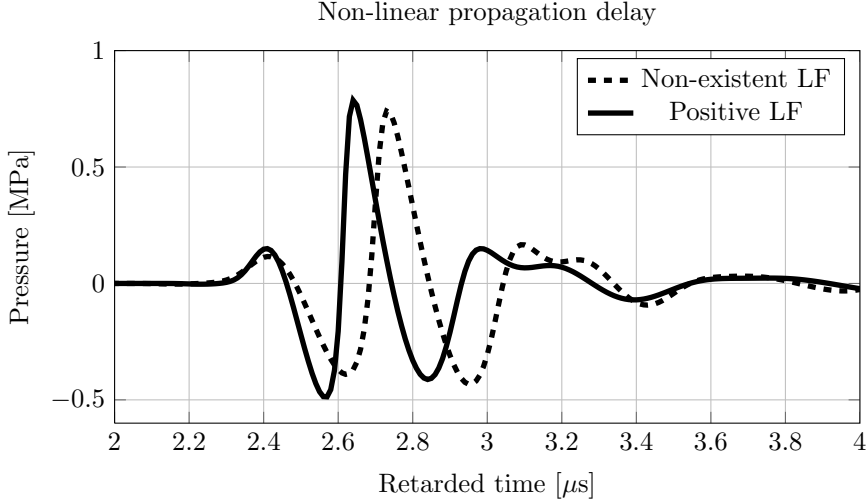


Figure 2.2: The simulated pulse forms of a HF pulse, with and without the presence of an LF pulse, at the focus of a transducer. Simulations were carried out using a probe simulator, *xTrans*[54], and a non-linear acoustic field simulator, *WaveSim*[55, 56]. The arrival time of the HF pulse changes when the LF pressure is applied, and the pulse form is also distorted.

The approximation of the propagation velocity of the HF wave in the pulse complex from Eq. (2.20) thus enables the separation of the integral in Eq. (2.22), so that the propagation time, $t(\mathbf{r})$, of a non-linearly propagating HF pulse in a SURF complex is related to the propagation time, $t_0(\mathbf{r})$, of a linearly propagating HF wave with no co-propagating LF wave via a *non-linear propagation delay* (NPD), $\tau(\mathbf{r})$, so that

$$t(\mathbf{r}) \approx t_0(\mathbf{r}) + \tau(\mathbf{r}) \quad (2.23)$$

$$t_0(\mathbf{r}) = \int_{\Gamma(\mathbf{r})} \frac{1}{c_0} d\mathbf{s} \quad (2.24)$$

$$\tau(\mathbf{r}) = - \int_{\Gamma(\mathbf{r})} \frac{\sigma_{na}(\mathbf{s}) p_L(\mathbf{s})}{c_0} d\mathbf{s} \quad (2.25)$$

By changing the polarity of the LF pressure, *i.e.* by placing the HF pulse in a rarefaction phase of the LF rather than a compression phase, the propagation delay will change from a negative to a positive value, indicating that the HF pulse propagates slower when propagating in LF rarefaction, and faster when propagating in LF compression, as expected.

2.3.2 Non-linear PFD

Although the assumption that the LF pulse amplitude is negligibly variant over the HF pulse provides a good approximation of how much the HF pulse is delayed as it propagates with the LF pulse, omitting the variation completely oversimplifies the physical situation. Since the LF pressure does in fact vary over the HF pulse, different parts of the HF pulse will experience different LF pressure as the complex propagates. Thus, the propagation velocity of the HF wave will be variant over the pulse length due to the slow variation of LF pressure along the pulse.

If the HF pressure amplitude is large, the variation in HF pressure will further complicate the situation, since the wave velocity becomes influenced by changes in HF pressure. This effect, combined with the effect of the LF pressure variation along the HF pulse will contribute to non-linear pulse form distortion (PFD). The situation is illustrated in Fig. 2.2.

2.3.3 Non-linear PFM

The pressure pulse form at a point in space is not only dependent on propagation along a single one-dimensional path from the source to the observation point, rather it is the result of an interference between waves propagating in from an infinite amount of point sources constituting the source. This is a well established concept in linear acoustics by Huygens' principle the Hemholtz-Kirchhoff integral theorem. The LF pressure along the trajectory from each point source to the observation point will determine the non-linear propagation delay of the pulse radiated by each point source. If there are variations in the pressure amplitude along the different point source trajectories, the waves from the points sources will interfere differently at the observation point due to inter-trajectory variations in non-linear propagation delay.

In ultrasound, applying different delays to different elements of an array transducer is a well known and widely used tool to focus the sound beam transmitted by the transducer [57]. Hence, introducing variation in non-linear propagation delay via transversally variant LF pressure implies that the focus of the beam will be modified. This effect is termed *pulse form modification*, and is an important consideration when designing LF transmit beams. Generally, to avoid these effects, the LF array is not focused so that an approximative plane LF wave propagates with the HF pulse. In the near-field of the transducer, the LF pressure will be highly variant transversally to the propagation direction, due to physical characteristics of the near-field [58]. This is an effect that is difficult to rectify without building very large transducers, but due to the accumulative nature of non-linear propagation delay, and the limited length of the LF near-field, other aberration effects are more dominant.

2.4 Geometrical Effects

In addition to the non-linear effects of Sec. 2.3, the transmitted pressure field is affected by the choice of beams in both the arrays. As discussed previously, the transmitted HF pulse is dependent on the LF pressure amplitude, and its transversal variation over the HF pulse. Therefore, the use of different focal points for the two arrays will result in what is termed *SURF aberration*.

The choice of transmit beams will not only determine the amount of SURF aberration on the HF wave, but will also affect the development of non-linear propagation delay. This occurs due to the frequency-dependent phase shift which occurs as the wave approaches the focal region, or the far-field, of the array.

2.4.1 SURF Aberration

The presence of PFM in the transmitted beam was shown to be dependent on the transversal variation in LF pressure in Sec. 2.3. An additional effect which modifies HF beam is the transversal variation in phase relation between the HF and the LF pulse. The variation will modify the LF pressure that is observed by the HF pulse, causing beam aberration due to transversally variant non-linear propagation delay. Additionally, the PFD, being dependent on the rapid variation in LF pressure over the temporal length of the HF pulse, will vary transversally to the propagation direction.

2.4.2 Focus-dependent Phase Relation

Another important geometrical effect in SURF imaging is the phase shift that occurs at the focus of an ultrasound beam. In the focus, one can use the Fraunhofer approximation to describe the field, which is well known in linear acoustic theory, and particularly important in ultrasound [45]. By describing the field using a free-space Green's function, in the focus of a transducer in a rigid baffle, one can find that the pressure is

$$p(\mathbf{r}, \omega) = -\frac{\rho U_F(\mathbf{r})}{2\pi|\mathbf{r}|} j\omega F(\omega) e^{ik|\mathbf{r}|} \quad (2.26)$$

where p is the pressure, ρ is the mass density of the medium, ω is the angular frequency, k is the wave number, \mathbf{r} is a point in space, and F is the spectrum of the time variation in the vibration of the transducer surface. U_F is defined as the spatial integral of the normal vibration velocity U_n over the surface of the transducer, S_t :

$$U_F(\mathbf{r}) = \int_{S_t} U_n(\mathbf{r}_0) e^{-j\frac{k}{|\mathbf{r}|}} d\mathbf{r}_0 \quad (2.27)$$

The 90 degree phase shift, represented in the expression by j , is independent of frequency. In the time domain, this means that the phase relation between a HF wave and a LF wave will be different in the focus than at the surface of the transducer, and the difference will be expressed by the periods of the waves: $\Delta t_p = (T_{HF} - T_{LF})/4$. This means that if the HF pulse is placed on the peak of the LF pulse at the transducer surface, it will, by the time it reaches the focus of the LF array, be displaced so that it is SURFing on the flank of the LF pulse. This situation yields non-linearity in the NPD, as well as inducing more PFD from the LF manipulation. Therefore, to obtain the most linear development of NPD, the effect of initial phase relation between the HF and LF pulses must be studied. This relation is dependent on each set of transmit foci, and the only way to find the ideal set-up is via simulations of the non-linear wave equation. Thus, the task of optimizing the phase relation can be a time-consuming one.

2.5 Scattering

Scattering of the ultrasound beam occurs due to variations in material parameters in the material in which the wave is propagating. It can be shown that linearly scattered plane waves can be decomposed into a monopole and a dipole components [57, pp. 7.63]. The monopole component arises from spatial variation of the compressibility of the material, whereas the dipole component is related to the spatial variation in mass density. In normal pulse echo imaging, the difference in the magnitude of these components determines the received signal. Inclusion of non-linear compressibility adds another monopole component to the scattered signal.

As a wave travels through a medium, variation in the material parameters of the medium produce reflected and refracted waves. In an inhomogeneous material like tissue, scattering occurs at all points in the medium, and yet the Born approximation only factors in the first reflection in the calculation of the received signal. The approximation is an expression for the first order reflected field, *i.e.* a field consisting of contributions from waves that have only been scattered once. In reality, the total field created by an incident beam is the sum of contributions from all fields that are scattered indefinitely, as shown with Eq. (1.4).

In ultrasound, the sound waves that are transmitted are relatively invariant transversally to the propagation direction and the relative variations of material parameters in tissue are small, so little refraction of the beam occurs. The transmitted sound wave travels away from the transducer, and the first order reflected waves travel back towards the transducer, and are detected. Similarly, the main direction of propagation of second order reflections is away from the transducer, and third order reflections propagate towards the transducer, and are detected. This is illustrated in Fig. 2.3, where the transducer itself has been used as the second scatterer.

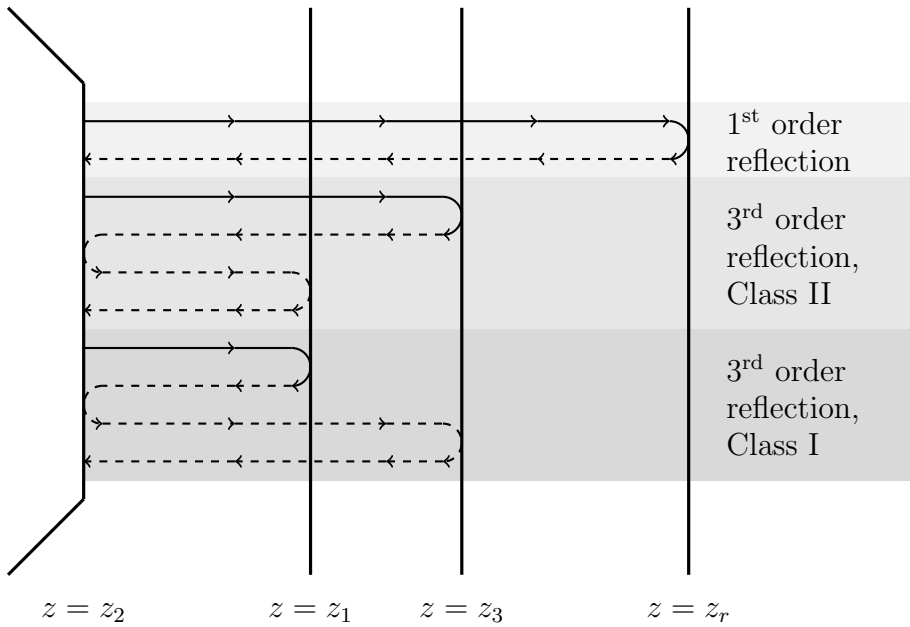


Figure 2.3: Singular and multiple scattering from strong reflecting planes. The transducer is illustrated to the left, and the waves are reflected by four scattering planes, including the transducer. Third order scattering paths where the second scatterer is not the transducer are not shown. Signal from all three scattering paths are observed at the time $t = 2z_r/c$.

The figure shows a one-dimensional illustration of first and third order scattering, and differentiates between two types of third order scattering; Class I and Class II, which will be detailed in Sec. 2.5.2. The following sections will develop mathematical models for first and third order scattering when a dual-band pulse complex propagates through a non-linear medium.

2.5.1 First Order Scattering

In Sec. 1.2, the Born approximation in Eq. (1.2) shows the expression for the first order linearly scattered momentum potential field from a volume of scatterers. This equation can be rewritten by collecting all the terms containing expression for the high frequency pressure pulse and rewriting the first order scattered field with a source term from Eq. (2.18)

$$s(\mathbf{r}, t) = \frac{\beta - 2\sigma_{nf}p_{Li}(\mathbf{r}, t)}{c_0^2} \frac{\partial^2 p_{Hi}(\mathbf{r}, t)}{\partial t^2} + \nabla (\gamma \nabla p_{Hi}(\mathbf{r}, t)) - \frac{\sigma_n}{c_0^2} \frac{\partial^2 p_{Hi}^2(\mathbf{r}, t)}{\partial t^2} \quad (2.28)$$

where the i subscript in the expressions of the HF and LF pressure fields indicates that they are incident, transmitted fields. Using the relation between pressure and momentum potential from Eq. (2.8), and writing in terms of the pressure fields, the integral representing the scattered field in Eq. (1.2) becomes

$$p_{s1}^n(\mathbf{r}, t) = \int_{-\infty}^{\infty} \int_V g(\mathbf{r}, \mathbf{r}_0, t - t_0) \left\{ \frac{\beta(\mathbf{r}_0) - 2\sigma_{nf}(\mathbf{r}_0)p_{Li}(\mathbf{r}_0, t_0)}{c_0^2} \frac{\partial^2 p_{Hi}(\mathbf{r}_0, t_0)}{\partial t_0^2} + \nabla_0 (\gamma(\mathbf{r}_0) \nabla_0 p_{Hi}(\mathbf{r}_0, t_0)) - \frac{\sigma_n(\mathbf{r}_0)}{c_0^2} \frac{\partial^2 p_{Hi}^2(\mathbf{r}_0, t_0)}{\partial t_0^2} \right\} d\mathbf{r}_0 dt_0 \quad (2.29)$$

where the superscript n has been added to highlight that non-linear scattering is included in the scattered field. By assuming that the interaction between the non-linear components of the incident wave and the non-linear scattering parameters, is weak compared to the other interactions, the final term in the integral can be neglected. By Fourier transform, the expression of the scattered signal becomes

$$P_{s1}^n(\mathbf{r}, \omega) = S(P_{Hi}(\mathbf{r}, \omega)) \quad (2.30)$$

$$P_{s1}^n(\mathbf{r}, \omega) = - \int_V G(\mathbf{r}, \mathbf{r}_0, \omega) \{ \beta(\mathbf{r}_0) k_\omega^2 P_{Hi}(\mathbf{r}_0, \omega) - \nabla_0 (\gamma(\mathbf{r}_0) \nabla_0 P_{Hi}(\mathbf{r}_0, \omega)) + 2\sigma_{nf} k_\omega^2 P_{Li}(\mathbf{r}_0, \omega) * P_{Hi}(\mathbf{r}_0, \omega) \} d\mathbf{r}_0 \quad (2.31)$$

Now, excluding the variation of the LF pulse in the area where the HF pulse is propagating, the convolution term in the integral can be neglected since the bandwidth of the LF pressure pulse becomes so small compared to that of the HF pressure. In other words, it is assumed that the main interaction between the LF pulse and the HF pulse is through the average value of the LF pressure over the region of the HF pulse, as discussed in Sec. 2.3.

Following the points of the discussion in Angelsen [57], and writing the incident pressure as the product of the spatial frequency response of the transmitting transducer, $H_t(\mathbf{r}, \omega, \mathbf{r}_t)$, a filter describing the non-linear pulse form distortion and delay of the pulse, $V_p(\mathbf{r}, \omega, p_L)$, and the frequency spectrum of the HF pressure pulse at the transmit transducer surface $P_t(\omega)$, the field at a point \mathbf{r} in space, from a point scatterer at \mathbf{r}_s , can be written as

$$dP_p(\mathbf{r}, \omega, \mathbf{r}_s) = dP_{pl}(\mathbf{r}, \omega, \mathbf{r}_s) + dP_{pn}(\mathbf{r}, \omega, \mathbf{r}_s) \quad (2.32)$$

$$dP_{pl}(\mathbf{r}, \omega, \mathbf{r}_s) = -jk_\omega^3 G(\mathbf{r}, \mathbf{r}_s, \omega) P_t(\omega) H_t(\mathbf{r}_s, \omega, \mathbf{r}_t) V_p(\mathbf{r}_s, \omega, p_L) \nu(\mathbf{r}_s) d\mathbf{r}_s \quad (2.33)$$

$$dP_{pn}(\mathbf{r}, \omega, \mathbf{r}_s) = -jk_\omega^3 G(\mathbf{r}, \mathbf{r}_s, \omega) P_t(\omega) H_t(\mathbf{r}_s, \omega, \mathbf{r}_t) V_p(\mathbf{r}_s, \omega, p_L) \\ \times 2p_L(\mathbf{r}_s) \sigma_{nf}(\mathbf{r}_s) d\mathbf{r}_s \quad (2.34)$$

where the definition of the spatial frequency response in linear acoustics has been used, *i.e.*

$$P_{Hi}(\mathbf{r}, \omega) = jk_\omega H_t(\mathbf{r}, \omega, \mathbf{r}_t) P_t(\omega) \quad (2.35)$$

and where $\nu(\mathbf{r}_s) = \beta(\mathbf{r}_s) - \gamma(\mathbf{r}_s)$ is the linear back scattering coefficient. The vector \mathbf{r}_t in the expression of the transmit beam H_t , specifies the point at which the beam is focused.

Finally, the expression of the signal that is received by the ultrasound system can be found by including the expression of the receive sensitivity $H(\mathbf{r}_s, \omega, \mathbf{r}_r)$, where \mathbf{r}_r specifies the focus of the receive sensitivity, and the relation between the pressure on the surface of the transducer and the pressure at a point in space is expressed by the spatial frequency response of the receiving transducer

$$P_r(\mathbf{r}_s, \omega) = jk_\omega H_r(\mathbf{r}_s, \omega, \mathbf{r}_r) dP_p(\mathbf{r}_s, \omega) d\mathbf{r}_s \quad (2.36)$$

where $dP_p(\mathbf{r}_s, \omega) = dP_p(\mathbf{r}_s, \omega, \mathbf{r}_s)$. Non-linear propagation is thus only considered in the forward propagating, incident pressure wave. This gives the first order received signal from a non-linearly scattering point in space as

$$dY_{p1}(\mathbf{r}_s, \omega) = k_\omega^4 P_t(\omega) H_t(\mathbf{r}_s, \omega, \mathbf{r}_t) H_r(\mathbf{r}_s, \omega, \mathbf{r}_r) V_p(\mathbf{r}_s, \omega, p_L) \\ \times [\nu(\mathbf{r}_s) + 2p_L(\mathbf{r}_s) \sigma_{nf}(\mathbf{r}_s)] d\mathbf{r}_s \quad (2.37)$$

The total signal from first order scattering within a volume can be obtained by integrating over the volume.

Note that the non-linear pulse form distortion filter has been simplified in this section to ease notation. As was discussed in Sec. 2.3 and 2.4, it is not only dependent on average LF pressure and scatterer position, as the present section suggests. The succeeding section will continue with the simplified notation.

2.5.2 Third Order Scattering

Developing a mathematical model for third order scattering between three arbitrarily placed point scatterers is a fairly straightforward expansion of the model

of first order scattering, presented in the previous section. Let the first, second and third scatterers have positions \mathbf{r}_1 , \mathbf{r}_2 , and \mathbf{r}_3 , respectively. From the Born approximation and the models in the previous section, the field at a point \mathbf{r} , resulting from a wave reflecting from the three scatterers can be described as

$$P_{p1}(\mathbf{r}, \mathbf{r}_1, \omega) = -k_\omega^2 G(\mathbf{r}, \mathbf{r}_1, \omega) P_i(\mathbf{r}_1, \omega) [\nu(\mathbf{r}_1) + 2p_L(\mathbf{r}_1) \sigma_{nf}(\mathbf{r}_1)] d\mathbf{r}_1 \quad (2.38)$$

$$P_{p2}(\mathbf{r}, \mathbf{r}_2, \omega) = -k_\omega^2 G(\mathbf{r}, \mathbf{r}_2, \omega) P_i(\mathbf{r}_2, \omega) [\nu(\mathbf{r}_2) + 2p_L(\mathbf{r}_2) \sigma_{nf}(\mathbf{r}_2)] d\mathbf{r}_2 \quad (2.39)$$

$$P_{p3}(\mathbf{r}, \mathbf{r}_3, \omega) = -k_\omega^2 G(\mathbf{r}, \mathbf{r}_3, \omega) P_i(\mathbf{r}_3, \omega) [\nu(\mathbf{r}_3) + 2p_L(\mathbf{r}_3) \sigma_{nf}(\mathbf{r}_3)] d\mathbf{r}_3 \quad (2.40)$$

if the incident wave, $P_i(\mathbf{r}, \omega)$ is a dual-band pulse. Now, letting the incident wave on the i 'th scatterer be the reflected field from the $(i-1)$ 'th scatterer, and letting the incident field on the first scatterer be the HF pulse from a transducer transmitting a pulse complex focused at \mathbf{r}_t , like in Eq. (2.35), the resulting wave from the third scatterer can be expressed as

$$\begin{aligned} P_{p3}(\mathbf{r}, \mathbf{r}_3, \mathbf{r}_2, \mathbf{r}_1, \omega) &= jk_\omega^7 G(\mathbf{r}, \mathbf{r}_3, \omega) G(\mathbf{r}_3, \mathbf{r}_2, \omega) G(\mathbf{r}_2, \mathbf{r}_1, \omega) \\ &\quad \times H_t(\mathbf{r}_1, \omega, \mathbf{r}_t) V_p(\mathbf{r}_1, \omega, p_L) P_t(\omega) \\ &\quad \times \nu(\mathbf{r}_1) \nu(\mathbf{r}_2) [\nu(\mathbf{r}_1) + 2p_L(\mathbf{r}_1) \sigma_{nf}(\mathbf{r}_1)] d\mathbf{r}_1 d\mathbf{r}_2 d\mathbf{r}_3 \end{aligned} \quad (2.41)$$

Note that the LF pressure dependent scattering component has been excluded from the second and third scattering terms, since the LF pressure is sufficiently reduced after the first scattering of the wave that they can be neglected.

Waves interacting with volume scatterers are scattered according to $-k_\omega^2 \nu(\mathbf{r})$, which are good models for the first and third order scattering points. However, in practice, the dominating second scatterer is the surface of the transducer, which scatters waves according to $\sigma_2(\mathbf{r}_2, \omega) = j2k_\omega R(\mathbf{r}_2, \omega) \delta(S_R(\mathbf{r}_2))$ [53], where R denotes a reflection coefficient and S_R denotes the area of the transducer. Therefore, let $\sigma(\mathbf{r}_2, \omega) = -k_\omega^2 \nu(\mathbf{r}_2)$ in Eq. (2.41). Furthermore, one can define the reverberation path between the scatterers as

$$dH_{rev}(\mathbf{r}_3, \mathbf{r}_2, \mathbf{r}_1, \omega) = G(\mathbf{r}_3, \mathbf{r}_2, \omega) G(\mathbf{r}_2, \mathbf{r}_1, \omega) \quad (2.42)$$

and by including the sensitivity of the receiving transducer, as in Eq. (2.36) and Eq. (2.37), the expression for the received signal due to reverberation between three scatterers at \mathbf{r}_1 , \mathbf{r}_2 , and \mathbf{r}_3 is

$$\begin{aligned} dY_{p3}(\mathbf{r}_3, \mathbf{r}_2, \mathbf{r}_1, \omega) &= k_\omega^6 P_t(\omega) H_t(\mathbf{r}_1, \omega, \mathbf{r}_t) V_p(\mathbf{r}_1, \omega, p_L) \\ &\quad \times dH_{rev}(\mathbf{r}_3, \mathbf{r}_2, \mathbf{r}_1, \omega) H_r(\mathbf{r}_3, \omega, \mathbf{r}_r) \\ &\quad \times \nu(\mathbf{r}_3) \sigma_2(\mathbf{r}_2, \omega) [\nu(\mathbf{r}_1) + 2p_L(\mathbf{r}_1) \sigma_{nf}(\mathbf{r}_1)] d\mathbf{r}_1 d\mathbf{r}_2 d\mathbf{r}_3 \end{aligned} \quad (2.43)$$

Briefly explained, Eq. (2.43) states that the transmitted HF pressure wave is scattered at the first point with a strength defined by

- the scattering coefficients at that point ($\nu(\mathbf{r}_1)$, $\sigma_{nf}(\mathbf{r}_1)$)

- the instantaneous amplitude of the co-propagating LF pulse ($p_L(\mathbf{r}_1)$)
- the transmit beam magnitude at that point ($H_t(\mathbf{r}_1, \omega, \mathbf{r}_t)$)

and the resulting pulse form is the second order differentiation ($-k_\omega^2$) of the original pulse form. Furthermore, the non-linear distortion ($V_p(\mathbf{r}_1, \omega, p_L)$) of the pulse is accumulated to this point and is dependent on the beam form, LF pressure, frequency separation, focusing configuration and phase relation of the HF and LF pulses.

The reflected wave then propagates linearly, according to a free-space Greens function, to the second scatterer. At this interface, the wave form is scattered linearly ($\sigma_2(\mathbf{r}_2, \omega)$) and yet again differentiated twice ($-k_\omega^2$), before beginning its propagation towards the third scatterer. This propagation is also linear and according to a free-space Greens function. These two propagation paths are described by $dH_{rev}(\mathbf{r}_3, \mathbf{r}_2, \mathbf{r}_1, \omega)$.

As the wave is scattered for a third time, the pulse form is differentiated twice ($-k_\omega^2$), and the magnitude of the scattering is determined by the linear scattering coefficients in the third point ($\nu(\mathbf{r}_3)$). The wave travels linearly to the transducer according to a free-space Greens function, but the amount of signal that is received is dependent on the sensitivity of the transducer to wave coming from the position of the third scatterer. The propagation and sensitivity are contained in the expression of the receive beam, $H_r(\mathbf{r}_3, \omega, \mathbf{r}_r)$.

Processing

Conventional ultrasound B-mode imaging has relatively simple processing before image reconstruction, after time-gain compensation (TGC) and beam-forming in the analogue front-end of the scanner. The received data, or post-beam-formed RF data, is demodulated, logarithmically compressed, and the result is displayed on the screen of the scanner. Additional image processing may be and is often applied to the frames as well.

With SURF imaging, more processing is applied to the post-beam-formed RF data in order to suppress various signal components. This chapter will focus on the suppression of acoustic noise, or pulse reverberation.

In Fig. 3.1, a block diagram of the signal processing is shown. It is a simple aid to illustrate how the signals in this text relate to one another, and so the spatial co-ordinate \mathbf{r} has been omitted. The input of the system is the transmitted pressure wave, which is decomposed into the sum of a HF wave, $p_H(t)$, and a LF wave $p_L(t)$. These are filtered by the spatial impulse response of the transmitting and receiving transducer apertures, $h_t(t)$, and $h_r(t)$, which are the time-domain descriptions of the filters $H_t(\mathbf{r}, \omega)$ and $H_r(\mathbf{r}, \omega)$ in Sec. 2.5. The last of the acoustic filters is the non-linearity filter $v_p(t)$, which again is the time domain description of the filter $V_p(\mathbf{r}, \omega)$ from Sec. 2.5. Thus, including the spatial co-ordinate in the expressions, the relations are

$$H_t(\mathbf{r}, \omega) = \mathcal{F}_t [h_t(\mathbf{r}, t)] \quad (3.1)$$

$$H_r(\mathbf{r}, \omega) = \mathcal{F}_t [h_r(\mathbf{r}, t)] \quad (3.2)$$

$$Y_p(\mathbf{r}, \omega) = \mathcal{F}_t [v_p(\mathbf{r}, t)] \quad (3.3)$$

where $\mathcal{F}_t[\cdot]$ denotes a Fourier transform in time.

The signals are subsequently filtered by the acousto-electric transfer function of the receiving transducer, $h_{rt}(t)$ and the receive electronics, represented by a

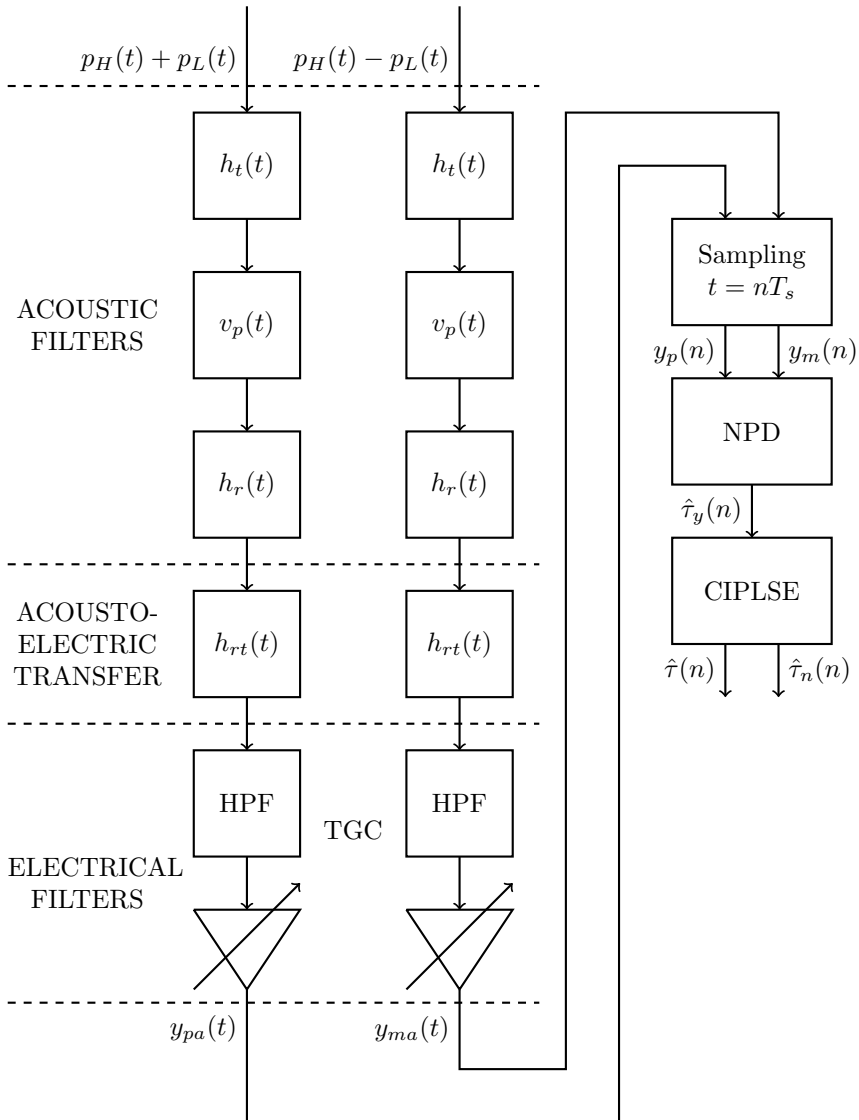


Figure 3.1: The block diagram shows the connection between the different signals described in the text. The spatial co-ordinate has been omitted.

band pass filter (BPF). Beam-forming and TGC is applied to the signals, and the resulting RF signals $y_p(t)$ and $y_m(t)$ are obtained and sampled. It is from these sampled RF signals, $y_p(n)$ and $y_m(n)$, that one can estimate the non-linear propagation delay (NPD), $\hat{\tau}_y(n)$ via the method in Sec. 3.2. From the NPD one can obtain estimates of first and third order delays, $\hat{\tau}(n)$ and $\hat{\tau}_n(n)$, via the constrained incremental polynomial least squares estimator (CIPLSE), described in Sec. 3.3. All of these delay estimates are used in suppression of reverberations, as will be described in Sec. 3.5.

3.1 Pulse Reverberation

The total pulse reverberation which is received at the same time as a first order signal is the sum of all combinations of reverberation that have propagation paths limited by

$$|\mathbf{r}_1| + |\mathbf{r}_2 - \mathbf{r}_1| + |\mathbf{r}_3 - \mathbf{r}_2| + |\mathbf{r}_3| = 2z \quad (3.4)$$

where \mathbf{r}_i denotes the position in space of scatterer i , and z is the depth from which a first order reflection is simultaneously received. In practice, the dominant second scatterer at \mathbf{r}_2 is the transducer. Assuming that the transducer is the *only* source of second order scattering, and that the transducer surface defines the depth $z = 0$, simplifies the following noise model and allows for the classification of reverberation types. Mathematically, the signal path requirement becomes that

$$|\mathbf{r}_1| + |\mathbf{r}_3| = z \quad (3.5)$$

To further simplify the model it is assumed that the transversal variation in material parameters can be neglected, limiting the analysis to scattering planes perpendicular to the propagation direction. Thereby, the scattering parameters are functions of depth only, and the signal path requirement becomes

$$z_1 + z_3 = z \quad (3.6)$$

which is visualised in Fig. 2.3. Reverberations that interfere with the first order signal from z have only been under the influence of the LF pulse for a distance of z_1 . This is opposed to the first order signal that is affected for the full length z . Since z_1 could be anywhere between the transducer and the scatterer at z , the reverberation that interferes at z is the sum of signals having different non-linear propagation delay, since this effect is cumulative with depth.

Estimating the signal strength of each signal component and its corresponding delay in a Fourier manner is not practically feasible, so the SURF signal model assumes that the *average* delay of the noise components is given by the delay of the first order signal at $z_1 = z/2$. The signal model can be written as the sum of a first order reflection, modified by a *first order delay*, τ , and a noise term,

modified by a *noise delay*, also called a *third order delay*, τ_n . In the frequency domain, this can be written as

$$Y_p(z, \omega) = \tilde{V}_p(z, \omega)X_l(z, \omega)e^{-j\omega\tau(z)} + \tilde{N}_p(z, \omega)e^{-j\omega\tau_n(z)} \quad (3.7)$$

$$Y_m(z, \omega) = \tilde{V}_m(z, \omega)X_l(z, \omega)e^{j\omega\tau(z)} + \tilde{N}_m(z, \omega)e^{j\omega\tau_n(z)} \quad (3.8)$$

with a positive and a negative LF transmit pressure, respectively. In these equations, Y_p and Y_m are the frequency descriptions of the received time-signals, $y_p(t)$ and $y_m(t)$, *i.e.*

$$Y_p(z, \omega) = \mathcal{F}_t[y_{pa}(z, t)] \quad (3.9)$$

$$Y_m(z, \omega) = \mathcal{F}_t[y_{ma}(z, t)] \quad (3.10)$$

where $\mathcal{F}_t[\cdot]$ denotes a Fourier transform in time.

Further, $N_p(z, \omega) = \tilde{N}_p(z, \omega)e^{-j\omega\tau_n(z)}$ and $N_m(z, \omega) = \tilde{N}_m(z, \omega)e^{j\omega\tau_n(z)}$ represent the noise signal using a positive and a negative LF transmit pressure, respectively. $V_p(z, \omega) = \tilde{V}_p(z, \omega)e^{-j\omega\tau(z)}$ and $V_m(z, \omega) = \tilde{V}_m(z, \omega)e^{j\omega\tau(z)}$ are filters describing the non-linear distortion and delays of the HF pulses, which occur as a result of the presence of the LF pulses. Again, the subscripts p and m denote the use of a positive and negative LF transmit pressure, respectively. $X_l(z, \omega)$ represents the part of the signal that is produced by first order linear scattering, and ultimately what should be displayed.

The signal models for first order scattering can be found as the volume integral of Eq. (2.37), and similarly one can construct a mathematical model for the third order scattering by integrating Eq. (2.43) over a volume of scatterers. These definitions and integrals of the signal components are defined in Angelsen and Tangen [53]. Because the derivations require some space and are not directly relevant to the following sections, they will be omitted here. The signal models in Eq. (3.7) and Eq. (3.8) are based on the signal models in Sec. 2.5 and the simplifications mentioned so far in this chapter. The noise terms can be defined as

$$N_p(z, \omega) = \tilde{N}_p(z, \omega)e^{-j\omega\tau_n(z)} \quad (3.11)$$

$$N_p(z, \omega) = \int_{z_1=0}^z \int_{z_3=z_{3a}}^{z_{3b}} \int_{\mathbf{r}_{1\perp} \in S} \int_{\mathbf{r}_{2\perp} \in S_t} \int_{\mathbf{r}_{3\perp} \in S} dY_{p3}(z_3, z_2=0, z_1, \mathbf{r}_{3\perp}, \mathbf{r}_{2\perp}, \mathbf{r}_{1\perp}) \\ \times d\mathbf{r}_{3\perp} d\mathbf{r}_{2\perp} d\mathbf{r}_{1\perp} dz_3 dz_2 dz_1 \quad (3.12)$$

where

$$z_{3a} = z - z_1 - \frac{z_p H(z)}{2} \quad (3.13)$$

$$z_{3b} = z - z_1 + \frac{z_p H(z)}{2} \quad (3.14)$$

and $z_p H(z)$ is the spatial extent of the HF pulse when the centre of gravity of the pulse is in z . Since the pulse length is dependent on the frequency content

of the pulse, this length will vary with depth due to the non-linear PFD. In Eq. (3.12) S is a surface which is perpendicular to the propagation direction of the wave, and S_t is the surface of the transducer. The integrand is the expression that was derived in Eq. (2.43). A similar expression can be constructed for $N_m(z, \omega) = \tilde{N}_m(z, \omega)e^{j\omega\tau_n(z)}$.

The expression for the first order reflection is less complicated, and may simply be written as

$$X_l(z, \omega) = \int_S dY_{p1}(z, \mathbf{r}_\perp, \omega) d\mathbf{r}_\perp \quad (3.15)$$

where the integrand is the expression for first order scattering from Eq. (2.37).

The objective of SURF processing to remove reverberation noise is ultimately to be able to find good estimates of X_l , $N_p(z, \omega) = \tilde{N}_p(z, \omega)e^{-j\omega\tau_n(z)}$, $N_m(z, \omega) = \tilde{N}_m(z, \omega)e^{j\omega\tau_n(z)}$, and $V_p(z, \omega) = \tilde{V}_p(z, \omega)e^{-j\omega\tau(z)}$ and $V_m(z, \omega) = \tilde{V}_m(z, \omega)e^{j\omega\tau(z)}$. Currently, there are only methods for estimating NPD, and the first and third order delays τ and τ_n , so the noise suppression schemes, presented in Sec. 3.5, are based on the assumption that $V_p(z, \omega) = V_m(z, \omega) = 1$, and that $\tilde{N}_p(z, \omega) = \tilde{N}_m(z, \omega)$.

3.2 Estimation of Non-Linear Propagation Delay (NPD)

The non-linear propagation delay that is accumulated along imaging lines is of primary importance to SURF imaging, and indeed to one of the methods presented in the following section. This section will briefly outline the algorithm that is used to estimate NPD between two received signals [59].

Let the signals $y_{pa}(t)$ and $y_{ma}(t)$ be analogue, received RF signals after beamforming with positive and negative transmit pressures, respectively. These signals are the summation of the signals $y_{pa}(z, t)$ and $y_{ma}(z, t)$ from Eq. (3.9) and Eq. (3.10) for all depths, z . Thus, they may be defined as

$$y_{pa}(t) = \int_0^{z_{max}} y_{pa}(z, t) dz \quad (3.16)$$

$$y_{ma}(t) = \int_0^{z_{max}} y_{ma}(z, t) dz \quad (3.17)$$

The analogue signals are sampled so that $y_p(n) = y_{pa}(nT_s)$ and $y_m(n) = y_{ma}(nT_s)$, where T_s is the sampling period. The sampled RF signals can then be defined as

$$y_p(n) = s \left(n + \frac{1}{2} \tau_y(n) \right) \quad (3.18)$$

$$y_m(n) = s \left(n - \frac{1}{2} \tau_y(n) \right) \quad (3.19)$$

where

$$s(n) = a(n)\exp[i(\phi(n) + \omega_c n)] \quad (3.20)$$

and where a is an amplitude, ω_c is the angular centre frequency of the signal, ϕ is a modulating phase, τ_y is the non-linear propagation delay (NPD), and n is the sample number. y_p is the received signal when using a positive LF pressure, and y_m is the received signal when using a negative LF pressure. Assuming that the phase difference between the signals is linearly related to the delay via the instantaneous frequency, one can find the phase difference by cross-multiplying the signals and taking the argument, resulting in

$$\begin{aligned} \psi(n) &= \arg\{y_p(n)y_m(n)\} \\ \psi(n) &= \phi\left(n + \frac{1}{2}\tau_y(n)\right) - \phi\left(n - \frac{1}{2}\tau_y(n)\right) + \omega_c\tau_y(n) \\ \psi(n) &\approx [\dot{\phi}(n) + \omega_c]\tau_y(n) \end{aligned} \quad (3.21)$$

If one then uses the approximation relating the instantaneous frequency to the phase difference, θ , so that $\theta(n) \approx \dot{\phi}(n) + \omega_c$ one can write that

$$\psi(n) \approx \theta(n)\phi(n) \quad (3.22)$$

The algorithm was developed by Standal et al. [59], and uses a sliding window with a fixed length $2L + 1$, centred on a sample n to estimate the NPD at the sample n , $\tau_y(n)$. The method is based on a linear model with a weighted Euclidean norm, minimizing

$$J(\boldsymbol{\alpha}) = \boldsymbol{\psi}^T \mathbf{D} \boldsymbol{\psi} - 2\boldsymbol{\alpha}^T \boldsymbol{\Theta}^T \mathbf{D} (\boldsymbol{\psi} - \boldsymbol{\Theta} \boldsymbol{\alpha}) \quad (3.23)$$

for each sample n , where $\boldsymbol{\alpha} = [\hat{\tau}_y(n), \partial\hat{\tau}_y(n)/\partial n]^T$. The \mathbf{D} matrix is a diagonal weighting and windowing matrix. The vectors $\boldsymbol{\psi}$, and $\boldsymbol{\theta}$ are column vectors consisting of $2L + 1$ sample values, centred around sample n , so that

$$\boldsymbol{\psi} = [\psi(n-L), \dots, \psi(n), \dots, \psi(n+L)]^T \quad (3.24)$$

$$\boldsymbol{\theta} = [\theta(n-L), \dots, \theta(n), \dots, \theta(n+L)]^T \quad (3.25)$$

and $\boldsymbol{\Theta} = [\boldsymbol{\ell} \circ \boldsymbol{\theta}, \boldsymbol{\theta}]$, where $\boldsymbol{\ell} = [-L, \dots, L]^T$ and \circ denotes the Hadamard product of two matrices. From this minimization, the non-linear delay is estimated as

$$\hat{\tau}_y(n) = \frac{S_0(n)T_1(n) - S_1(n)T_0(n)}{S_0(n)S_2(n) - S_1^2(n)} \quad (3.26)$$

where

$$S_k(n) = \sum_{\ell=-L}^L c(n+\ell)\theta(n+\ell)^2 w(\ell)\ell^k \quad (3.27)$$

$$T_k(n) = \sum_{\ell=-L}^L c(n+\ell)\theta(n+\ell)\phi(n+\ell)w(\ell)\ell^k \quad (3.28)$$

and \mathbf{c} and \mathbf{w} are the weighting and windowing vectors constituting $\mathbf{D} = \text{diag}(\mathbf{c} \circ \mathbf{w})$.

3.3 Estimation of First and Third Order Delays

The first and third order delays in Eq. (3.7) and Eq. (3.8) are crucial to the suppression scheme that is presented in Sec. 3.5. With a good transmit set-up, one can observe from simulations that the non-linear propagation delay accumulates in the forward propagating wave in a fairly linear manner. Thus, the expected first order delay should be close to linear, and dependent on the non-linearity parameter of the material, and the LF pressure. The expected development of NPD can be seen in Fig. 3.2, which shows the simulated propagation delay between an HF pulse co-propagating with a positive LF pulse, and an HF pulse propagating without the manipulation of an LF wave.

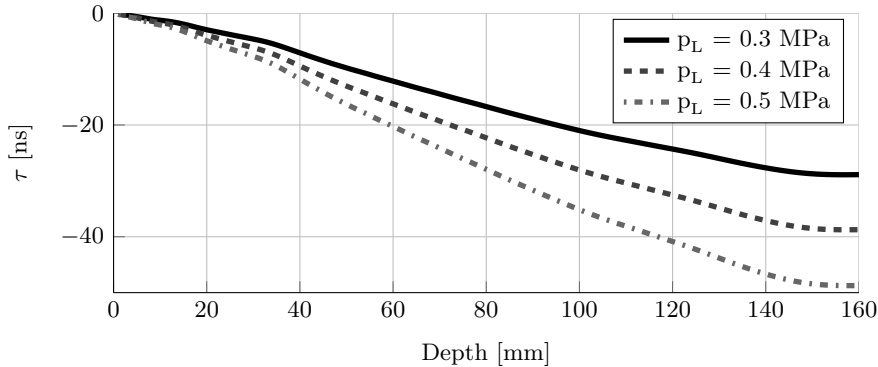


Figure 3.2: Simulation of non-linear propagation delay as a function of depth, with different positive LF pressure amplitudes. The simulation was done using *WaveSim*, using the dimensions of the *Skolmen* probe, and the simulation medium is muscle tissue.

Currently, the group working on SURF imaging at ISB, NTNU uses a constrained incremental polynomial least squares estimator (CIPLSE) to estimate the first order delay, $\hat{\tau}$, from the estimated NPD, $\hat{\tau}_y$. In effect, this estimator is a multi-stage polynomial fitter with an initial peak detector. A block diagram of the estimator is shown in Fig. 3.3.

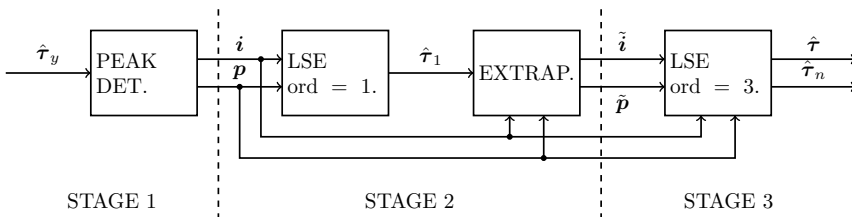


Figure 3.3: The CIPLSE block diagram.

The figure shows the input vector that is the estimated NPD, $\hat{\tau}_y$, the linear regression of the NPD, $\hat{\tau}_1$, and the estimated first and third order delays, $\hat{\tau}$ and $\hat{\tau}_n$. The vectors \mathbf{i} and \mathbf{p} are the indices and values of the extrema in the NPD, respectively. Additional points that are used to stabilize the final estimates of $\hat{\tau}$ and $\hat{\tau}_n$ at larger depths are found from the linear extrapolation of these extrema, and are represented in the figure by the vectors $\tilde{\mathbf{i}}$ and $\tilde{\mathbf{p}}$.

The first stage of the estimator is a peak-detector that selects the points that are to be used in the estimation. The points that are selected are positive or negative peaks on the NPD curve, depending on the LF polarity, and must be monotonously increasing or decreasing. Additionally, the first point in the estimation is set to 0, because at the transducer, the NPD should be 0, irrespective of the value given by the estimator in Sec. 3.2, since no non-linear propagation has occurred. The peak detector uses a sliding hamming window to low-pass filter the NPD estimate in order to remove noise peaks from the estimate. It then calculates the difference in subsequent samples to determine whether or not each sample is a maxima or a minima. Finally, if subsequent maxima or minima are not increasing or decreasing monotonously, they are discarded, leaving the estimator with the monotonously increasing or decreasing local extrema on the NPD estimate.

The second stage of the estimator uses least squares linear regression to fit a linear function to the selected points from the peak-detector. After fitting the linear function, the estimator uses the linear estimate to extrapolate two new data points from the originally selected peak points. This is done because the NPD becomes more noisy at larger depths, due to reduced signal-to-noise ratio (SNR), as discussed in Ch. 4. The extrapolated data points prevent the next step in the estimator from becoming unstable.

The final stage in the estimation of first order delay is to fit a third degree polynomial to the data points from the peak detector and the linear extrapolation. The resulting estimate should be a monotonously decreasing or increasing curve with a slope that flattens with increased depth. This is to be expected because the LF pressure will inevitably drop as the depth increases and diffraction takes its toll on the amplitude of the wave.

The estimator gives an estimate of first order delay, $\hat{\tau}(n)$, and third order delay $\hat{\tau}_n(n) = \hat{\tau}(n)$, given an estimate of the NPD, $\hat{\tau}_y(n)$ between two signals $y_p(n)$ and $y_m(n)$.

3.4 Beam Interpolation Scheme

In SURF imaging, at least two pulse complexes with different LF pressure must be transmitted in each imaging direction, *i.e.* along each image line. This decreases the frame rate of the imaging system, but allows for suppression of unwanted signal components.

To speed up the data acquisition, one can design algorithms that use sparsely acquired data and interpolation to create artificial image data that closely resembles densely acquired actual data. This can be done for instance either by creating additional, completely artificial RF data by interpolating over acquired image lines, or by using a subset of image lines with a certain LF polarity in combination with a complete set of image lines with another LF polarity, and exploiting the non-linear propagation effects to fill in missing image lines in the first subset of lines.

The first of these methods will be called beam RF interpolation (BRI), and has the potential to double the rate of acquisition. The method is not specific to SURF imaging, since it does not rely on non-linear propagation effects. The second method will be called beam delay interpolation (BDI). It is a method that is specific to SURF imaging since it relies on the non-linear propagation delay that is incurred by this method, and has the potential to increase frame rate by 50%.

Both of the presented methods are new. BRI was proposed by Angelsen [60], and BDI is a new method first proposed in this thesis.

3.4.1 Beam RF Interpolation (BRI)

The BRI method of creating artificial image line data uses sparsely acquired RF data. The performance of the method relies on slow variation of material parameters transversally to the scanning direction. If the scatterers contributing to two image lines are dissimilar, the artificial interpolated image line, representing data which is dependent on the scatterers lying in between the original lines, will have no provable connection to the physical situation. The artificial data could model the physical situation well, or it could be completely arbitrary. Slow transversal variations in the material increases the validity of the interpolated prediction, since the prediction is more likely to be similar to the original data, rather than being completely different.

To avoid spatial sampling artefacts, the requirement in phased array scanning is that the angular distance between neighbouring beams should be limited by

$$\Delta\phi_s < \frac{\lambda_{min}}{a} \quad (3.29)$$

where $\Delta\phi_s$ is the angular increment between two beams, or the angular sampling interval, λ_{min} is the smallest significant wave length in the transmitted pulse, and a is the width of the transmit aperture. This can be best understood by viewing the imaging system in k-space, and the topic is covered in depth by Angelsen [61].

Another problem with BRI is that it requires a very homogeneous transducer, in order to correctly represent the transmitting aperture for the artificial lines.

The fact that the interpolation scheme would vary in performance depending on which transducer were used makes the method somewhat less robust than one would desire.

Finally, the data acquisition method itself sets an important limitation on the performance of the algorithm. Phased array scanning and linear scanning with a curvilinear array both increment the direction of the transmitted sound beam with each scan line. By skewing the beam in this way, the interpolation is destroyed even though the beams overlap substantially. This is because the angle between the adjacent transmit beams cause the received signal at a certain depth to consist of the echo contributions from two completely different sets of scatterers.

Mathematically, one can define a set \mathbf{B} of acquired RF data as consisting of J vectors of lengths N , and a set \mathbf{L} of expanded data to be used in processing and image reconstruction as consisting of I vectors of lengths N , where $I = 2J$, so that $\mathbf{B} \subset \mathbf{L}$.

$$\mathbf{B} = \{\mathbf{b}_i \mid i \in \{1, 2, \dots, J\}\} \quad (3.30)$$

$$\mathbf{L} = \{\boldsymbol{\ell}_i \mid i \in \{1, 2, \dots, I\}\} \quad (3.31)$$

where the vectors in \mathbf{B} are received RF data with one of two polarities. For instance, one could think of \mathbf{B} as a set of vectors containing RF data acquired from each imaging direction with a positive LF pressure, so that $\mathbf{b}_i = \mathbf{y}_{pi}$, where \mathbf{y}_{pi} is the vector defined in Eq. (3.18).

The sets have cardinalities related by $|\mathbf{L}| = IN = 2JN = 2|\mathbf{B}|$. The linear interpolation of the RF data which produces the image data can then be written as a linear transformation

$$\mathbf{T}_L : \mathbf{B}^2 \mapsto \mathbf{L} \quad (3.32)$$

Using a cubic spline interpolation, the linear transformation becomes

$$\mathbf{T}_S : \mathbf{B}^J \mapsto \mathbf{L}^I \quad (3.33)$$

In other words, the spline interpolation requires that all vectors in \mathbf{B} are known before the interpolation can be done.

The transformations are defined as

$$\mathbf{T}_L : \mathbf{l}_i = \begin{cases} 2\mathbf{b}_{i/2} - \mathbf{b}_{i/2-1}, & i = I \\ \frac{1}{2}(\mathbf{b}_{i/2} + \mathbf{b}_{i/2+1}), & i \in \{2n : n \in [1, I-2]\} \\ \mathbf{b}_{(i+1)/2}, & i \in \{2n-1 : n \in [1, I]\} \end{cases} \quad (3.34)$$

where $\mathbf{l}_i \in \mathbf{L}$ with $\mathbf{l}_i \in \mathcal{R}^N$, and $\mathbf{b}_i \in \mathbf{B}$ with $\mathbf{b}_i \in \mathcal{R}^N$. Further,

$$\mathbf{T}_S : \mathbf{l}_i = \begin{cases} \mathbf{f}_s(i), & i \in \{2n : n \in [1, I]\} \\ \mathbf{b}_{(i+1)/2}, & i \in \{2n-1 : n \in [1, I]\} \end{cases} \quad (3.35)$$

where

$$\mathbf{f}_s(i) = \mathbf{S}_3(2j, \mathbf{b}_j) \quad (3.36)$$

is the N element vector containing the cubic splines over the vectors \mathbf{b}_j , $j = 1, \dots, J$ as $n = 1, \dots, N$. In other words, a cubic spline is defined by the samples $b_j[n]$, $j = 1, \dots, J$, for all n , giving n cubic splines for each data set \mathbf{B} .

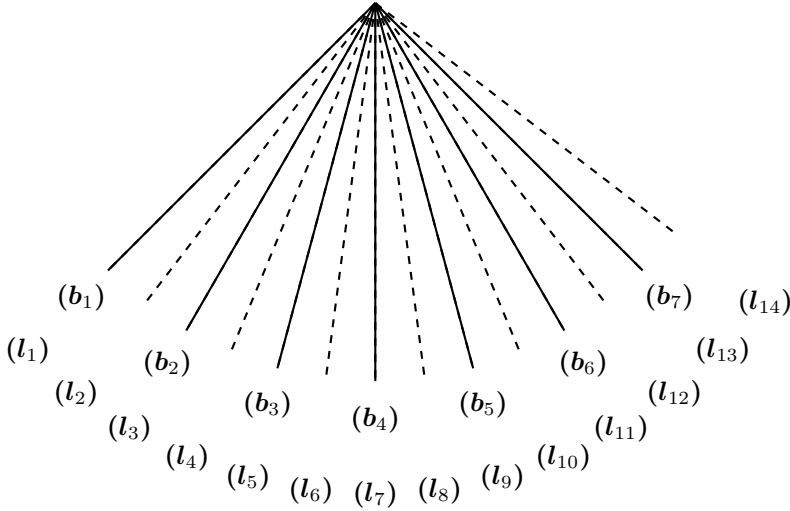


Figure 3.4: A graphic representation of BRI with the beam data vectors \mathbf{b}_i and the interpolated data \mathbf{l}_i , when the beams are arranged as in a phased array.

3.4.2 Beam Delay Interpolation (BDI)

BDI has the potential to yield better estimates of image line data than BRI, since all the RF lines are based upon reflections from a correct set of scatterers. For each frame, data is collected from each imaging direction with one of two LF polarities. This produces a set of data \mathbf{M} consisting of I vectors, \mathbf{m}_i which in turn consist of N samples each. In other words, $|\mathbf{M}| = IN$. Additionally, data is collected along every other imaging direction with the opposite LF polarity, producing a set of data \mathbf{P} consisting of $J = I/2$ vectors, \mathbf{p}_j which in turn consist of N samples each. In other words, $|\mathbf{P}| = JN = |\mathbf{M}|/2$. This means that \mathbf{m}_{2j-1} and \mathbf{p}_j are data vectors which are acquired from steering the transmitted sound beam in the same direction, and that the vectors \mathbf{m}_{2j} are missing their counterparts in \mathbf{P} . BDI estimates these counterparts via interpolation of the non-linear propagation delay that can be calculated between the vectors \mathbf{m}_{2j-1} and \mathbf{p}_j . A graphical representation of the method is shown in Fig. 3.5.

The estimation of the non-linear propagation delay, defined in Eq. (2.25), in

direction j can be written as

$$\hat{\tau}_{yj} = \text{NPD}(\mathbf{m}_{2j-1}, \mathbf{p}_j) \quad (3.37)$$

where the operation $\text{NPD}(\cdot, \cdot)$ is the CIPLSE described in Sec. 3.3.

By defining $\mathbf{S}_1 = \{\hat{\tau}_{yj} : j \in [1, J]\}$ and $\mathbf{S}_2 = \{\check{\tau}_{yi} : i \in [1, I]\}$ the interpolation of the NPD can be written as a linear transformation

$$\mathbf{T}_\tau : \mathbf{S}_1^2 \mapsto \mathbf{S}_2 \quad (3.38)$$

where

$$\mathbf{T}_\tau : \check{\tau}_{yi} = \begin{cases} 2\hat{\tau}_{y,i/2} - \hat{\tau}_{y,i/2-1}, & i = I \\ \frac{1}{2}(\hat{\tau}_{y,i/2} + \hat{\tau}_{y,i/2+1}), & i \in \{2n : n \in [1, I]\} \\ \hat{\tau}_{y,(i+1)/2}, & i \in \{2n-1 : n \in [1, I]\} \end{cases} \quad (3.39)$$

Applying the interpolated delays to the corresponding vectors \mathbf{m}_{2j-1} with missing counterparts in \mathbf{P} , will complete the set of positive pulses, so that

$$\check{\mathbf{p}}_j = \mathbf{m}_{2j}(\check{\tau}_{y2j}), \quad j \in [1, J] \quad (3.40)$$

Finally, by defining $\check{\mathbf{P}} = \{\check{\mathbf{p}}_j : j \in [1, J]\}$, the set of all p-polarity data, \mathbf{P}' , acquired directly or via BDI, can be defined as $\mathbf{P}' = \mathbf{P} \cup \check{\mathbf{P}}$.

As is evident from the mathematics, BDI is a slightly more complex task compared to BRI. The method is reliant on a good estimation of NPD, meaning that $|\tau_y - \hat{\tau}_y|$ is small, and assumes that PFD and PFM are negligible. The strength of the method lies in that the data in \mathbf{M} , on which the artificial data is based, is entirely defined by the combinations of scatterers that contribute to the backscattered signal in each direction. Thus, the artificial lines are based on real scattering conditions in the imaged medium. The method also avoids issues regarding non-uniformity of the transmit aperture, and differences in beam profiles due to steering angle, aberrations, etc.

BDI is also dependent on the slow variation of NPD transversally to the beam directions. The NPD is accumulative with depth and is less dependent on the rapid variation in material parameters than the RF signals. Unless the backscattered signal at a given depth is very strong, the rapid variations will be averaged, and result in a smoothed NPD, as one can see by its definition in Eq. (2.25). An interpolation between two adjacent developments should therefore yield a usable estimate of the development that would occur in a beam between the two. An exception could yet again be in areas where adjacent beams cover widely different tissue areas like the echogenic myocardium and the hypochoic left ventricular cavity.

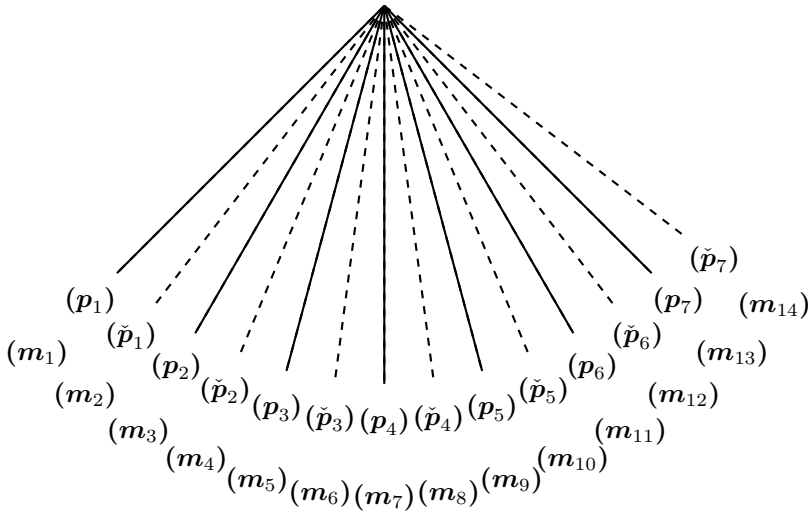


Figure 3.5: A graphic representation of BDI with the beam data vectors \mathbf{m}_i and \mathbf{p}_i , and the interpolated data $\check{\mathbf{p}}_i$, when the beams are arranged as in a phased array.

3.5 Reverberation Suppression

From Jahren [51], it is known that under controlled conditions, the SURF technique can suppress reverberations well. By checking the reverberation suppression capabilities of the SURF method with and without BRI or BDI, one can assess whether or not the interpolation methods degrade one of the fundamental advantages of the SURF technique; suppressing reverberations.

The suppression scheme that is used in Ch. 4 is taken from Angelsen and Tangen [53], and is a weighted difference between the received signals resulting from transmissions with positive and negative LF polarities. For each image line, one can estimate the first order scattered signal as

$$\hat{x}_l(n) = \frac{y_p(n + f_s \hat{\tau}_n(n)) - y_m(n - f_s \hat{\tau}_n(n))}{\mu + 2 \sin[\omega_c(\hat{\tau}(n) - \hat{\tau}_n(n))]} \quad (3.41)$$

where, \hat{x}_l is the estimated signal from first order scattering, y_p is the received signal from a positive LF polarity transmission, Eq. (3.18), y_m is the received signal from a negative LF polarity transmission, Eq. (3.19), $\hat{\tau}$ is the estimated first order delay, $\hat{\tau}_n$ is the estimated third order delay, ω_c is the angular centre frequency of the HF pulse, f_s is the sampling frequency, and μ is a noise parameter which prevents the amplitude of \hat{x}_l from becoming very large when $\hat{\tau}$ and $\hat{\tau}_n$ are similar.

Using interpolated artificial image lines, \check{y}_p , in stead of y_p in every other imaging line, does not change the formula for estimating the first order scattered

signal. For image lines with artificial positive polarity LF pulses, the expression becomes

$$\tilde{x}_l(n) = \frac{\tilde{y}_p(n + f_s \hat{\tau}_n(n)) - \tilde{y}_m(n - f_s \hat{\tau}_n(n))}{\mu + 2 \sin [\omega_c (\hat{\tau}(n) - \hat{\tau}_n(n))]} \quad (3.42)$$

$$\tilde{x}_l(n) = y_m \left(n + f_s \frac{\hat{\tau}_y(n)}{2} \right) \frac{\sin \left[\omega_c \left(\frac{\hat{\tau}_y(n)}{2} - \hat{\tau}_n(n) \right) \right]}{\sin [\omega_c (\hat{\tau}(n) - \hat{\tau}_n(n))]} \quad (3.43)$$

using BRI and BDI, respectively. Recall that $\hat{\tau}_y$ is the estimated NPD between the signals resulting from transmissions with positive and negative LF polarities. Comparison of the resulting images using Eq. (3.41), Eq. (3.42), and Eq. (3.43) to suppress noise will be one of the quality measures for BRI and BDI in this thesis.

Phantom Recordings

The following chapter presents the main results of this thesis. Measurements of a tissue mimicking phantom from CIRS [62] were taken using the modified SonixMDP scanner and the *Skolmen* probe. The probe was fixed in place using a vice, and water was filled in the water well of the phantom to ensure good coupling between the transducer and the phantom.

The set-up of the scanner software is given in App. D.

Data was acquired by the scanner, and stored as un-processed RF data. This raw data was modeled by the signals y_p and y_m in Eq. (3.18) and Eq. (3.19). In other words, the available data was beam-formed, amplified with a time-gain compensation amplifier (TGC), and band-pass filtered by the receive electronics of the scanner. Further processing was done off-line, using MATLAB.

To compare originally acquired data with interpolated data, the scanner recorded and stored all image lines in each image. In other words data was acquired when transmitting with either positive or negative LF pressure in each direction, so that y_p and y_m were known in each direction. Interpolation could be done later by simply removing a subset of image lines from the original data, and using the remaining data to interpolate a replacement for each removed image line.

The main points of interest in the measurements were how the artificially constructed data, described in Ch. 3, compared to real acquired data. The effects of beam width and line density changes on the quality of the artificial data were also of primary concern.

Secondly, the two interpolation techniques described in Ch. 3 were to be compared by examining differences in signal envelopes and reverberation suppression. Images interpolated with BRI and BDI are shown in Sec. 4.2 and Sec. 4.3, respectively.

Each figure consists of three images. The signal envelope of the original data is visualised in the top image, the signal envelope of the interpolated data is visualised in the middle, and the relative difference between the two is shown in at the bottom of each set of images.

The images showing the signal envelopes are B-mode images, shown with a dynamic range of 65 dB, normalized to the maximum value in the entire image. The difference images show relative difference between the signal envelope of the original data, and of the interpolated data. Given in the terms of Ch. 3, the relative differences \mathbf{d}_i can be written

$$\mathbf{d}_i = \left| \frac{\log_{10} (|\ell_{e,i}|) - \log_{10} (|\mathbf{b}_{e,i}|)}{\log_{10} (|\mathbf{b}_{e,i}|)} \right| \quad (4.1)$$

when using BRI, where the subscript e denotes the complex envelope of the signal. This is typically obtained via the hilbert transform, or via demodulation of the signal. Using BDI, the expression is similar;

$$\mathbf{d}_i = \left| \frac{\log_{10} (|\check{\mathbf{p}}_{e,i}|) - \log_{10} (|\mathbf{p}_{e,i}|)}{\log_{10} (|\mathbf{p}_{e,i}|)} \right| \quad (4.2)$$

The scale in the difference images are in the range $[0, 1]$ with black representing a value of 0, and white representing a value of 1.

The relative difference in signal envelope can be quantified, and the average envelope deviation (AED) can indicate how well the methods perform. The AED, denoted \bar{d} , of a complete frame consisting of i image lines is defined as

$$\bar{d} = \frac{1}{IN} \sum_{i=1}^I \sum_{n=1}^N d_i(n) \quad (4.3)$$

However, the information in the AED is affected by the presence and dominance of a few larger deviations that occur due the zero crossings of the original signal envelopes. A high average deviation could therefore indicate a large AED, or a large envelope deviation in a single point. Therefore, one must also consider the standard deviation of the envelope deviation (SED). The SED, denoted σ_d , for a complete frame consisting of i image lines is defined as

$$\sigma_d = \sqrt{\frac{1}{IN} \sum_{i=1}^I \sum_{n=1}^N (d_i(n) - \bar{d})^2} \quad (4.4)$$

Together, AED and SED provide a good measure of the quantitative performance of the methods, and an overview is given in Tab. 4.1. However, the information is heavily compressed. To prevent losing potential insight into the methods performance, it is useful to evaluate the signal envelope deviation at each point in the images. Therefore, this deviation is visualised in Fig. 4.2 through Fig. 4.9, providing a ground for evaluation which sits between the regimes of quantitative, and qualitative assessment.

Table 4.1: Interpolation performance

Method	Noise suppression	Line Density	Figure	AED	SED
BRI	No	64	4.2	0.35	14.54
		128	4.3	0.33	52.18
	Yes	64	4.6	0.38	52.18
		128	4.7	0.53	192.05
BDI	No	64	4.4	0.11	4.25
		128	4.5	0.17	15.55
	Yes	64	4.8	0.07	5.30
		128	4.9	0.13	54.85

4.1 The CIRS Phantom

The CIRS phantom which was used as the imaging object when acquiring the data presented in this chapter has some prominent features which will be referred to in the text. A cross-sectional schematic of the phantom is shown in Fig. 4.1, where the imaging region seen in Fig. 4.2 through Fig. 4.9 is indicated by a red outline.

The schematic of the CIRS phantom contains some indicators which point out the important features of the phantom. With reference to Fig. 4.1;

1. Vertically positioned steel wires with a diameter of 100 μm , and a spacing of 10 mm.
2. Vertically positioned anechoic stepped cylinders with diameters in the range 1 mm to 3 mm.
3. Horizontally positioned steel wires with a diameter of 100 μm , and a spacing of 10 mm at 4 cm depth.
4. Horizontally positioned steel wires with a diameter of 100 μm , and a spacing of 20 mm at 9 cm depth.
5. Horizontally positioned, cylindric gray scale targets, with contrast resolutions of -6,-3,+3,+6, and $>+15$ dB. The diameters of the cylinders are 10 mm, and they are located at a depth of 11.5 cm.
6. The left hand side wall of the phantom.

These structures will be referred to as *Features* in the following sections.

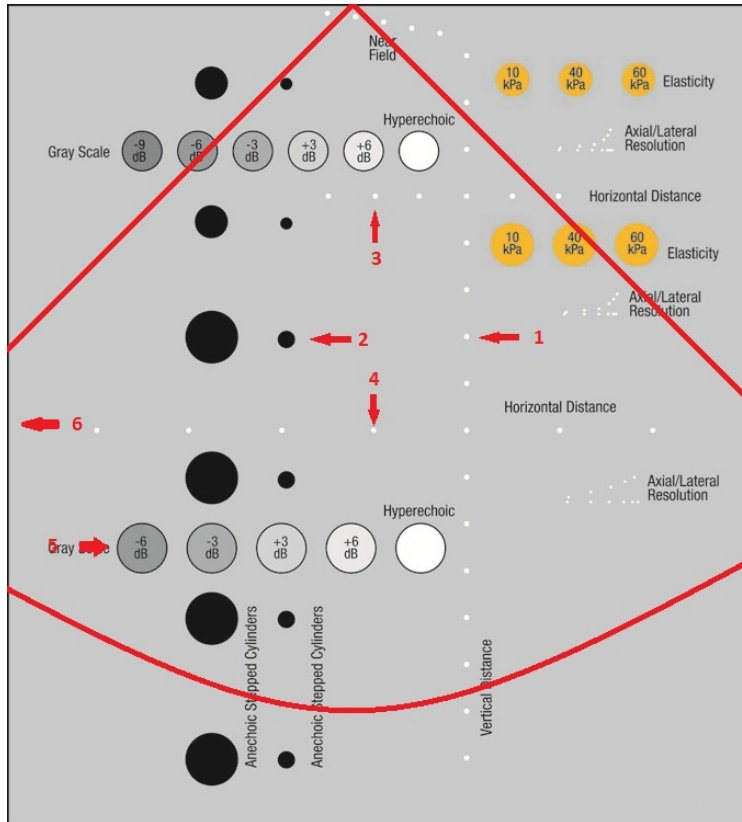


Figure 4.1: A cross-sectional schematic of the CIRS phantom, with the imaging region highlighted.

4.2 Signal Envelope

The signal envelope of the interpolated data and the original data are shown in Fig. 4.2 through Fig. 4.5. In Fig. 4.2 and Fig. 4.3 the interpolation was done using BRI, using an initial line density of 64 and 128 lines per frame, respectively. The images made using BRI thus have original line densities of 32 and 64 lines per frame, respectively, with no adjustment to transmit or receive parameters.

The images in Fig. 4.4 and Fig. 4.5 were produced using BDI, using initial line densities of 64 and 128 lines per frame, respectively. The interpolated images use different line densities for the acquisition with positive and negative LF pressure. 64 and 128 lines per frame were acquired with negative LF pressure, whereas only 32 and 64 lines were acquired using positive LF pressure. Again, no adjustments were made to imaging parameters between acquisitions.

Assessing the quality of the BRI technique visually and qualitatively, one can see that the method produces lateral smearing of the image, causing structures such as the echogenic wires of the phantom (Features 1,3 and 4) to become less pronounced. The wires can be seen as small, white dots in the images. Furthermore, the hypoechoic regions, located in a vertical line in the centre of the images (Feature 2), also become ill-defined when using BRI. As the line density is increased, the image with interpolated data seems to resemble the image with original data more closely. The perceived improvement is contrary to the quantitative evaluation in Tab. 4.1, which indicates that increased line density does not affect AED, but increases the SED substantially.

Performing beam interpolation with the BDI technique produces the results in Fig. 4.4 and Fig. 4.5. The figures in Tab. 4.1 suggest that the method produces images with interpolated data that resembles images with original data more closely than the BRI technique, for both line densities. The contrast resolution of the steel wires (Features 1, 3 and 4) is better, with less lateral smearing, and the borders of the low echogenic regions (Feature 2) are more clearly defined.

From the difference images, it can also clearly be seen that the BDI technique yields better results, particularly when using low line density. However, as the signal-to-noise ratio (SNR) decreases with depth, both of the techniques struggle to correctly interpolate the data, and the error increases. This is clearly seen beyond the wall of the phantom itself, which can be seen as a strongly scattering white vertical line on the left hand side of the images (Feature 6). Beyond this line, the signal is mostly noise, since practically no signal can be detected outside the borders of the phantom. However, the wall of the phantom is itself represented well by both of the techniques, implying that both of the techniques benefit from a good SNR.

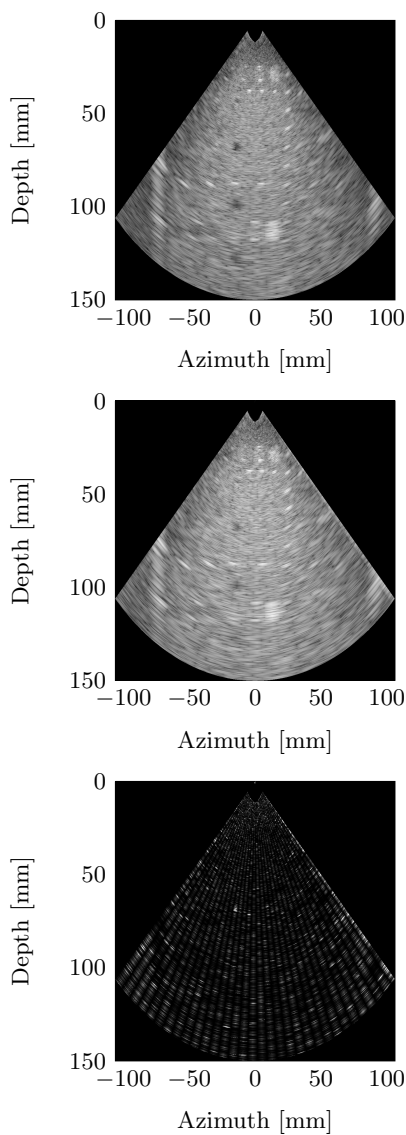


Figure 4.2: Relative difference in the signal envelope caused by BRI when transmitting with a positive LF amplitude, using a line density of 64 lines per frame.

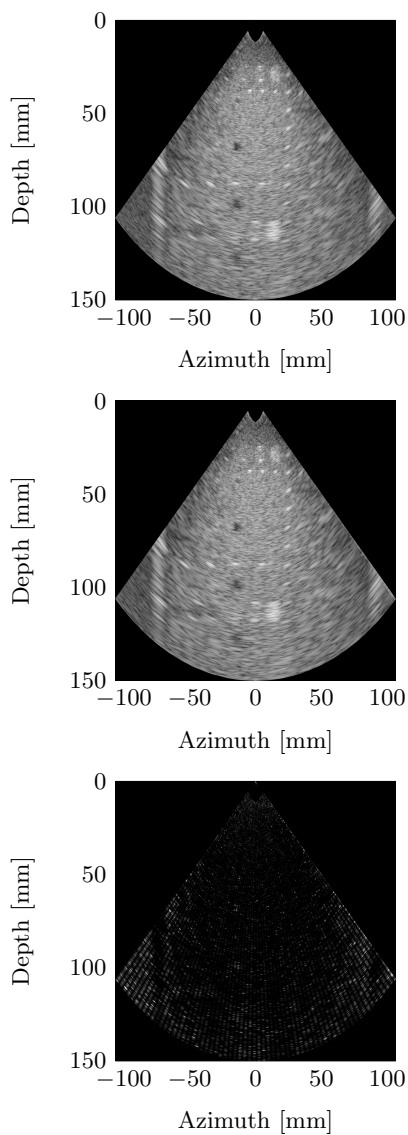


Figure 4.3: Relative difference in the signal envelope caused by BRI when transmitting with a positive LF amplitude, using a line density of 128 lines per frame.

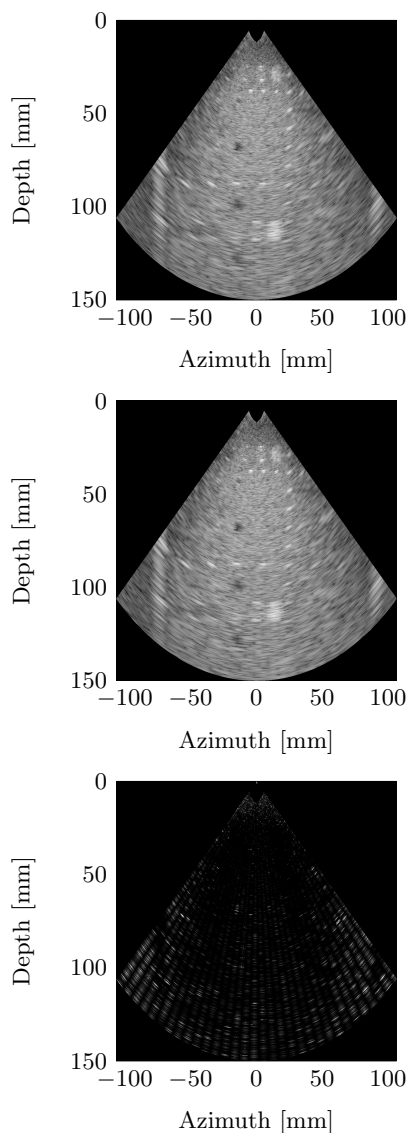


Figure 4.4: Relative difference in the signal envelope caused by BDI when transmitting with a positive LF amplitude, using a line density of 64 lines per frame.

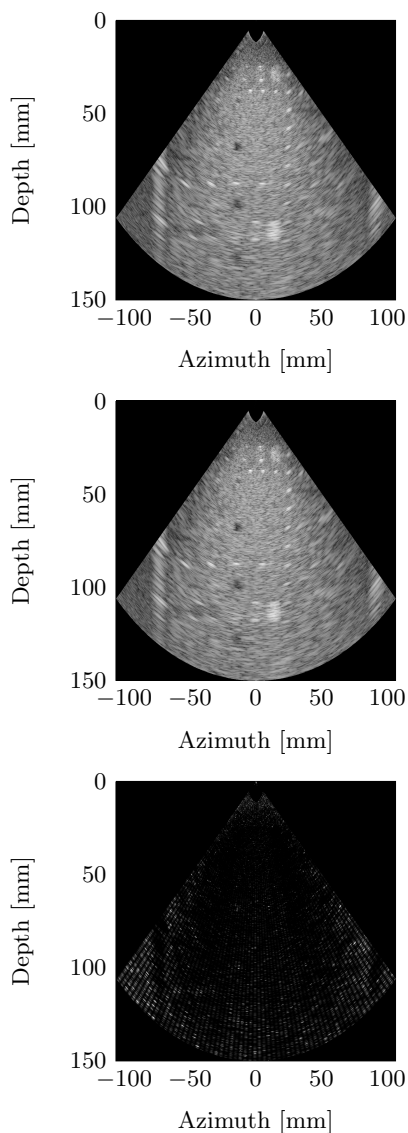


Figure 4.5: Relative difference in the signal envelope caused by BDI when transmitting with a positive LF amplitude, using a line density of 128 lines per frame.

4.3 Signal Envelope after Noise Suppression

In Fig. 4.6 through Fig. 4.9, the noise suppression using original and interpolated data are compared. The original data is visualised in the top images, the interpolated data is visualised in the middle, and the relative difference between the two is shown in at the bottom of each set of figures. In Fig. 4.6 and Fig. 4.7 the interpolation was done using BRI, using an initial line density of 64 and 128 lines per frame, respectively. The images made using BRI thus have original line densities of 32 and 64 lines per frame, respectively, with no adjustment to transmit or receive parameters.

The images in Fig. 4.8 and Fig. 4.9 were produced using BDI, using initial line densities of 64 and 128 lines per frame, respectively. The interpolated images use different line densities for the acquisition with positive and negative LF pressure. 64 and 128 lines per frame were acquired with negative LF pressure, whereas only 32 and 64 lines were acquired using positive LF pressure. Again, no adjustments were made to imaging parameters between acquisitions.

All the images contain radial lines where the magnitude of the image drops. These are located in the same directions in all of the images, and are assumed to be closely related to the estimated non-linear propagation delay in that direction. These lines will be discussed further in Ch. 5.

Again, starting with the quantitative results in Tab. 4.1, it can be seen that the AED and SED of the noise suppressed images is better when using BDI compared to BRI. The error is around 20% to 25% less with BDI than with BRI. Additionally, the numbers show that the SED increases with increased line density, as is the case without noise suppression.

The increase in SED with line density, which is particularly dramatic in the case of BRI, is hard to recognize in the difference images. The difference image becomes darker when the line density is increased, indicating that the overall error decreases. The overall increase in SED could be due to certain dominant sample values in which either of the denominators in Eq. (4.1), Eq. (4.2), Eq. (3.42), or Eq. (3.43) could be close to 0.

By comparing some of the features in the images, the difference in performance can be seen with the naked eye. Images made with BRI struggle to resolve the deep, lowly echogenic regions in the bottom left corner of the images (Feature 5), particularly with low line density. These three circular structures which are arranged horizontally in the images, can be picked out more easily in the images produced with BDI. Furthermore, the vertically aligned black circles in the centre of the images (Feature 2) are also clearer in the BDI images. BDI also outperforms low line density BRI when it comes to visualising the steel wires (Features 1, 3 and 4). These are clearly more blurry in Fig. 4.6, compared to the other images.

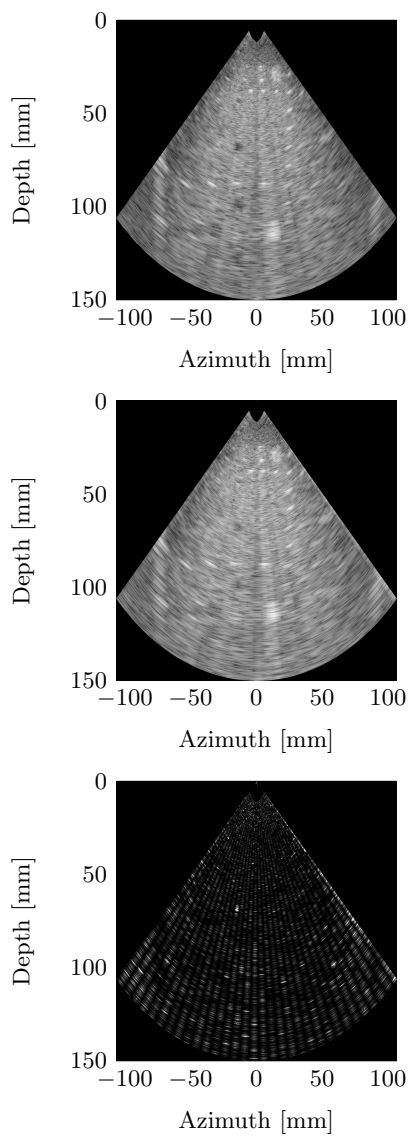


Figure 4.6: Relative difference in suppression, caused by BRI, using a line density of 64 lines per frame.

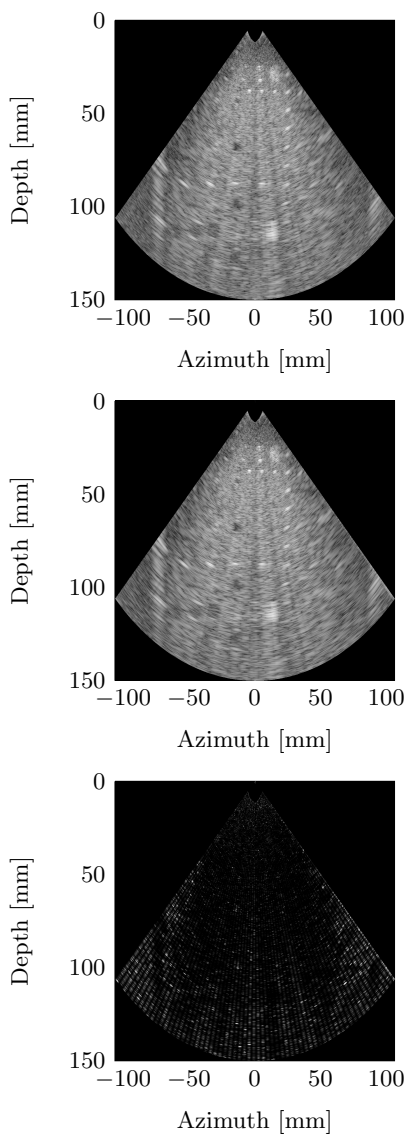


Figure 4.7: Relative difference in suppression, caused by BRI, using a line density of 128 lines per frame.

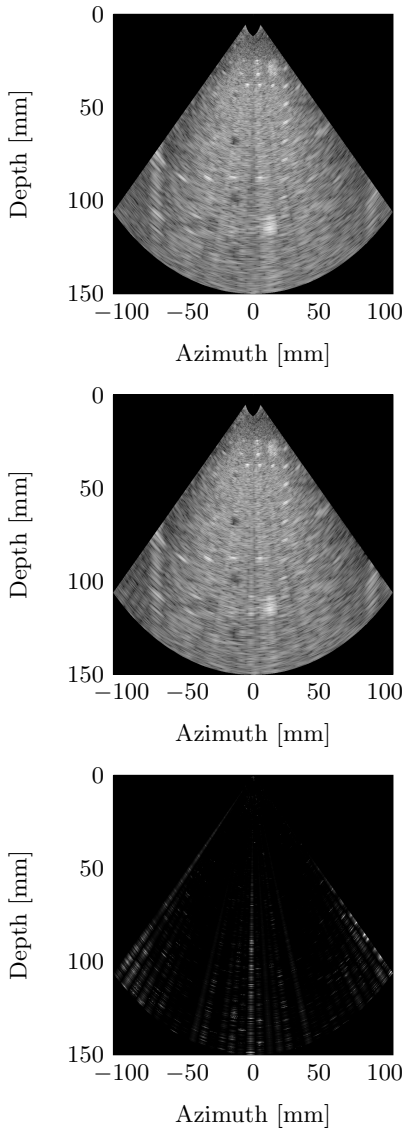


Figure 4.8: Relative difference in suppression, caused by BDI, using a line density of 64 lines per frame.

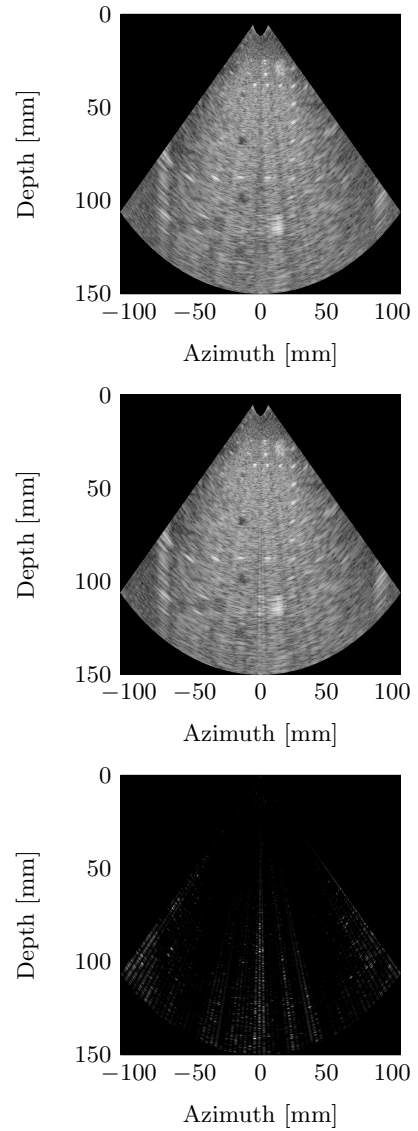


Figure 4.9: Relative difference in suppression, caused by BDI, using a line density of 128 lines per frame.

Discussion

The present chapter discusses the results presented in [Ch. 4](#). The difference in performance between BRI and BDI is outlined and discussed. The dataset that was available to test BRI and BDI on in this thesis was heavily influenced by the set-up of the scanner and the available hardware. Unfortunately, the hardware of the imaging system proved to be malfunctioning and beyond repair, which affected the results. The relation between hardware function and interpolation method performance is therefore also discussed. The imaging system is described in [App. A](#), and the hardware deficiency is thoroughly documented in [App. G](#).

5.1 Effects of Hardware Malfunction

In ultrasound imaging, the probe is a highly essential part of the imaging system. If the probe is badly designed or manufactured, the images produced by the system will have low quality. In SURF imaging, the LF array is badly designed or manufactured if it cannot transmit an LF sound pressure pulse that co-propagates with the HF pulse in such a way that the HF pulse is subjected to near constant ambient pressure as it travels into the tissue. This is the most basic function that the LF array serves. Losing this ability renders the LF array as a rather expensive and unnecessary addition to the probe architecture.

Ideally, the LF array should consist of homogeneous elements, which allows the LF sound beam to be steered in the same directions as the HF beam. The pulse complex consisting of the two pulses will then propagate in a predictable manner, with a geometrical behaviour like the arrays described in [Angelsen \[63\]](#). It is then possible to predict, for instance, the development of NPD with increasing depth. When an array contains malfunctioning elements that are either fused together or not functioning at all, it becomes harder to find a transmission set-up that provides LF pulses leading to a nice development of NPD with depth.

In the *Skolmen* probe, there were a considerable number of malfunctioning elements, which is shown in App. G, and in particular Fig. G.16. This caused the local LF pressure around the propagating HF pulses to behave far more erratically than intended, particularly when steering angles were applied to the LF beam. As a result of this, the estimated NPD in each direction varies substantially from one imaging line to the next. It even changes sign, indicating that a negative LF polarity causes the HF pulse to travel faster than it does with positive LF polarity. This is unexpected, and not physically viable unless the phase relation between the HF and LF pulses is changed due to the malfunctioning array, so that the LF polarity observed by the HF pulse is effectively inverted. In other words, at certain steering angles the malfunctioning array causes the HF pulse to be located in the trough of an LF pulse, rather than at a peak, or vice versa.

The erratic manipulation of the HF pulse by the LF pressure could be detrimental to both of the interpolation methods in this thesis. The interference pattern in the RF data which is interpolated in BRI is not only dependent on the tissue, but of the LF and HF beams as well. Interference patterns from two adjacent imaging lines may be fairly similar to one another if the beams satisfy the angular sampling criterion in Eq. (3.29), and LF pressure is fairly equal in the two beams. However, changes in LF pressure along one of the lines will change the interference pattern, causing an interpolation between the two lines to take a value that is more or less random with respect to the value that would have been obtained if data was acquired rather than interpolated. For BDI, one of the criteria for achieving good performance is that the NPD does not change significantly between image lines. Since NPD is directly dependent on LF pressure and polarity, the LF pressure should be as constant as possible when moving from one line to the next.

The probe malfunction did not only cause much of the time allocated to this project to be spent on error checking and needless software debugging. It also made the results from the beam interpolation more ambiguous. The extent to which one can be conclusive in recommending the use of the methods is therefore limited.

5.2 Interpolation Method Quality

Results from using BRI and BDI to create artificial image data from sparsely acquired acoustic data were shown in Ch. 4. The chapter comments briefly on the quantitative and qualitative performance of each of the methods, both of which will be discussed further in this section.

In Tab. 4.1, it was shown that BDI outperforms BRI when performance is measured in average envelope deviation (AED) and standard deviation of the envelope deviation (SED), in particular for low line density. The results can be attributed to the fact that BDI uses acquired image data from each imaging

direction. Thus, the interpolated data is constructed using a direction-specific RF signal, meaning that the same collection of scatterers contribute to the original and interpolated signals. BRI is not based on the scatterers that are located in the direction which the data is supposed to represent, rather, it is based on two sets of different scatterers. This produces slightly different received RF signals, which form a basis for a *prediction* of what the medium may look like in the direction that is represented by the interpolated data. BRI and BDI are both predictive methods, but the prediction of the scatterers based on the received RF signals seems further from the truth than a prediction based on the non-linear propagation delay.

The qualitative assessment of the methods seems more interesting, and in particular the difference images of Ch. 4. These images give an interesting insight into which conditions produce interpolated data that resemble real data more closely. The most important requirement for good performance seems to be a good SNR. The quality of the methods deteriorate as the SNR drops. This can be explained by noting that as the SNR drops, the signal becomes more random in nature and the correlation of the signals in two different directions becomes less. This effect causes BRI to fail. Increased randomness in the signal also produces less detectable difference between data acquired using positive and negative LF pressure on transmission. This causes the estimation of non-linear propagation delay (NPD) to break down, which in turn means that BDI produces less reliable results.

After processing to suppress reverberations in the images, some artefacts can be seen using both of the methods. The patterns appear in the original images, as well as in the images containing interpolated data. These lines were found to be linked with the estimation of NPD, and the estimation of first, $\hat{\tau}$, and third, $\hat{\tau}_n$, order delays. These were estimated using a least squares method fitting a third order polynomial to peaks on the NPD curve, described in Sec. 3.3. The estimation assumes that the NPD is close to linear with depth, so an erratic NPD could lead to bad estimates, and consequently to erroneous suppression. The effect of such bad estimates can be seen in the last images in Ch. 4, where suppression using BDI yields unequal results between original and interpolated data.

Finally, the methods can be compared with the naked eye, by comparing images produced with the two methods. From the results seen in Ch. 4, it is tempting to conclude that BDI produces images that are more clearly defined than those produced with BRI, in particular when line density is low. However, the performance can at best be described as marginally better, and the trade-off between image quality and frame rate could well render BDI superfluous, especially when imaging at larger depths.

5.3 Practical Experiences

There were a number of practical learning experiences during the work on this thesis. Firstly, the time spent doing experimental studies to verify the functionality of the imaging system, was prolonged. This was partly due to a lacking amount of documentation of the scanner software, which had to be modified. Proper documentation of highly intricate systems is crucial in order to foster effective research projects. Other delaying factors included erroneous hardware documentation, and the set-up of the lab experiments.

The field that was emitted by the transducer were mostly studied in a situation where the transducer was radiating in a direction normal to the face of the probe, *i.e.* with no steering delays applied. By not doing measurements of the radiated field in other directions, the problem of fused elements could not be observed from the water tank measurements. If the same beam profile measurements had been made for different transmission directions, the problem may have been discovered earlier, and the work could potentially have been done with different equipment.

The results of the DC inter-channel resistance measurements, presented in Sec. G.5.3, illuminated the malfunction of the probe well. The measurement was also very simple, requiring only a multimeter to perform. This measurement was not done by Myhre [64], but the current body of work shows that it definitely should be one of the fundamental measurements conducted to verify probe function because of its unequivocal results and simplicity.

5.4 Conclusions

It has been shown that the two interpolation techniques presented in this thesis produce fairly similar results. By sacrificing frame rate to use BDI in stead of BRI, the quality of the interpolated images becomes somewhat better when using low line density and a shallow imaging depth. Generally, though, both methods provide fair results when SNR is good. Furthermore, both of the methods benefit from minimizing the difference in LF pressure between transmit beams. However, due to the low quality of the dataset that was available for study in this thesis, one can draw no conclusion regarding which of the methods is most advantageous to use.

5.5 Future Work

There are a lot of factors that affect how well interpolation between beams may work, ranging from linear effects such as phase front aberration, beam widths, and the effect of beam steering, to SURF related effects such as SURF aberration,

development of NPD, the presence of PFD and PFM, and the various schemes for estimating these. Further work should be done on determining which of these effects are important for the interpolation performance, and which may be ruled out as insignificant.

In SURF imaging, it is of interest to acquire data in each direction using multiple LF transmit pressures. Particularly when examining moving structures such as the heart. Therefore, the techniques should be tested with moving structures. It would also be interesting to see if one could create multiple interpolated beams with different LF pressures in a single direction.

Finally, the quality of these methods can only really be put to the test by clinicians. The methods must therefore be implemented to operate in real-time on a scanner, and be assessed qualitatively in a case-controlled study.

Bibliography

- [1] Farlex, Inc. The Free Online Dictionary, 2013. URL <http://www.thefreedictionary.com/>. 1051 County Line Road Suite 100, Huntingdon Valley, PA 19006.
- [2] M Matsuzaki, Y Toma, and R Kusunokawa. Clinical applications of transesophageal echocardiography. *Circulation*, 82(3):709–22, 1990. doi: 10.1161/01.CIR.82.3.709. URL <http://circ.ahajournals.org/content/82/3/709.short>.
- [3] G S Hillis and P Bloomfield. Basic transthoracic echocardiography. *BMJ*, 330(7505):1432–1436, 6 2005. doi: 10.1136/bmj.330.7505.1432.
- [4] T A Ports, J Cogan, N B Schiller, and E Rapaport. Echocardiography of left ventricular masses. *Circulation*, page 528, 1978.
- [5] M B Al-Nouri, K Patel, W D Johnson, M L Kamath, and D H Schmidt. The sensitivity and specificity of two-dimensional echocardiography in detecting left ventricular thrombi. *Circulation*, 62 (suppl III):III–21, 1980.
- [6] G S Reeder, A J Tajik, and J B Seward. Left ventricular mural thrombus: two dimensional echocardiographic diagnosis. *Mayo Clinic Proceedings*, 56: 82, 1981.
- [7] J R Stratton, G W Lighty, A S Pearlman, and J L Ritchie. Detection of left ventricular thrombus by two-dimensional echocardiography: sensitivity, specificity, and causes of uncertainty. *Circulation*, 66(1):156–66, 1982. doi: 10.1161/01.CIR.66.1.156. URL <http://circ.ahajournals.org/content/66/1/156.abstract>.
- [8] M D Ezekowitz, D A Wilson, E O Smith, R D Burow, L H Harrison Jr., D E Parker, R C Elkins, M Peyton, and F B Taylor. Comparison of indium-111 platelet scintigraphy and two-dimensional echocardiography in the diagnosis of left ventricular thrombi (abstract). *New England Journal of Medicine*, 306(25):1509–1513, 1982. URL <http://www.nejm.org/doi/full/10.1056/NEJM198206243062502>.

- [9] C A Visser, G Kan, G K David, K I Lie, and D Durrer. Two dimensional echocardiography in the diagnosis of left ventricular thrombus. a prospective study of 67 patients with anatomic validation. *CHEST Journal*, 83(2):228–232, 1983. doi: 10.1378/chest.83.2.228. URL <http://dx.doi.org/10.1378/chest.83.2.228>.
- [10] M A Alpert, R J Carney, G C Flaker, J F Sanfelippo, R R Webel, and D L Kelly. Sensitivity and specificity of two-dimensional echocardiographic signs of mitral valve prolapse. *The American Journal of Cardiology*, 54(7): 792 – 796, 1984. ISSN 0002-9149. doi: 10.1016/S0002-9149(84)80210-6. URL <http://www.sciencedirect.com/science/article/pii/S0002914984802106>.
- [11] P S Douglas, M J Garcia, D E Haines, W W Lai, W J Manning, A R Patel, M H Picard, D M Polk, M Ragosta, R P Ward, and R B Weiner. ACCF/ASE/AHA/ASNC/HFSA/HRS/SCAI/SCCM/SCCT/SCMR 2011 Appropriate Use Criteria for Echocardiography: A Report of the American College of Cardiology Foundation Appropriate Use Criteria Task Force, American Society of Echocardiography, American Heart Association, American Society of Nuclear Cardiology, Heart Failure Society of America, Heart Rhythm Society, Society for Cardiovascular Angiography and Interventions, Society of Critical Care Medicine, Society of Cardiovascular Computed Tomography, and Society for Cardiovascular Magnetic Resonance Endorsed by the American College of Chest Physicians. *Journal of the American College of Cardiology*, 57(9):1126 – 1166, 2011. ISSN 0735-1097. doi: 10.1016/j.jacc.2010.11.002. URL <http://www.sciencedirect.com/science/article/pii/S0735109710044694>.
- [12] S Thanigaraj, K B Schechtman, and J E Prez. Improved echocardiographic delineation of left ventricular thrombus with the use of intravenous second-generation contrast image enhancement. *Journal of the American Society of Echocardiography*, 12(12):1022 – 1026, 1999. ISSN 0894-7317. doi: 10.1016/S0894-7317(99)70097-0. URL <http://www.sciencedirect.com/science/article/pii/S0894731799700970>.
- [13] M B Srichai, C Junor, L L Rodriguez, A E Stillman, R A Grimm, M L Lieber, J A Weaver, N G Smedira, and R D White. Clinical, imaging, and pathological characteristics of left ventricular thrombus: A comparison of contrast-enhanced magnetic resonance imaging, transthoracic echocardiography, and transesophageal echocardiography with surgical or pathological validation. *American Heart Journal*, 152(1):75 – 84, 2006. ISSN 0002-8703. doi: 10.1016/j.ahj.2005.08.021. URL <http://www.sciencedirect.com/science/article/pii/S0002870305008732>.
- [14] N Mansencal, I A Nasr, R Pillière, J-C Farcot, T Joseph, P Lacombe, and O Dubourg. Usefulness of contrast echocardiography for assessment of left ventricular thrombus after acute myocardial infarction. *The American*

-
- Journal of Cardiology*, 99(12):1667 – 1670, 2007. ISSN 0002-9149. doi: 10.1016/j.amjcard.2007.01.046. URL <http://www.sciencedirect.com/science/article/pii/S0002914907004559>.
- [15] J W Weinsaft, R J Kim, M Ross, D Krauser, S Manoushagian, T M LaBounty, M D Cham, J K Min, K Healy, Y Wang, M Parker, M J Roman, and R B Devereux. Contrast-enhanced anatomic imaging as compared to contrast-enhanced tissue characterization for detection of left ventricular thrombus. *JACC: Cardiovascular Imaging*, 2(8):969 – 979, 2009. ISSN 1936-878X. doi: 10.1016/j.jcmg.2009.03.017. URL <http://www.sciencedirect.com/science/article/pii/S1936878X09003799>.
- [16] J W Weinsaft, H W Kim, A L Crowley, I Klem, C Shenoy, L Van Assche, R Brosnan, D J Shah, E J Velazquez, M Parker, R M Judd, and R J Kim. LV thrombus detection by routine echocardiography: Insights into performance characteristics using delayed enhancement CMR. *JACC: Cardiovascular Imaging*, 4(7):702 – 712, 2011. ISSN 1936-878X. doi: 10.1016/j.jcmg.2011.03.017. URL <http://www.sciencedirect.com/science/article/pii/S1936878X11003111>.
- [17] V L Roger, A S Go, D M Lloyd-Jones, R J Adams, J D Berry, T M Brown, M R Carnethon, S Dai, G de Simone, E S Ford, C S Fox, H J Fullerton, C Gillespie, K J Greenlund, S M Hailpern, J A Heit, P M Ho, V J Howard, B M Kissela, S J Kittner, D T Lackland, J H Lichtman, L D Lisabeth, D M Makuc, G M Marcus, A Marelli, D B Matchar, M M McDermott, J B Meigs, C S Moy, D Mozaffarian, M E Mussolino, G Nichol, N P Paynter, W D Rosamond, P D Sorlie, R S Stafford, T N Turan, M B Turner, N D Wong, and J Wylie-Rosett. Heart disease and stroke statistics – 2011 update: A report from the American Heart Association. *Circulation*, 123(4):e18–e209, 2011. doi: 10.1161/CIR.0b013e3182009701. URL <http://circ.ahajournals.org/content/123/4/e18.short>.
- [18] K Hisanaga, A Hisanaga, K Nagata, and Y Ichie. Transesophageal cross-sectional echocardiography. *American Heart Journal*, 100(5):605 – 609, 1980. ISSN 0002-8703. doi: [http://dx.doi.org/10.1016/0002-8703\(80\)90223-9](http://dx.doi.org/10.1016/0002-8703(80)90223-9). URL <http://www.sciencedirect.com/science/article/pii/0002870380902239>.
- [19] K Hisanaga, A Hisanaga, N Hibi, K Nishimura, and T Kambe. High speed rotating scanner for transesophageal cross-sectional echocardiography. *The American Journal of Cardiology*, 46(5):837 – 842, 1980. ISSN 0002-9149. doi: [http://dx.doi.org/10.1016/0002-9149\(80\)90437-3](http://dx.doi.org/10.1016/0002-9149(80)90437-3). URL <http://www.sciencedirect.com/science/article/pii/0002914980904373>.
- [20] B Rajagopalan, E P DiMagno, J F Greenleaf, P T Regan, J Buxton, P S Green, and J W Whitaker. Transesophageal ultrasonic imaging of the heart. In K Y Wang, editor, *Acoustical Imaging*, volume 9 of *Acoustical Imaging*, pages 555–567. Springer US, 1980. ISBN 978-1-4684-3757-7. doi:

- 10.1007/978-1-4684-3755-3_34. URL
http://dx.doi.org/10.1007/978-1-4684-3755-3_34.
- [21] J Souquet, P Hanrath, L Zitelli, P Kremer, B A Langenstein, and M Schluter. Transesophageal phased array for imaging the heart. *Biomedical Engineering, IEEE Transactions on*, BME-29(10):707–712, 1982. ISSN 0018-9294. doi: 10.1109/TBME.1982.324864.
- [22] M Schlüter, B A Langenstein, J Polster, P Kremer, J Souquet, S Engel, and P Hanrath. Transoesophageal cross-sectional echocardiography with a phased array transducer system. technique and initial clinical results. *British Heart Journal*, 48(1):67–72, 1982. doi: 10.1136/hrt.48.1.67. URL <http://heart.bmj.com/content/48/1/67.abstract>.
- [23] C Chen, D Koschyk, C Hamm, B Sievers, W Kupper, and W Bleifeld. Usefulness of transesophageal echocardiography in identifying small left ventricular apical thrombus. *Journal of the American College of Cardiology*, 21(1):208 – 215, 1993. ISSN 0735-1097. doi: 10.1016/0735-1097(93)90738-M. URL <http://www.sciencedirect.com/science/article/pii/073510979390738M>.
- [24] W G Daniel, C Angermann, R Engberding, R Erbel, P Hanrath, S Iliceto, W Kasper, and C A Visser. Transesophageal echocardiography in patients with cerebral ischemic events and arterial embolism - a european multicenter study (abstract). *Circulation*, 80 (suppl II):II-473, 1989. ISSN 0735-1097.
- [25] A C Pearson, A J Labovitz, S Tatineni, and C R Gomez. Superiority of transesophageal echocardiography in detecting cardiac source of embolism in patients with cerebral ischemia of uncertain etiology. *Journal of the American College of Cardiology*, 17(1):66 – 72, 1991. ISSN 0735-1097. doi: 10.1016/0735-1097(91)90705-E. URL <http://www.sciencedirect.com/science/article/pii/073510979190705E>.
- [26] W Aschenberg, M Schlüter, P Kremer, E Schröder, V Siglow, and W Bleifeld. Transesophageal two-dimensional echocardiography for the detection of left atrial appendage thrombus. *Journal of the American College of Cardiology*, 7(1):163 – 166, 1986. ISSN 0735-1097. doi: 10.1016/S0735-1097(86)80275-3. URL <http://www.sciencedirect.com/science/article/pii/S0735109786802753>.
- [27] W G Daniel, U Nellessen, E Schröder, B Nonnast-Daniel, P Bednarski, P Nikutta, and P R Lichtlen. Left atrial spontaneous echo contrast in mitral valve disease: An indicator for an increased thromboembolic risk. *Journal of the American College of Cardiology*, 11(6):1204 – 1211, 1988. ISSN 0735-1097. doi: 10.1016/0735-1097(88)90283-5. URL <http://www.sciencedirect.com/science/article/pii/0735109788902835>.

-
- [28] G Pop, G R Sutherland, P J Koudstaal, T W Sit, G de Jong, and J R Roelandt. Transesophageal echocardiography in the detection of intracardiac embolic sources in patients with transient ischemic attacks. *Stroke*, 21(4):560–5, 1990. doi: 10.1161/01.STR.21.4.560. URL <http://stroke.ahajournals.org/content/21/4/560.abstract>.
- [29] B Schneider, P Hanrath, P Vogel, and T Meinertz. Improved morphologic characterization of atrial septal aneurysm by transesophageal echocardiography: Relation to cerebrovascular events. *Journal of the American College of Cardiology*, 16(4):1000 – 1009, 1990. ISSN 0735-1097. doi: 10.1016/S0735-1097(10)80354-7. URL <http://www.sciencedirect.com/science/article/pii/S0735109710803547>.
- [30] B Cujec, P Polasek, C Voll, and A Shuaib. Transesophageal echocardiography in the detection of potential cardiac source of embolism in stroke patients. *Stroke*, 22(6):727–733, 1991. doi: 10.1161/01.STR.22.6.727. URL <http://stroke.ahajournals.org/content/22/6/727.abstract>.
- [31] G Zenker, R Erbel, G Krämer, S Mohr-Kahaly, M Drexler, K Harnoncourt, and J Meyer. Transesophageal two-dimensional echocardiography in young patients with cerebral ischemic events. *Stroke*, 19(3):345–8, 1988. doi: 10.1161/01.STR.19.3.345. URL <http://stroke.ahajournals.org/content/19/3/345.abstract>.
- [32] M Born and E Wolf. *Principles of Optics - Electromagnetic Theory of Propagation, Interference and Diffraction of Light*. Pergamon Press Ltd., 1959.
- [33] B Ward, A C Baker, and V F Humphrey. Nonlinear propagation applied to the improvement of resolution in diagnostic medical ultrasound. *The Journal of the Acoustical Society of America*, 101(1):143–154, 1997. doi: 10.1121/1.417977. URL <http://link.aip.org/link/?JAS/101/143/1>.
- [34] J D Thomas and D N Rubin. Tissue harmonic imaging: Why does it work? *Journal of the American Society of Echocardiography*, 11(8):803 – 808, 1998. ISSN 0894-7317. doi: 10.1016/S0894-7317(98)70055-0. URL <http://www.sciencedirect.com/science/article/pii/S0894731798700550>.
- [35] P J A Frinking, A Bouakaz, J Kirkhorn, F J Ten Cate, and N de Jong. Ultrasound contrast imaging: current and new potential methods. *Ultrasound in Medicine & Biology*, 26(6):965 – 975, 2000. ISSN 0301-5629. doi: 10.1016/S0301-5629(00)00229-5. URL <http://www.sciencedirect.com/science/article/pii/S0301562900002295>.
- [36] F A Duck. Nonlinear acoustics in diagnostic ultrasound. *Ultrasound in Medicine & Biology*, 28(1):1 – 18, 2002. ISSN 0301-5629. doi: 10.1016/S0301-5629(01)00463-X. URL <http://www.sciencedirect.com/science/article/pii/S030156290100463X>.

- [37] T G Muir and E L Carstensen. Prediction of nonlinear acoustic effects at biomedical frequencies and intensities. *Ultrasound in Medicine & Biology*, 6(4):345 – 357, 1980. ISSN 0301-5629. doi: 10.1016/0301-5629(80)90004-6. URL <http://www.sciencedirect.com/science/article/pii/0301562980900046>.
- [38] E L Carstensen, W K Law, N D McKay, and T G Muir. Demonstration of nonlinear acoustical effects at biomedical frequencies and intensities. *Ultrasound in Medicine & Biology*, 6(4):359 – 368, 1980. ISSN 0301-5629. doi: 10.1016/0301-5629(80)90005-8. URL <http://www.sciencedirect.com/science/article/pii/0301562980900058>.
- [39] M D Harpen. Basic nonlinear acoustics: An introduction for radiological physicists. *Medical Physics*, 33(9):3241–3247, 2006. doi: 10.1118/1.2207128. URL <http://link.aip.org/link/?MPH/33/3241/1>.
- [40] R Hansen. *New Techniques for Detection of Ultrasound Contrast Agents*. PhD thesis, Norwegian University of Science and Technology, December 2003.
- [41] B A J Angelsen. *Ultrasound Imaging - Waves, Signals and Signal Processing*. Emantec AS, December 2000. URL <http://www.ultrasoundbook.com>.
- [42] R S C Cobbold. *Foundations of Biomedical Ultrasound*. Oxford University Press, 2007.
- [43] M F Hamilton and D T Blackstock, editors. *Nonlinear Acoustics*. Academic Press, 1998.
- [44] K Naugolnykh and L Ostrovsky. *Nonlinear Wave Processes in Acoustics*. Cambridge University Press, 1998.
- [45] B A J Angelsen. *Ultrasound Imaging - Waves, Signals and Signal Processing*, volume 1, chapter 4. Emantec AS, December 2000.
- [46] B A J Angelsen. *Ultrasound Imaging - Waves, Signals and Signal Processing*, volume 2, chapter 12. Emantec AS, December 2000.
- [47] R Hansen, S-E Måsøy, T F Johansen, and B A J Angelsen. Utilizing dual frequency band transmit pulse complexes in medical ultrasound imaging. *The Journal of the Acoustical Society of America*, 127(1):579–587, 2010. doi: 10.1121/1.3257584. URL <http://link.aip.org/link/?JAS/127/579/1>.
- [48] S-E Måsøy, Ø Standal, P Näsholm, T F Johansen, B A J Angelsen, and R Hansen. SURF imaging: In vivo demonstration of an ultrasound contrast agent detection technique. *Ultrasonics, Ferroelectrics and Frequency Control, IEEE Transactions on*, 55(5):1112–1121, 2008. ISSN 0885-3010. doi: 10.1109/TUFFC.2008.763.

-
- [49] R Hansen and B A J Angelsen. SURF imaging for contrast agent detection. *Ultrasonics, Ferroelectrics and Frequency Control, IEEE Transactions on*, 56(2):280–290, 2009. ISSN 0885-3010. doi: 10.1109/TUFFFC.2009.1037.
- [50] J M Rau. *Dual Frequency Band Ultrasound for Suppression of Multiple Scattering*. PhD thesis, Norwegian University of Science and Technology, May 2013.
- [51] T S Jahren. Suppression of multiple scattering and imaging of nonlinear scattering in ultrasound imaging. Master’s thesis, Norwegian University of Science and Technology, May 2013.
- [52] B A J Angelsen and R Hansen. 7A-1 SURF Imaging - A New Method for Ultrasound Contrast Agent Imaging. In *Ultrasonics Symposium, 2007. IEEE*, pages 531–541, 2007. doi: 10.1109/ULTSYM.2007.140.
- [53] B A J Angelsen and T A Tangen. Nonlinear imaging with dual band pulse complexes. Patent Application, May 2012.
- [54] B A J Angelsen. *Ultrasound Imaging - Waves, Signals and Signal Processing*, volume 1, chapter 3. Emantec AS, December 2000.
- [55] T Varslot and S-E Måsøy. Forward propagation of acoustic pressure pulses in 3d soft biological tissue. *Modeling, Identification and Control*, 27(3): 181–200, 2006. URL <http://www.ingentaconnect.com/content/nfa/mic/2006/00000027/00000003/art00005>.
- [56] J Kvam. Interactions between microbubbles and ultrasound: In vitro and in vivo observations. Master’s thesis, The Norwegian University of Science and Technology, June 2012.
- [57] B A J Angelsen. *Ultrasound Imaging - Waves, Signals and Signal Processing*, volume 2, chapter 7. Emantec AS, December 2000.
- [58] B A J Angelsen. *Ultrasound Imaging - Waves, Signals and Signal Processing*, volume 1, chapter 5. Emantec AS, December 2000.
- [59] Ø Standal, T A Tangen, and B A J Angelsen. P2D-4 A Phase Based Approach for Estimation and Tracking of Locally Variable Delays. In *Ultrasonics Symposium, 2007. IEEE*, pages 1583–1585, 2007. doi: 10.1109/ULTSYM.2007.398.
- [60] B A J Angelsen. Ultrasound assessment of contraction and relaxation deficiencies of the heart. Patent Application, August 2011.
- [61] B A J Angelsen. *Ultrasound Imaging - Waves, Signals and Signal Processing*, volume 2, chapter 8. Emantec AS, December 2000.

- [62] Computerized Imaging Reference Systems, Inc. (CIRS), 2013. URL <http://www.cirsinc.com/products/modality/67/multi-purpose-multi-tissue-ultrasound-phantom/>. 2428 Alameda Ave, Suite 316, Norfolk, Virginia 23513 USA.
- [63] B A J Angelsen. *Ultrasound Imaging - Waves, Signals and Signal Processing*, volume 1, chapter 6. Emantec AS, December 2000.
- [64] O F Myhre. Characterization of a dual-band piezoelectric ultrasound transducer – measurements and issues. Master’s Project, december 2012.
- [65] SURF Technoloy AS. URL <http://www.surftech.no/>. Richard Birkelands vei 2B, 7491 Trondheim, Norway.
- [66] Ultrasonix Medical Corporation, 2013. URL <http://www.ultrasonix.com/>. Richmond, BC, Canada.
- [67] ITT Interconnect Solutions. *Cannon DL series ZIF connectors*. 666 E. Dyer Rd, Santa Ana, Ca 92831, January 2009.
- [68] T F Johansen. *SURF Cardiac Probe: Phased Linear SURF Array*. SURF Technology A/S, Richard Birkelands vei 2B, N-7491 Trondheim, Norway. Confidential specification.
- [69] B A J Angelsen. *Ultrasound Imaging - Waves, Signals and Signal Processing*, volume 1, chapter 2. Emantec AS, December 2000.
- [70] D K Cheng. *Field and Wave Electromagnetics*. Addison-Wesley, second edition, 1989.
- [71] J D Larson. A new vibration mode in tall, narrow piezoelectric elements. In *1979 Ultrasonics Symposium*, pages 108 – 113, 1979.
- [72] S W Smith, Olaf T von Ramm, M E Haran, and F L Thurstone. Angular response of piezoelectric elements in phased array ultrasound scanners. *Sonics and Ultrasonics, IEEE Transactions on*, 26(3):185–191, may 1979.
- [73] R E McKeighan. Design guidelines for medical ultrasonic arrays. In *Proc. SPIE 3341, Medical Imaging 1998: Ultrasonic Transducer Engineering*, volume 2, 1998.
- [74] Ultrasonix Medical Corporation. URL http://www.ultrasonix.com/wikisonix/index.php?title=Category:Research_Documentation&action=pdfbook. Richmond, BC, Canada.
- [75] L deBruijn. *Probe Heating Measurements 4DL14-5/38*. SURF Technology A/S, Richard Birkelands vei 2B, N-7491 Trondheim, Norway.
- [76] J A Jensen and N B Svendsen. Calculation of pressure fields from arbitrarily shaped, apodized, and excited ultrasound transducers. *Ultrasonics, Ferroelectrics and Frequency Control, IEEE Transactions on*, 39(2):262–267, 1992. ISSN 0885-3010. doi: 10.1109/58.139123.

- [77] J A Jensen. FIELD: A program for simulating ultrasound systems. In *10th Nordicbaltic Conference On Biomedical Imaging, Supplement 1*, volume 4, pages 351–353, 1996.

Appendices

Listings

C.1	The <code>probes.xml</code> file used by Sonix	88
C.2	The GEN-General (Skolmenmm).xml configuration file	89
C.3	The <code>probes.xml</code> file used by the SURF library	93
C.4	The <code>probe.xml</code> file for <i>Skolmen</i>	94
C.5	The <code>applications.xml</code> file for <i>Skolmen</i>	95
C.6	The <code>ceus_2pulse.xml</code> file for <i>Skolmen</i>	96
E.1	Original <code>geometrybase.h</code> file	104
E.2	Original <code>geometrybase.cpp</code> file	104
E.3	Modified <code>geometrybase.h</code> file	105
E.4	Modified <code>geometrybase.cpp</code> file	105
E.5	Original <code>beamformer_1p25d.cpp</code> file (Part 1)	107
E.6	Modified <code>beamformer_1p25d.cpp</code> file (Part 1)	107
E.7	Original <code>beamformer_1p25d.cpp</code> file (Part 2)	108
E.8	Modified <code>beamformer_1p25d.cpp</code> file (Part 2)	108
E.9	Original <code>beamformer_1p25d.cpp</code> file (Part 3)	109
E.10	Modified <code>beamformer_1p25d.cpp</code> file (Part 3)	109
E.11	Original <code>helperfunctions.h</code> file	109
E.12	Modified <code>helperfunctions.h</code> file	109
E.13	Original <code>surflftxfe.cpp</code> file	110
E.14	Modified <code>surflftxfe.cpp</code> file	110
F.1	The GEN-Meas_2D_Field (Skolmenmm).xml configuration file . . .	111
F.2	The GEN-Phantom (Skolmenmm).xml configuration file	112

Imaging System

To be able to acquire experimental data with the application of the dual band technique described in Ch. 2, part of the research group at the Department of Circulation and Medical Imaging (ISB) at the Norwegian University of Science and Technology (NTNU) has co-operated with SURF Technology AS [65] to modify a Sonix MDP ultrasound scanner, manufactured by Ultrasonix Medical Corporation [66]. The modified system is based on the Sonix MDP, with hardware and software extensions which have been added in order to control a voltage pulser that is capable of driving the low frequency elements of custom dual-band array transducers. The details of the system is covered by Rau [50].

This chapter will give a short description of hardware components and software setup of the imaging system, alongside details about the dual-band array transducer, *Skolmen*, that was used to collect experimental data. Additional measurement systems were used for verification of pulse forms, transmit sequences and beam characteristics. The chapter will present the methods and results of these measurements.

A.1 Hardware

The dual-band imaging system comprises the Ultrasonix SonixMDP and custom hardware which is used to generate the low frequency signals. The current system uses a simplified version of the one specified by Rau [50], and a schematic overview can be seen in Fig. A.1.

The hardware consists of four main parts: the Ultrasonix SonixMDP scanner, the custom LF pulser, a connector interface PCB and the probe. No hardware modifications have been made to the scanner.

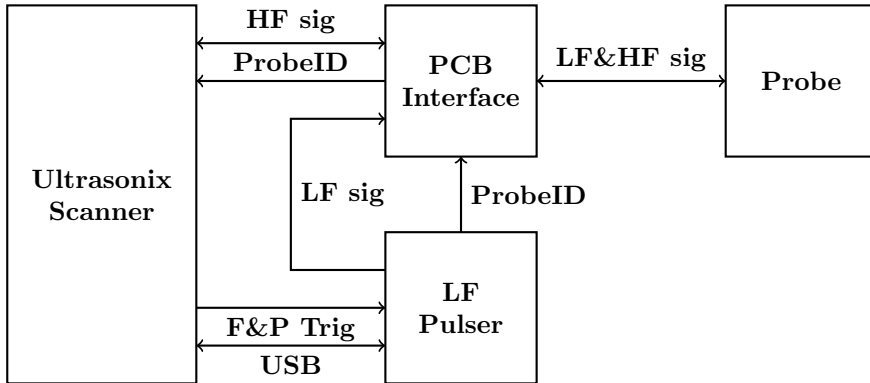


Figure A.1: A schematic overview of the hardware components in the dual-band imaging system.

The SonixMDP scanner is the core component of the SURF system, as it controls other external hardware via a USB link. Additionally, all processing related to beam-forming, manipulation of received signals and image reconstruction is done within the scanner. The HF front-end transmit electronics in the SonixMDP consists of 128 tri-state transmit pulser circuits capable of producing a maximum voltage of 96 V, peak-to-peak, and are clocked at 80 MHz. The number of receive channels on the system is 64, so for phased arrays the number of elements in the transducer should not exceed 64, since all channels are used simultaneously on reception. The scanner has the ability to do beam-forming on all transmit and receive channels, with the limitation that apodization cannot be applied on transmission.

The LF pulser is a tri-state pulser with 64 master output channels. In parallel with each master channel is a slave channel; hence each output has a corresponding optional parallel output. The pulser produces rectangular pulse trains according to a sequence specified by the SonixMDP. The transmit patterns for entire frames and all corresponding parameters are also loaded into the local memory of the pulser before transmission is initiated.

The connector interface routes the HF signals from the MDP scanner, and the LF signals produced by the LF pulser to a Cannon/ITT DLP408R [67], to which the probe connector is attached. It also connects a logic circuit in the LF pulser to the 5 Probe ID pins on the MDP scanner. These pins constitute a 5 bit code which inform the scanner which probe is connected. The software uses this configuration to identify the probe and set up parameters and available applications. For custom probes, like *Skolmen*, which lack this hard-wired configuration of ID pins the pins may be set by the logic circuit in the LF pulser. This ID can be specified by the user on the MDP scanner, which communicates the configuration to the LF pulser via the USB link. The interfacing PCB card is mounted directly to one of the output connectors on the MDP scanner.

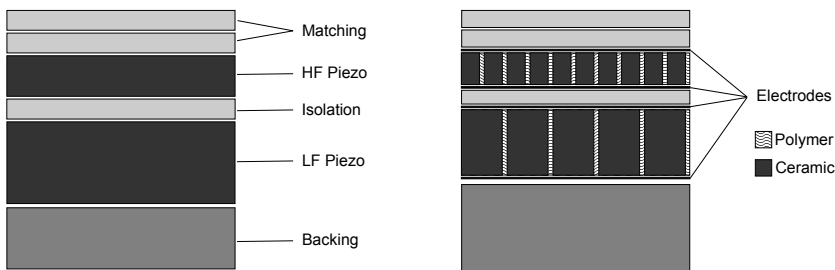
The probe is application specific, meaning that a probe is tailored for imaging a particular structure, *e.g.* the heart. Therefore, additional tuning hardware must be mounted in the probe connector housing, or that of the probe itself, since tuning components are highly dependent on transducer design.

A.2 Skolmen

Skolmen is a multilayered phased array transducer which is able to transmit pulse complexes consisting of a low frequency manipulation pulse and a high frequency imaging pulse. It was designed by SURF Technology AS for use in cardiac applications [68], and has a HF center frequency of 2.75 MHz, and a LF center frequency of 0.45 MHz.

A.2.1 Transducer stack

Piezoelectric transducer design is a field in itself; one which the present text will not go deeply into. However, the most basic considerations that must be taken into account when designing a transducer will be summarized to complete the reader's understanding of the ultrasound system. It is assumed that the reader is acquainted with the concept of acoustical impedance in one-dimensional systems [69], and has some knowledge of electrical circuits and transmission lines [70]. Further insight into transducer design and experimental validation can be found in texts by Larson [71], Smith et al. [72], McKeighan [73] and Angelsen [54].



(a) Stack with two piezoelectric layers.

(b) Stack showing composite piezoelectric layers with diced ceramics.

Figure A.2: Principal overview of dual-band transducer stacks. The transducer surface is at the top of the figures.

A cross-sectional view of a typical dual-band array transducer can be seen in Fig. A.2. It is constituted by two piezoelectric layers, an isolation layer, matching layers, and a backing. Note that the positive and ground electrodes connecting

the piezoelectric layers to the transmit and receive electronics of the ultrasound scanner are located at the back and front of the layers, respectively. Figure A.2b illustrates how the piezoelectric layers of array transducers are sub-diced into smaller elements, in order to be able to electronically steer the transmitted beams, and to simultaneously lower the effective characteristic acoustic impedance of the layers. This makes the requirements imposed on the matching and isolation layers less stringent and can thereby increase the performance of the transducer.

The large difference between the acoustic impedances of piezoelectric materials and biological tissue necessitates the use of acoustic matching layers at the front of the transducer. These elastic materials are selected so that the equivalent acoustic impedances at the front face of the piezoelectric layers are similar to the characteristic acoustic impedance of the piezoelectric material, depending on transducer application. The isolation layer, located between the two piezoelectric layers, is included in the design to prevent the HF layer vibrations from affecting the vibrations of the LF layer. The choice of material in this layer has a great impact on the maximum bandwidth of the transmitted pulse, since it affects the equivalent impedance at the back layer of the piezoelectric layer. If the mismatch in impedances is large at this interface, the HF layer becomes more resonant, resulting in more ringing in the pulse, lower maximum bandwidth, and larger peak pressure amplitude. Conversely, if the mismatch is small, the layer becomes less resonant and wide-band pulses can be transmitted. However, the HF layer will also radiate more energy backwards into the stack, causing heating issues in the probe and smaller maximum pressure amplitudes on the surface. This trade-off raises design challenges that are important to address.

The backing layer is usually a thick layer of highly absorbing medium which aims to attenuate all waves that travel backwards through the stack, so that reflections from the back of the transducer do not interfere with incident waves from tissue. The characteristic impedance of the backing layer also determines the degree of resonance in the HF and LF piezoelectric layers.

The piezoelectric layers are connected to the front-end transmit and receive electronics of the ultrasound scanner. As voltage is applied to the layers they begin to vibrate, and it is this vibration that results in the excitation and transmission of an acoustic wave. Reciprocally, when a pressure wave is incident on the piezoelectric layers, they vibrate with an intensity that is highly dependent on the frequency of the incoming wave, and thus produce a voltage over the receive electronics in the scanner. The frequency dependency of the vibration in the piezoelectric layer is related to its thickness and the acoustic impedance of the media surrounding it [54], and can be characterized by the electro-acoustic transfer function of the layer. Since it is of most interest to find the relation between the voltage over the piezoelectric material and the pressure at the surface of the transducer, the transfer function can be defined as

$$H_{tt}(\omega) = \frac{U(\omega)}{V_{tt}(\omega)} \quad (\text{A.1})$$

where $V_{tt}(\omega)$ is the voltage over the piezoelectric material, and $U(\omega)$ is the vibration velocity at the surface of the stack. The transfer function $H_{tt}(\omega)$ thus incorporates the effects of all the materials between the front face of the piezoelectric layer and the material into which the transducer is radiating.

In addition to being characterized by its electro-acoustic transfer function, the transducer has an electrical characteristic, which can be represented as an input impedance. Again, the frequency dependency of this impedance is related to the thickness of the piezoelectric layer, the acoustic impedances of the surrounding media, and characteristic parameters of the material. Since the electrodes on the piezoelectric material are parallel to one another, and situated on either side of the piezoelectric material, it should not come as a surprise that a piezoelectric layer has a mainly capacitive characteristic, with some resonant traits at frequencies where the layer has mechanical resonances. In one mathematical model for this, based on one-dimensional thickness vibration, the electrical input impedance $Z_i(\omega)$ can be written in terms of the mechanical impedance of the layer $Z_m(\omega)$, as [54, pp. 3.24]

$$Z_i(\omega) = \frac{1}{j\omega C_0} \left(1 + j \frac{h^2 C_0}{\omega Z_m(\omega)} \right) \quad (\text{A.2})$$

where

$$Z_m(\omega) = \frac{Z_0(Z_L + Z_B) \cos(\omega L/c) + j(Z_0^2 + Z_L Z_B) \sin(\omega L/c)}{2Z_0 \cos(\omega L/c) + j(Z_L + Z_B) \sin(\omega L/c) - 2Z_0} \quad (\text{A.3})$$

and the rest of the terms are listed in Tab. A.1.

Table A.1: Description of the terms used in Eq. (A.2) and (A.3).

Term	Description
ω	Angular frequency
C_0	Clamped capacitance of layer (rest capacitance)
h	Electro-acoustic coupling parameter
Z_0	Characteristic acoustical impedance of layer
Z_L	Equivalent acoustic impedance at layer front
Z_B	Equivalent acoustic impedance at layer front
L	Layer thickness
c	Speed of sound in layer

Using the above equations, and the approach in Angelsen [54, pp. 3.40], the electro-acoustical transfer function for a given transducer design can be simulated. This has been done for *Skolmen*, by Johansen [68] and Myhre [64], and the simulation results are shown in Fig. B.1 and B.2.

Note the different frequency axes, and that the LF transfer function in Fig. B.2 has two peaks in the HF pass band. This implies that if the excitation pulse on

the LF array has energy at frequency components within the pass band, the LF pressure pulse will contain HF components that effectively stretches the imaging pulse and destroys the estimation schemes presented in Sec. 3.5. *Skolmen* has a series inductor with an inductance of 220 μH mounted at the scanner-side of the cable connecting the probe to the scanner [64]. The transfer function from the output voltage of the LF pulser to the vibration velocity on the surface of the probe can be calculated, using a transmission line model for the connecting cable, and measured impedances. The transfer functions of both of the arrays are shown in Fig. A.3.

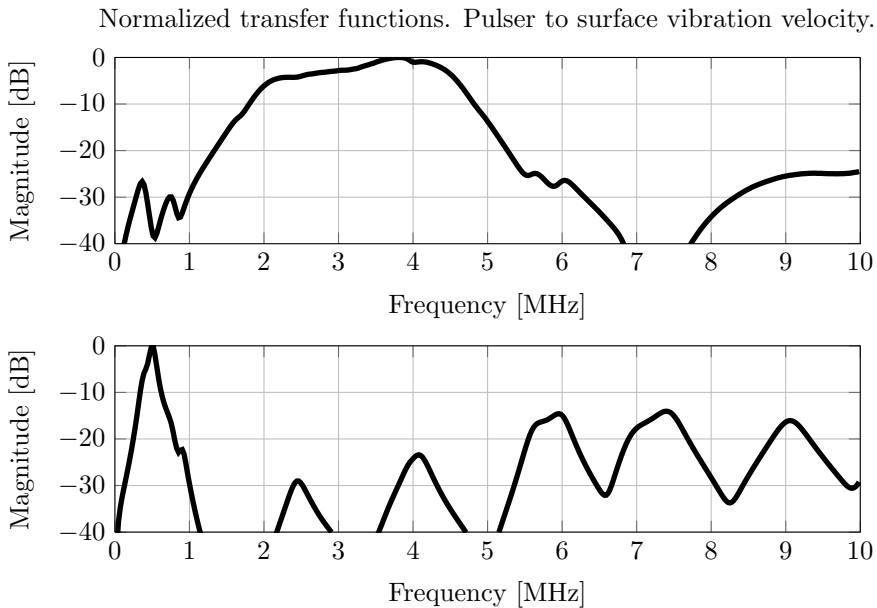


Figure A.3: Normalized transfer functions of *Skolmen* channels, from the pulser voltage to the surface vibration velocity. The HF array is above, and the LF array below. The transfer functions are estimated from measured impedances, transmission line modelled electronics and simulated electro-acoustic transfer functions.

This figure shows that the transmitted LF pressure may contain frequency components within the HF pass-band if the source signal has such components. Since the LF pulser excites the elements using rectangular pulse-trains which have harmonic components at each odd multiple of the fundamental frequency, it is therefore necessary to closely investigate the LF pulse that is generated by the system and ascertain whether it contains frequency components within the HF band.

Although thorough work has been done to design the *Skolmen* probe, the final specifications of the transducer are currently not known. SURF Technology

AS supplied a design specification to the manufacturer, but the final choice of piezoelectric and elastic materials is known only to the manufacturer. Therefore, the electro-acoustic transfer functions and input impedances must be measured in order to characterize the probe. This was partially done by Myhre [64], but the real electro-acoustic transfer function is still not known. The specification of the transducer stack is given in App. B.

A.2.2 Specifications and Acoustic

The diffraction foci of the two arrays in the *Skolmen* transducer have been calculated for the cases where the transducer is radiating into water and into tissue in Tab. B.3. The calculations were made using wavelengths at the center frequencies of the arrays, *i.e.* using $f_{c,HF} = 2.75$ MHz and $f_{c,LF} = 0.45$ MHz. These focal depths are based on the assumption that the transducer is a plane radiating source. In fact, the HF array in the transducer has an elevational lens which geometrically focuses it at 70 mm and in practice it is focused electronically in azimuth. However, the diffraction foci are still interesting since electronic and geometric focusing is only efficient if the focal point is within the near-field of the transducer. As the focal distance increases, the focal width will be increasingly dominated by the diffraction characteristics of the transducer [58]. Therefore, it is important to be aware of the position of the diffraction focus in a measurement situation.

As stated in Ch. 2, a focused wave radiated from a transducer will experience a relative phase shift of 90° as it propagates from the transducer surface to the focal point of the beam. This is also true in the diffraction focus and far-field of waves emitted by unfocused sources. It was also shown that the accumulation of non-linear propagation delay is dependent on the average LF pressure experienced by the LF pulse, and that for the delay accumulation to be linear, the average LF pressure should maintain as constant a value as possible. It was also demonstrated that the diffraction of the LF wave will cause a large shift in the relative position of the HF pulse on the LF pulse, thereby ruining the linearity of the accumulative non-linear propagation delay. These effects are important to consider when doing experimental work that utilizes the SURF technique.

A.3 Software

The software of the dual-band system comprises the standard Sonix imaging software of the SonixMDP scanner, and custom software that controls the hardware extension. It has previously not been documented how these systems interact with one another. This section will provide some details on the system as a resource for future students, documentation projects or further system development.

A.3.1 The Sonix Imaging Software

The complete documentation for the research interface of the Sonix imaging software can be found on-line and can be downloaded as a PDF file [74] from the Ultrasonix wiki page. This web page provides details on all the imaging parameters that are available in the research interface, hardware information, and information on the Software Development Kits (SDK) that Ultrasonix provides.

In subsequent sections, imaging parameters that can be found in Sonix will be referred to in the text, and can be identified by their **bold** font. The complete list and description of these parameters are given in Tab. A.2.

Table A.2: Description of important Sonix imaging parameters used in the text.

Parameter	Description
Power	Determines the output power in dB.
PRF Adjust	Increases pulsing period by the specified number of samples
TX delay	Delay in number of samples from trig to HF excitation
Extension Angle	Two times the maximum steering angle

The Sonix research interface allows the user to access a great amount of imaging parameters, relating to operations such as transmit and receive beamforming and image processing. All the parameters are probe specific, and the system thus requires specific information for each probe that is supported by the system. It expects this information to be stored in `.xml` files within subdirectories of the directory where the program executable is stored. The details of these files and how they interact with the software can be found in App. C.

A.3.2 The SURF Library

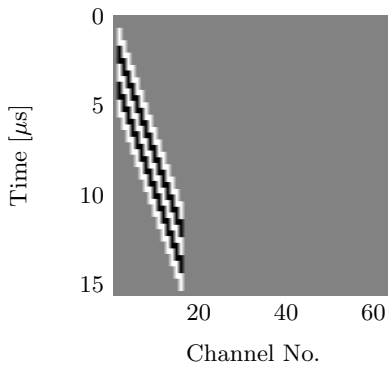
The SURF library is a series of dynamic-link libraries (DLL) written in C++, providing the Sonix software with means to control the LF pulser. The library is responsible for three major operations:

- Calculating focusing and steering delays for the LF array
- Communicating with the LF pulser hardware
- Applying SURF processing to received RF data

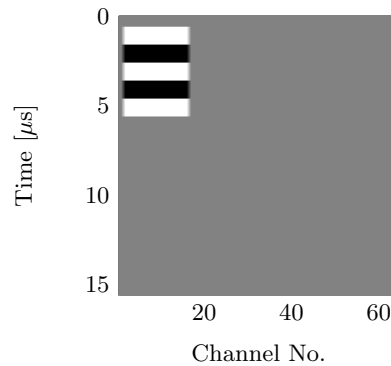
XML files are also required for this part of the software, since all parameters are probe and application specific. More details on the XML files can be found in Sec. C.2.

Parameters relating to SURF imaging can be also be adjusted in real time via Sonix. However, not all the parameters in Sonix are available to the SURF library. Parameters that are necessary in order to transmit coinciding HF and LF beams simultaneously in phased array scanning are for instance not available at present. In order for *Skolmen* to function as a phased array, this had to be circumvented by assuming that **Extension Angle** was fixed at 90 degrees, and that all beams were centred at the azimuthal midpoint of the arrays.

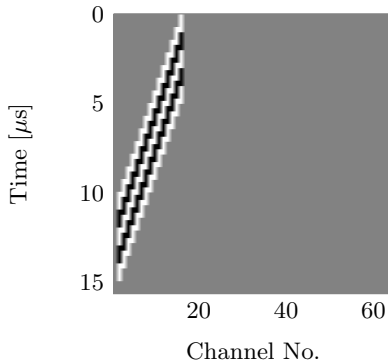
A number of other modifications were made to the source code of the SURF library in order to support the *Skolmen* probe and phased arrays in general. The most relevant changes are presented in App. E. The modifications were verified by examining the contents of the LF pulser's pulse memory. The memory is graphically presented in Fig. A.4, for three different image lines. It can clearly be seen that the pulser only uses channels 2–16, and steers the array by approximately $\pm 45^\circ$, with a steering angle of 0 degrees for the central line of the frame.



(a) Image line no. 1



(b) Image line no. 32



(c) Image line no. 64

Figure A.4: The figures show the LF pulser memory for three different imaging lines. Gray indicates zero voltage, white represents a positive voltage, and black represents a negative voltage. The total number of imaging lines in the set-up was 64, the number of half-cycles was 5, and the beam was set to be unfocused.

Skolmen Design Specification

The following sections present information about the probe that was used to collect data in this work. The transducer is a prototype made for SURF Technology A/S by the french company Vermon¹. It was designed at SURF Technology for the purpose of imaging the heart and abdominal structures with the SURF technique. It consists of two arrays, stacked in front of one another, as described in App. A.

Also in this section are simulations of the electro-acoustic transfer functions of the two arrays, simulated with *xTrans*, and measured array element impedances.

B.1 Design Specifications

The table below shows the stack specification that SURF Technology AS sent to the manufacturer of *Skolmen*.

Note in particular the specification of the centre frequency of the LF array. This frequency is related to the thickness vibration of the piezoelectric material at half wave resonance. Experience with dual-layer transducers shows that the electro-acoustic transfer function has a tendency to become double-peaked around the centre frequency, as shown in Fig. B.2.

To design the most efficient LF array, the electrical tuning circuitry should be selected so that voltage transfer from a source to an element is maximum at the same frequency where the electro-acoustic transfer function has one of its peaks. For *Skolmen*, the tuning is selected so that the maximum voltage transfer occurs at the lowest of the two peaks in the electro-acoustic transfer function of the LF array, which is located at 0.5 MHz.

¹<http://www.vermon.com>

Table B.1: Design specifications of *Skolmen*.

		LF	HF
Centre frequency	f_c	0.70 MHz \pm 10 %	2.75 MHz \pm 10 %
Minimum bandwidth, 6dB, two-way	B	0.35 MHz, 50 %	1.93 MHz, 70 %
Number of active elements, azimuth	N_a	16	64
Number of total elements, azimuth	N_T	16	96
Number of elements, elevation	N_e	1	1
Aperture size (azimuth \times elevation)	A	$24.0 \times 16.0 \text{ mm}^2$	$16.0 \times 13.0 \text{ mm}^2$
Elevation focus	F_e	∞	70 mm
Pulse length, -30 dB	t_{-20dB}	–	$< 1.45 \mu\text{s}$
Pulse length, -30 dB	t_{-30dB}	–	$< 2.4 \mu\text{s}$

B.2 Electro-acoustic Transfer Functions

In Tab. B.2, the simulation set-up for the *xTrans* simulations of *Skolmen* is shown. This is also the stack that was used in the probe specification. It is therefore in conjunction with the specification in Tab. B.1 the most accurate description one can have of the transducer apart from data from measurements.

By using the stack design in Tab. B.2, the electro-acoustic transfer functions of the LF and HF arrays were simulated. The resulting transfer functions are shown in Fig. B.1 and B.2 for the HF and LF arrays, respectively.

B.3 Electrical Characteristics

The figures in Fig. B.3 and B.4 show the estimated average impedance of the elements in the HF and LF arrays, respectively. The impedances have been estimated by measuring the input impedance on each channel in the connector, measuring the impedance of the tuning inductors, and using a transmission line model of the connecting cable. It is the same method used by Myhre [64], and the same dataset.

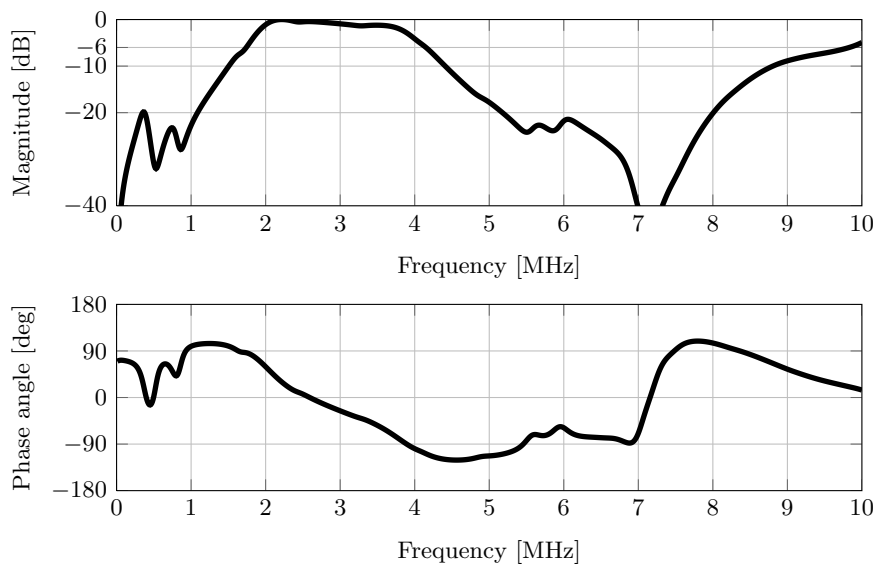


Figure B.1: Transfer function of elements of the HF array in *Skolmen*.

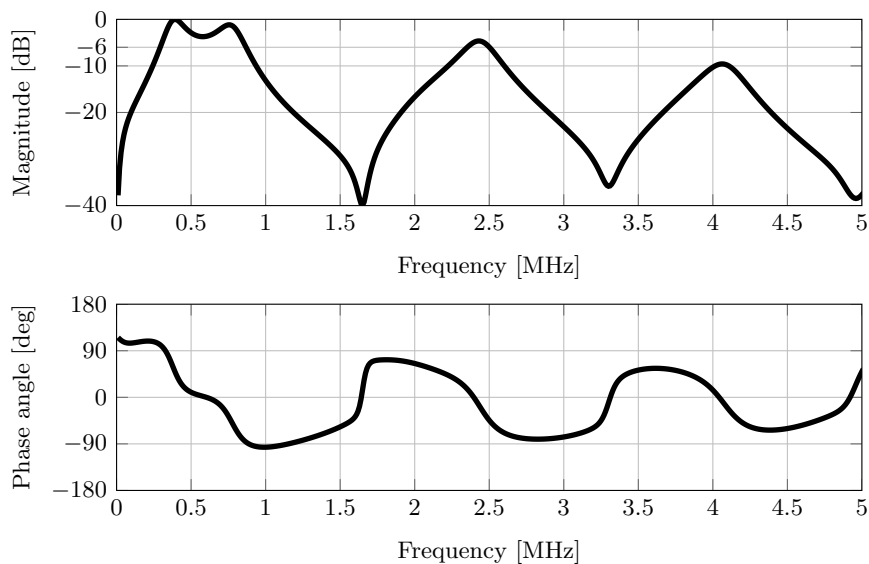


Figure B.2: Transfer function of elements of the LF array in *Skolmen*.

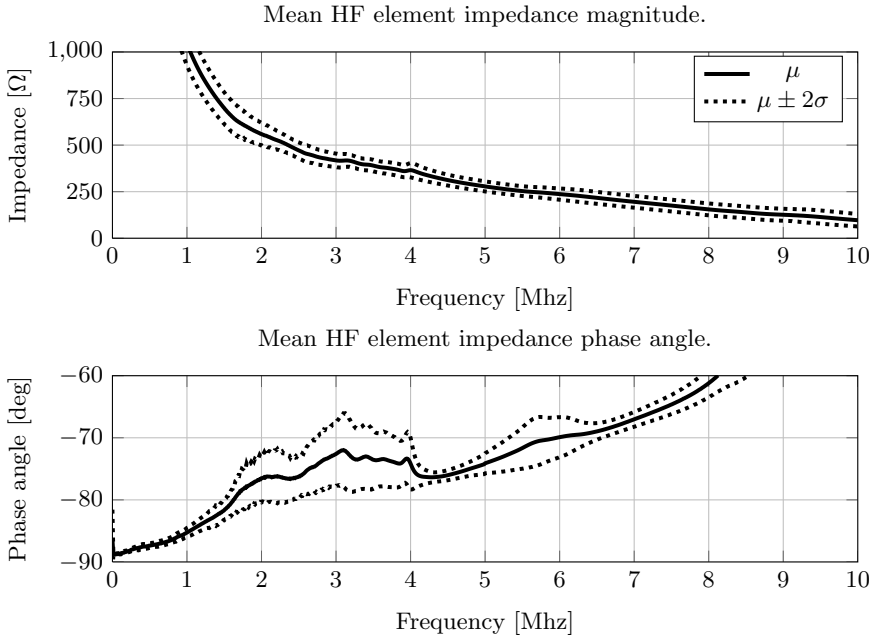


Figure B.3: Estimated mean input impedance of the HF elements in *Skolmen*

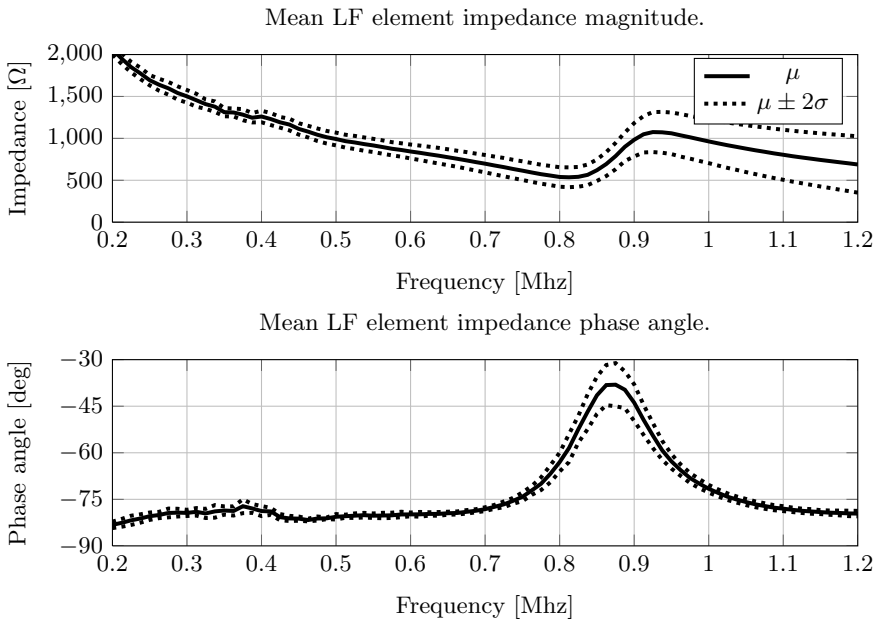


Figure B.4: Estimated mean input impedance of the LF elements in *Skolmen*

Table B.2: The proposed stack design for *Skolmen*.

Layer	h (V/m·10 ⁸)	ϵ rel. ϵ_0	Z (MRayl)	c (m/s)	Q	l (μm)
Backing			5.0	2000	10	
LF piezo	14.3	1237	19.0	3598	30	2200
Isolation			2.0	2200	30	183
HF piezo	14.3	1237	19.0	3598	30	514
Matching			6.6	2600	30	288
Matching			2.3	1800	30	158
Load			1.65	1600	30	

B.4 Diffraction Foci

The data in Tab. B.3 shows the diffraction foci of *Skolmen* in water and tissue. Note that the diffraction foci of the LF array are well within the desired maximum imaging depth of the probe. The presence of a LF diffraction focus affects the development of non-linear propagation delay, as discussed in Ch. 2. The parameters in Tab. B.3 are therefore important to bear in mind when configuring a transmission set-up for the probe.

Table B.3: *Skolmen* diffraction focusing depths

	Water [mm] ($c_0 = 1490$ m/s)	Tissue [mm] ($c_0 = 1540$ m/s)
HF azimuth	118	114
HF elevation	79	76
LF azimuth	49	47
LF elevation	22	21

XML Documentation

Much of the work that needed to be done in order for the SURF scanner to function properly with the *Skolmen* probe, was made more time consuming due to the lack of proper hardware and software documentation. A combination of lacking documentation and severely limited practical experience with the scanner slowed progress, since every error that occurred with the system could have been rooted in any part of the system. Needless to say, the amount of time spent troubleshooting on the scanner went far beyond what was expected at the beginning of the project. Therefore, the following chapter includes some basic documentation on the software peripherals, in the hope that future students or researchers that need to modify the scanner in some way may save some valuable time.

This chapter documents which XML files are needed to run the Sonix imaging software and the significance and function of each of the most important parameters in the files. Furthermore, the XML files that are needed in order to operate the scanner in SURF mode are presented, and the parameters in them will be described.

C.1 Sonix

C.1.1 Probes.xml

The file `probes.xml` contains the most basic information about all the probes that can be used with the Sonix imaging system. The file may contain definitions of up to 31 probes, each having a unique ID which must correspond with the hard-wired ID pins in the probe.

An excerpt from `probes.xml` is listed below. Note that a SURF probe may have any unoccupied ID since the LF pulser has the capability of setting the ID

to a value specified by the user. The ID must correspond to the `probe` parameter in the Sonix application files described in Sec. C.1.2, and the parameters `ID` and `probeID` in the `probes.xml` (Sec. C.2) and `probe.xml` (Sec. C.2.1) files used by the SURF library.

Listing C.1: The `probes.xml` file used by Sonix

```

1  <probe id="4" name="Skolmen">
2      <enabled>
3          <hwplatform usmoduleversion="2" state="development"/>
4          <hwplatform usmoduleversion="3" state="released"/>
5          <hwplatform usmoduleversion="4" state="released"/>
6      </enabled>
7      <type>2</type>
8      <transmitoffset>31.5</transmitoffset> <!-- 31.5 for PA -->
9      <vendors>
10         <vendor name="Vernon">
11             <model>PA4-2/16</model>
12             <partnumber cableexit="left">00.035.XXX</partnumber>
13         </vendor>
14     </vendors>
15     <icon>SA4-2_24_Prosonic.png</icon>
16     <frequency>
17         <center>2750000</center>
18         <bandwidth>2000000</bandwidth>
19     </frequency>
20     <maxfocusdistance>300000</maxfocusdistance>
21     <maxsteerangle>60000</maxsteerangle>
22     <minFocusDistanceDoppler>80000</minFocusDistanceDoppler>
23     <minlineduration>120</minlineduration>
24     <motor>
25         <FOV>0</FOV>
26         <homeMethod>0</homeMethod>
27         <minTimeBetweenPulses>0</minTimeBetweenPulses>
28         <radius>0</radius>
29         <steps>0</steps>
30         <homeCorrection>0</homeCorrection>
31     </motor>
32     <numElements>64</numElements>
33     <pinOffset>0</pinOffset>
34     <pitch>250</pitch>
35     <radius>0</radius>
36     <support>
37         <freehand3d>0</freehand3d>
38         <tempAngleSensor>0</tempAngleSensor>
39         <trus>0</trus>
40         <abus>0</abus>
41         <gps>0</gps>
42     </support>
43     <muxWrap>
44         <Rx>0</Rx>
45         <Tx>0</Tx>
46     </muxWrap>
47     <elevationLength>1.4</elevationLength>
48     <maxPwPrp>700</maxPwPrp>
49     <invertedElements>0</invertedElements>
50 </probe>

```

C.1.2 GEN-General

Every probe that is supported by Sonix must have a file named GEN-General (<probe_name>mm).xml in the ./presets/imaging directory. Basically, the file sets the values of selected variables and can also specify a range of legal values that the variables can take. Any variables that are not set in this file, are set by the parameters.default.xml file, found in ./presets.

Parameters are not named in the application files as they are in the Sonix interface. That would simply be too easy. Therefore, there is a complete list of the parameters, connecting "variable names" with "Sonix names", and offering a brief description of what each parameter does. The list is located in the file parameters.list.xml, in the directory ./presets. A variant of this list can also be found online¹.

The GEN-General file that was developed for *Skolmen* is shown below. All the measurements in Ch. 4 and App. G were made using the variable values in GEN-General (Skolmenmm).xml. alongside the specific application files in App. F.

Listing C.2: The GEN-General (Skolmenmm).xml configuration file

```

1 <?xml version="1.0" encoding="utf-8" standalone="no" ?>
2 <preset app="6" factory="1" master="1" probe="4" version="2" xmlns:xsi="http:
  //www.w3.org/2001/XMLSchema-instance" xsi:noNamespaceSchemaLocation="../
  presets.xsd">
3
4   <variables>
5     <variable id="autoBGain-brightnessCurve" value="[C] 37, 55, 46, 10"/>
6     <variable id="b image" value="General">
7       <range start="General"/>
8     </variable>
9     <variable id="b frame rate" value="FrRate Med">
10      <range start="FrRate Min"/>
11      <range start="FrRate Low"/>
12      <range start="FrRate Med"/>
13      <range start="FrRate High"/>
14      <range start="FrRate Max"/>
15    </variable>
16    <variable id="b map" value="Map 4"/>
17    <variable id="b-autoFocusAdjustLineduration" value="160"/>
18    <variable id="b-depth" value="90">
19      <range start="40" step="10" stop="150"/>
20    </variable>
21    <variable id="b-deviation" value="0">
22      <range start="-10000" step="10000" stop="10000"/>
23    </variable>
24    <variable id="b-dyn linear factor" value="25"/>

```

¹<http://www.ultrasonix.com/wikisonix/docs/html/Menu.htm> (20.07.2013)

```

25 <variable id="b-dyn pivot out" value="212"/>
26 <variable id="b-extension angle" value="90000">
27   <range start="90000"/>
28 </variable>
29 <variable id="b-focus blend" value="8"/>
30 <variable id="b-focus count" value="1">
31   <range start="0" step="1" stop="10"/>
32 </variable>
33 <variable id="b-gain" value="300"/>
34 <variable id="b-image rect" value="[R] 0, 456, 0, 127"/>
35 <variable id="b-initial zoom" value="100"/>
36 <variable id="b-persistence" value="2"/>
37 <variable id="b-reject" value="24"/>
38 <variable id="b-rx curve depth" value="70000"/>
39 <variable id="b-rx f number" value="7"/>
40 <variable id="b-sampl freq" value="10000000"/>
41 <variable id="b-tgc-depth" value="150000"/>
42 <variable id="b-tgc-sensitivity" value="35"/>
43 <variable id="b-tx aperture max" value="32"/>
44 <variable id="b-weight type" value="0"/>
45 <variable id="bb-initial zoom" value="100"/>
46 <variable id="bflow-map" value="5"/>
47 <variable id="b-ldensity" value="128">
48   <range start="64"/>
49   <range start="96"/>
50   <range start="128"/>
51   <range start="192"/>
52   <range start="256"/>
53 </variable>
54 <variable id="focus boundaries" value="48,92,168,288"/>
55 <variable id="focus depth" value="70000">
56   <range start="40000" step="10000" stop="150000"/>
57 </variable>
58 <variable id="focus span" value="6000"/>
59 <variable id="focus span default in non pulse inv har" value="1000"/>
60 <variable id="max fr" value="300">
61   <range start="0" step="10" stop="600"/>
62 </variable>
63 <variable id="mode id" value="B">
64   <range start="B"/>
65   <range start="M"/>
66   <range start="Color Doppler"/>
67   <range start="Pulsed Wave Doppler"/>
68   <range start="Triplex"/>
69   <range start="Panoramic"/>
70   <range start="Dual B"/>
71   <range start="Quad B"/>
72   <range start="Compound"/>
73   <range start="Dual Color"/>
74   <range start="Dual Compound"/>
75   <range start="Color Split"/>
76   <range start="4D"/>
77   <range start="Color M"/>
78   <range start="Elastography"/>
79   <range start="Anatomical M"/>
80   <range start="Elastography Comparative"/>
81   <range start="Fusion"/>

```

```

82     <range start="Vector Doppler"/>
83     <range start="SURF"/>
84 </variable>
85 <variable id="mru filtering" value="Clarity High"/>
86 <variable id="power" value="7">
87     <range start="0" step="1" stop="15"/>
88 </variable>
89 <variable id="prf-adjust" value="0">
90     <range start="0" step="1000" stop="10000"/>
91 </variable>
92 <variable id="surf tx-voltage lf" value="0">
93     <range start="0" step="5" stop="100"/>
94 </variable>
95 <variable id="tx aperture curve" value="[C] 0, 50, 100, 50"/>
96 <variable id="tx curve depth" value="70000"/>
97 </variables>
98
99 <optimizations>
100 <optimization id="b frame rate" value="FrRate High">
101     <variable id="b-ldensity" value="96">
102         <range start="96"/>
103     </variable>
104 </optimization>
105 <optimization id="b frame rate" value="FrRate Max">
106     <variable id="b-ldensity" value="64">
107         <range start="64"/>
108     </variable>
109 </optimization>
110 <optimization id="b frame rate" value="FrRate Med">
111     <variable id="b-ldensity" value="128">
112         <range start="128"/>
113     </variable>
114 </optimization>
115 <optimization id="b frame rate" value="FrRate Low">
116     <variable id="b-ldensity" value="192">
117         <range start="192"/>
118     </variable>
119 </optimization>
120 <optimization id="b frame rate" value="FrRate Min">
121     <variable id="b-ldensity" value="256">
122         <range start="256"/>
123     </variable>
124 </optimization>
125 <optimization id="b image" value="General">
126     <variable id="b-autoFocusPos1" value="3000"/>
127     <variable id="b-autoFocusPos2" value="6000"/>
128     <variable id="b-autoFocusPos3" value="11000"/>
129     <variable id="b-autoFocusPos4" value="20000"/>
130     <variable id="b-autoFocusPos5" value="30000"/>
131     <variable id="b-autoFocusPos6" value="40000"/>
132     <variable id="b-autoFocusPos7" value="28000"/>
133     <variable id="b-freq" value="2800000">
134         <range start="1000000" step="100000" stop="4000000"/>
135     </variable>
136     <variable id="b-freq display" value="2800000"/>
137     <variable id="b-iq-bottom freq" value="1800000"/>
138     <variable id="b-iq-top freq" value="4000000"/>

```

```

139     <variable id="b-pulse index a" value="0"/>
140     <variable id="b-tgc" value="[C] 0, 50, 100, 50"/>
141     <variable id="bx-autoFocusPos1" value="5000"/>
142     <variable id="bx-autoFocusPos2" value="15000"/>
143     <variable id="bx-autoFocusPos3" value="9800"/>
144     <variable id="max fr" value="0"/>
145 </optimization>
146 <optimization id="hw-platform" value="V2">
147     <variable id="b-dyn log factor offset" value="-8"/>
148     <variable id="b-gain-digimin" value="-8"/>
149     <variable id="b-gain-digirange" value="26"/>
150     <variable id="b-reject offset" value="4"/>
151     <variable id="bxiq-x new reject" value="44"/>
152     <variable id="color-numDummyLines" value="6"/>
153     <variable id="color-r0 clutter max" value="800"/>
154     <variable id="color-r0 clutter max power" value="860"/>
155     <variable id="doppler-digital gain min" value="-31"/>
156     <variable id="doppler-digital gain range" value="16"/>
157     <variable id="pw-reject" value="40"/>
158     <variable id="pw-voltage [-] rng1" value="7"/>
159     <variable id="pw-voltage [-] rng2" value="8"/>
160     <variable id="pw-voltage [-] rng3" value="9"/>
161     <variable id="pwDuplex-gain offset" value="25"/>
162     <variable id="tri-gain offset" value="25"/>
163     <variable id="vca-amp" value="5"/>
164 </optimization>
165 <optimization id="hw-platform" value="V3">
166     <variable id="b-dyn log factor offset" value="-8"/>
167     <variable id="b-gain-digimin" value="-8"/>
168     <variable id="b-gain-digirange" value="26"/>
169     <variable id="b-reject offset" value="4"/>
170     <variable id="b-tx aperture max" value="32"/>
171     <variable id="bxiq-x new reject" value="44"/>
172     <variable id="color-numDummyLines" value="6"/>
173     <variable id="color-r0 clutter max" value="800"/>
174     <variable id="color-r0 clutter max power" value="860"/>
175     <variable id="doppler-digital gain min" value="-31"/>
176     <variable id="doppler-digital gain range" value="16"/>
177     <variable id="pw-reject" value="40"/>
178     <variable id="pw-voltage [-] rng1" value="5"/>
179     <variable id="pw-voltage [-] rng2" value="5"/>
180     <variable id="pw-voltage [-] rng3" value="6"/>
181     <variable id="pwDuplex-gain offset" value="25"/>
182     <variable id="tri-gain offset" value="25"/>
183     <variable id="vca-amp" value="20"/>
184 </optimization>
185 <optimization id="hw-platform" value="V4">
186     <variable id="b-gain-digimin" value="-15"/>
187     <variable id="b-gain-digirange" value="40"/>
188     <variable id="b-tx aperture max" value="32"/>
189     <variable id="bxiq-x new reject" value="50"/>
190     <variable id="color-numDummyLines" value="9"/>
191     <variable id="color-r0 clutter max" value="800"/>
192     <variable id="color-r0 clutter max power" value="860"/>
193     <variable id="doppler-digital gain min" value="-15"/>
194     <variable id="doppler-digital gain range" value="10"/>
195     <variable id="pw-reject" value="40"/>

```

```

196     <variable id="pw-voltage [-] rng1" value="2"/>
197     <variable id="pw-voltage [-] rng2" value="3"/>
198     <variable id="pw-voltage [-] rng3" value="4"/>
199     <variable id="pwDuplex-gain offset" value="25"/>
200     <variable id="tri-gain offset" value="25"/>
201     <variable id="vca-amp" value="10"/>
202   </optimization>
203 </optimizations>
204
205 </preset>

```

C.2 SURF

When adding SURF support for additional probes in Sonix, XML files specifying the characteristics of the new probes must be added. The SURF code uses a probe catalogue file, `probes.xml`, to specify which probes that are currently supported. The file that is currently used is shown in this section.

Listing C.3: The `probes.xml` file used by the SURF library

```

1 <probes>
2   <probe name="Vora" ID="18" probedir="Vora"/>
3   <probe name="Okla" ID="23" probedir="okla"/>
4   <probe name="Viglen" ID="29" probedir="viglen"/>
5   <probe name="Ruten" ID="30" probedir="ruten"/>
6   <probe name="L14-5/38" ID="2" probedir="L14"/>
7   <probe name="Skolmen" ID="4" probedir="Skolmen"/>
8 </probes>

```

Each entry in the `probes.xml` file has the following attributes

name Specifies the name of the probe.

ID Specifies the probe ID, and must correspond to the ID in the Sonix version of `probes.xml`.

probedir Specifies the directory in which the XML files containing probe information are located.

The following files should be located in the directory specified by `probedir` in the `probes.xml` file.

C.2.1 Probe.xml

The `probe.xml` file that is used by the SURF library sets the parameters relating to the physical layout of the probe. It also specifies the default operating mode

for the probe when SURF mode is activated on the SonixMDP. Note that this mode is the default SURF application, not the default imaging preset used by Sonix.

The `probe.xml` file for *Skolmen* is listed below, with comments.

Listing C.4: The `probe.xml` file for *Skolmen*

```

1  <?xml version="1.0" encoding="UTF-8"?>
2  <probe probeID="4" defapp="bmode.xml" NumHFPerLF="6">
3    <name>Skolmen</name>
4    <footprints>
5      <footprint name="HFLF" type="LA" dll="footprint_LA.dll">
6        <azimuthsize>
7          <value>24000</value>
8          <unit>um</unit>
9        </azimuthsize>
10       <elevationsize>
11         <value>16000</value>
12         <unit>um</unit>
13       </elevationsize>
14     </footprint>
15   </footprints>
16   <subarrays>
17     <subarray>
18       <name>HF</name>
19       <footprint name="HFLF"/>
20       <geometry type="PA" dim="1D">
21         <azim>
22           <count>64</count>
23           <pitch>250</pitch>
24           <kerf>0</kerf>
25           <outerpos>
26             <az>4125</az>
27             <el>0</el>
28           </outerpos>
29         </azim>
30         <elementindx>
31           <row indx="0">1:64</row>
32         </elementindx>
33       </geometry>
34       <acoustics>
35         <!-- time needed for a pulse from excitation to emittance on
36            transducer surface -->
37         <timetofront>
38           <value></value>
39           <unit></unit>
40         </timetofront>
41       </acoustics>
42     </subarray>
43     <subarray>
44       <name>LF</name>
45       <footprint name="HFLF"/>
46       <mask>1</mask>
47       <geometry type="PA" dim="1p25D">
48         <azim>
49           <count>16</count>

```

```

49     <pitch>1500</pitch>
50     <kerf>0</kerf>
51     <outerpos>
52         <az>750</az>
53         <el>0</el>
54     </outerpos>
55     <baffle>3</baffle>
56 </azim>
57
58 <elev>
59     <count>1</count>
60     <pitch>8000</pitch>
61     <kerf>100</kerf>
62     <outerpos>
63         <az>474</az>
64         <el>3300</el>
65     </outerpos>
66 </elev>
67
68 <elementindx>
69     <row indx="0">2:2:128</row>
70     <row indx="1">1:2:127</row>
71 </elementindx>
72 </geometry>
73 <acoustics>
74     <!-- time needed for a pulse from excitation to emittance on
75         transducer surface -->
76     <timetofront>
77         <value></value>
78         <unit></unit>
79     </timetofront>
80 </acoustics>
81 </subarray>
82 </subarrays>
83 <limits>
84     <limit type="Voltages" value="-100 100"/>
85 </limits>
</probe>

```

C.2.2 Applications.xml

The `applications` file for *Skolmen* is listed below. Each application must have an ID, a name and an `appfile` parameter, specifying which XML file that is associated with the application. The `applications` file and the files specified by the `appfile` parameters in it are expected to be in the same folder as the `probe.xml` file, *i.e.* in `SURF/probes/<probedir>/`.

Listing C.5: The `applications.xml` file for *Skolmen*

```

1 <!-- ID corresponds to "SURF Application" parameter in Sonix -->
2
3 <applications>
4   <application ID="0" name="General" appfile="bmode.xml" />

```

```

5 <application ID="1" name="B-Plus" appfile="bmode_plus.xml" />
6 <application ID="2" name="CEUS" appfile="ceus_2pulse.xml" />
7 <application ID="3" name="RevSup" appfile="rev_sup.xml"/>
8 </applications>

```

C.2.3 Application files

The application files that are used by the SURF library specify the transmit set-up of the LF array and the processing that is done on received data. All the application set-ups are accessible from Sonix via the parameter SURF Application, which sets the current application via its corresponding ID tag. An example of an application file for *Skolmen* is shown below, and commented.

Listing C.6: The ceus_2pulse.xml file for *Skolmen*

```

1 <?xml version="1.0" encoding="utf-8"?>
2 <application preset="Generic-SURF CEUS (Vora)" name="SURF CEUS, 2 pulse">
3   <!-- Set any SURF parameters, see parameters.list.xml for alternatives and
4     syntax -->
5   <parameters>
6     <parameter name="Probe stack delay" id="3018" >
7       <default>
8         <x>0 100000</x>
9         <y>-276 -276</y>
10      </default>
11    </parameter>
12  </parameters>
13
14  <!-- Set up transmit configuration -->
15  <!--TX config node: Frontends with Pulses,BeamConfigs and Subarrays-->
16  <txconfig>
17
18    <!-- Set up configuration for multiple front ends -->
19    <frontends>
20
21      <!-- Define the LF front end -->
22      <frontend id="LF" type="LF" disabled="no">
23        <setup>
24          <!-- Sampling frequency of the LF pulser is 80 MHz -->
25          <samplingfrequency value="80000000"/>
26        </setup>
27
28      <!-- Set up transmit pulses, set all pulseforms within this node -->
29      <pulses>
30        <!-- Give each pulse a unique ID -->
31        <pulse id="POS">
32          <!-- Pulse form can be "square", "sine", or "zero" -->
33          <form>square</form>
34          <!-- frequency and numhalfcycles take parameters from Sonix. -->
35          <frequency paramID="1322"/>
36          <numhalfcycles paramID="1325"/>
37          <!-- Specify polarity of first half cycle in the excitation pulse
38          -->

```

```

37     <startpositive value="yes"/>
38 </pulse>
39
40 <pulse id="NEG">
41   <form>square</form>
42   <frequency paramID="1322"/>
43   <numhalfcycles paramID="1325"/>
44   <startpositive value="no"/>
45 </pulse>
46 </pulses>
47
48 <!-- Configures the LF beams. Totally reliant on what the HF is doing,
49    so all parameters should be linked to parameters in Sonix. Multiple
50    beams may be defined with unique IDs, but the parameters within each
51    configuration should be the same.-->
52 <beamconfigs>
53   <!-- The only supported beam configuration is specified by
54    beamconfig_1p25D.dll -->
55   <beamconfig type="Beam1p25D" dll="beamconfig_1p25D.dll" id="CEUS">
56     <focusing>
57       <numfoci paramID="157"/>
58       <depth paramID="1254"/>
59       <span paramID="1255"/>
60     </focusing>
61     <aperture>
62       <curve paramID="128"/>
63       <depth paramID="392"/>
64       <max paramID="162"/>
65     </aperture>
66     <triggoffset paramID=""/>
67     <probesetup>
68       <rows active="10"/>
69     </probesetup>
70   </beamconfig>
71 </beamconfigs>
72
73 <!-- Create a list of transmit beam forms -->
74 <txbeamforms>
75   <!-- Each transmit beam form has an ID, a beam configuration, and
76    may be assigned a series of pulses -->
77   <txbeamform id="1" beamID="CEUS">
78     <pulse indx="0" pulseID="POS"/>
79     <pulse indx="1" pulseID="NEG"/>
80   </txbeamform>
81 </txbeamforms>
82
83 <!-- Multiple subarrays may be defined. -->
84 <subarrays>
85   <subarray name="LF">
86     <!-- Set beamformer. Currently, the only beamformer available is
87    Beamformer_1p25D.dll. However, this beamformer supports LA, CLA,
88    and PA with a sector opening angle of 90 degrees -->
89     <beamforming type="Beamforming1p25D" dll="Beamformer_1p25D.dll">
90       <!-- Set transmit delay in number of LF periods -->
91       <lfperiodoffset>1.0</lfperiodoffset>
92     </beamforming>
93     <!-- Additional beamforming paramteres may be added as desired,
94    as long as the LoadFromXML function in the Beamformer_1p25D.cpp

```

```

      file is expanded accordingly -->
86 </beamforming>
87
88 <!-- Set up frame configuration. A single frame contains a number
      of scan lines specified by linedensity. However, beams may be fired
      along each scan line multiple times, equal to the product of the
      number of txbeamforms, the number of pulses within each txbeamform
      and the number of foci in each txbeamform. -->
89 <frames>
90 <!-- Each frame must have a name a type and an ID -->
91 <frame name="B-mode frame" type="B-Mode" id="A">
92 <!--Set up the transmit pattern for the beam, defined by a
      number of scline nodes -->
93 <txpattern>
94 <!-- TXBID - ID of a txbeamform -->
95 <!-- line - Name of the scline -->
96 <!-- indx - Index of the scline -->
97 <scline TXBID="1" line="1" indx="1"/>
98 </txpattern>
99 <!-- Fetch the line density that is used by Sonix. -->
100 <linedensity paramID="32"/>
101 </frame>
102 </frames>
103 <!-- Set the sequence in which frames are acquired, e.g. A B C. -->
104 <frameseq>A</frameseq>
105 </subarray>
106 </subarrays>
107 <!-- Set the sequence in which subarrays are used, e.g. LF1 LF2 -->
108 <subarraysequence>LF</subarraysequence>
109 </frontend>
110 </frontends>
111 </txconfig>
112
113 <!-- Set up receive configuration -->
114 <rxconfig>
115 </rxconfig>
116
117 <!-- Select processing -->
118 <processing>
119 <iqprocessing dll="CEUSProcessor.dll"/>
120 </processing>
121 </application>

```

Imaging Parameters

The number of parameters that are available for adjustment when using the research mode of the Sonix software is staggering. Without any knowledge of how the system ties all of these parameters together, it can be a struggle to understand which parameter it is that is causing a particular problem encountered during lab work. In order to narrow down the list of possible culprits for future students and researchers, the complete list of parameters affecting the SURF mode in the scanner is listed in Tab. D.1 through D.3. The SURF library uses SURF specific parameters to define LF transmit beams (Tab. D.1), and to adjust SURF processing (Tab. D.2). Additionally, it relies on some parameters from the Sonix software. Sonix parameters that are currently available are shown in Tab. D.3.

The list in Tab. D.3 does not include some parameters that are vital for using phased arrays in SURF mode. In order to fully adapt the LF beam-forming according to the HF beam-forming, one would need access to the parameters **Extension Angle** and **LD Adjust** from the B-GEOM menu in Sonix. **Extension Angle** specifies the opening angle of the frame when the **Sector** is set 100%, and **LD Adjust** specifies how many extra scan lines should be used in the frame. The total number of scan lines is thus

$$\text{Scanlines} = \langle \text{Line Density} \rangle + \langle \text{LD Adjust} \rangle, \quad (\text{D.1})$$

and the scan line angles are calculated as

$$\text{th}_n = \frac{\text{th}_E}{2} \left(\frac{2n}{\langle \text{Line Density} \rangle + \langle \text{LD Adjust} \rangle} - 1 \right) + \langle \text{Steer} \rangle \quad (\text{D.2})$$

where

$$\text{th}_E = \langle \text{Extension Angle} \rangle \times \langle \text{Sector} \rangle \quad (\text{D.3})$$

The modifications made to the source code of the SURF library assume that these parameters take the values $\langle \text{Extension Angle} \rangle = 90^\circ$ and $\langle \text{LD Adjust} \rangle = 0$, respectively.

Table D.1: SURF mode transmission parameters.

Type	Name	Description
int	<code>txFrequencyLF</code>	The transmit frequency of the LF array.
int	<code>txPressureLF</code>	Transmit pressure. Not implemented.
int	<code>txVoltageLF</code>	Pulser voltage.
int	<code>txNumHalfCyclesLF</code>	Number of half cycles in the LF pulse.
int	<code>txFlipLF</code>	Flip the polarity of the LF pulse.
int	<code>enableIndepFocusLF</code>	Focus the LF beam independently of the HF beam.
int	<code>txDefocusLF</code>	Set the LF array to transmit a plane wave.
int	<code>focusDepthLF</code>	Depth of the independent LF focus.
int	<code>focusSpanLF</code>	Distance between LF foci when multiple foci are used.
int	<code>relAptSizeLF</code>	Size of the LF aperture, relative to the HF aperture.
int	<code>relAptSizeCurveSpanLF</code>	The distance between different LF foci. Used with the <code>txAptCurve</code> .
SC*	<code>txAptCurve</code>	Curve defining the size of the transmit aperture as a function of focal depth.
int	<code>txAptMaxLF</code>	Maximum LF aperture size.
int	<code>txAptDepthLF</code>	The largest depth for which the transmit aperture curve is valid. For focal depths beyond this, the aperture size is equal to <code>txAptMaxLF</code> .
int	<code>centerActiveLF</code>	Activate the central row of elements in the LF array.
int	<code>outerActiveLF</code>	Activate the outer rows of elements in the LF array. With the new probe interface, this parameter doubles the amount of current flowing into the central row.
int	<code>positionHF</code>	The relative position of the HF relative to the LF, in percent of the LF period.
int	<code>zeroAdjustDelay</code>	Adjust the transmit delay of the LF pulse.
SC	<code>zeroAdjustDelayCurve</code>	Curve for adjusting the transmit delay of the LF pulse as a function of depth, when using multiple foci.
int	<code>zeroAdjustDelaySpan</code>	The distance between different LF foci. Used with the <code>zeroAdjustDelayCurve</code> .
int	<code>rfMModeOnOff</code>	Turn on M-mode.
int	<code>rfMModePos</code>	Select image line to perform M-mode on.
int	<code>rectLeft</code>	Select first scan line number.
int	<code>rectRight</code>	Select final scan line number.

* Abbreviated SURF_CURVE

Table D.2: SURF mode processing parameters.

Type	Name	Description
int	<code>IQDecimation</code>	Decimation ratio applied to IQ data.
int	<code>envDecimation</code>	Decimation ratio applied to the envelope data.
int	<code>outputBits</code>	Sample bit resolution. 0 = 8 bits, 1 = 16 bits.
int	<code>IQDemodFreqA</code>	Demodulation frequency used in the IQ demodulation.
int	<code>IQDemodFreqB</code>	Demodulation frequency used in the IQ demodulation. Not in use.
int	<code>IQDemodLPFilterLength</code>	Length of the low pass filter used in the SURF IQ demodulation.
int	<code>IQDemodLPFilterCutoff</code>	Cut-off frequency of the low pass filter used in the SURF IQ demodulation.
int	<code>SURFProcessingType</code>	Select SURF processing. Processing type depends on the definition in the application file that is used.
int	<code>SURFModeID</code>	Application selection. Application depends on definition in the <code>probe.xml</code> file.
int	<code>SURFModeOn</code>	SURF mode on/off.
int	<code>medianFilterSize</code>	Length of median filter used to smooth delay estimation.
int	<code>windowLength</code>	Length of the regression window used in delay estimation
int	<code>interpolationType</code>	Interpolation type used for delay correction. 1 = Linear, 0 = Cubic Spline
int	<code>flash</code>	Transmit LF flash sequence to destroy USCA. Not implemented.
int	<code>mip</code>	Maximum projection image processing.
int	<code>delayGain</code>	Gain applied on delay estimates.
int	<code>lateralUpsample</code>	Lateral up-sampling of IQ data before envelope detection in order to give better speckle. Sonix does not handle this correctly.

* Abbreviated SURF_CURVE

Table D.3: SURF parameters supplied by Sonix.

Type	Name	Description
int	<code>txFrequencyHF</code>	The transmit frequency of the HF array.
int	<code>focusDepthHF</code>	The focal depth of the HF array.
int	<code>txApertureMaxHF</code>	The maximum number of elements used in beam-forming by the HF array.
int	<code>txApertureDepthHF</code>	The largest depth for which the transmit aperture curve is valid. For focal depths beyond this, the aperture size is equal to <code>txApertureMaxHF</code> .
SC*	<code>txAptCurveHF</code>	A curve specifying the number of elements that are to be used in transmission when focusing at a certain depth.
int	<code>numFoci</code>	The number of HF transmit foci.
int	<code>focusSpan</code>	The spacing between adjacent foci.
int	<code>speedOfSound</code>	Specifies the assumed average speed of sound. Used in beam-forming.
int	<code>txDelayHF</code>	Additional delay added from the pulse trigger to the excitation of the HF pulse.
int	<code>txDefocusHF</code>	Boolean specifying whether or not the HF beam is a plane wave (true), or focused (false).
int	<code>steer</code>	Specifies the static steering angle of the array.
int	<code>rfDecimation</code>	Check <code>parameters.list.xml</code> Decimation factor applied by Sonix before passing RF data to SURF processing.
int	<code>imagingDepth</code>	Maximum imaging depth.
int	<code>lineDensity</code>	Specifies the number of lines used in each frame.
int	<code>probeID</code>	The ID of the probe.
int	<code>inputSamples</code>	Length of the RF data passed from Sonix' image buffer.
int	<code>inputLines</code>	Width of the RF data passed from Sonix' image buffer.
int	<code>accumulator</code>	Specifies how many packets are in each frame. One packet consists of all pulses fired along a single line with varying beam configurations.
int	<code>accumulatorSend</code>	Not clear what this parameter does, but it doesn't appear to be used in SURF.
int	<code>enable</code>	This is a SURF parameter.
int	<code>gainB</code>	B-mode image gain. Used by the SURF IC processor.
int	<code>dynamicRange1</code>	Dynamic range used by the SURF IC processor.
int	<code>dynamicRange2</code>	Top of dynamic range.
int	<code>newReject</code>	Not used by the SURF library.
int	<code>outputPivot</code>	Not used by the SURF library.
int	<code>persistence</code>	The number of frames to apply frame averaging on the B display. Used by the SURF IC Processor.

* Abbreviated SURF_CURVE

Software Adjustments

A few software adjustments to the SURF library needed to be made, in order for the system to be compatible with steering the *Skolmen* probe as a phased array. The following chapter documents the changes that were made.

Each modified file is quite long, so rather than listing the entire file, only the modified parts of the code are shown here. The old source code is listed alongside the modified code.

E.1 Geometrybase

The header and source files `geometrybase.h` and `geometrybase.cpp` were modified so that the system could recognise a phased array geometry. The value of the `GeometryType` enum in these files defines which beam-forming that is done by the LF beam-former.

Listing E.1: Original geometrybase.h file

```
7 typedef enum
8 {
9     GeometryT_LA_1p00d, // linear array (rectangular surface) 1D
10    GeometryT_LA_1p25d, // linear array (rectangular surface) 1.25D
11    Geometry_LA,
12    Geometry_CLA,
13 } GeometryType;
```

Listing E.2: Original geometrybase.cpp file

```
56 if(iStr == "LA")
57 {
58     mType = Geometry_LA;
59 }
60 else if(iStr == "CLA")
61 {
62     mType = Geometry_CLA;
63 }
64 else
65 {
66     LOG_ERROR("Invalid geometry type: " + iStr);
67     return false;
68 }
```

Listing E.3: Modified geometrybase.h file

```
7 typedef enum
8 {
9     GeometryT_LA_1p00d, // linear array (rectangular surface) 1D
10    GeometryT_LA_1p25d, // linear array (rectangular surface) 1.25D
11    Geometry_LA,
12    Geometry_CLA,
13    Geometry_PA
14 } GeometryType;
```

Listing E.4: Modified geometrybase.cpp file

```
56 if(iStr == "LA")
57 {
58     mType = Geometry_LA;
59 }
60 else if(iStr == "CLA")
61 {
62     mType = Geometry_CLA;
63 }
64 else if(iStr == "PA")
65 {
66     mType = Geometry_PA;
67 }
68 else
69 {
70     LOG_ERROR("Invalid geometry type: " + iStr);
71     return false;
72 }
```

E.2 Beamformer

The beam-former that was implemented in the SURF library lacked the ability to steer successive transmit beams in different directions. As mentioned in App. D, the software needs more parameters from the Sonix software in order to do this properly. The `beamformer_1p25d.cpp` file was modified to support phased array steering, by assuming that the steering angles of the beams could be calculated according to Eq. (D.2), that the opening angle of the frame was 90 degrees, and that the number of additional lines specified by the LD `Adjust` parameter was 0.

The function selects the manner of beam-forming by checking which geometry that is given to the software so the modifications that were presented in Sec. E.1 are used directly.

In addition to modifying the main B-mode beam-forming function, an error was found and corrected in the function that calculates the actual delays that are used by the LF pulser. The modification can be seen in line 186 in the listings below.

Listing E.5: Original beamformer_1p25d.cpp file (Part 1)

```
106 // Set the delay function
107 switch(iGeometryLF.GetType())
108 {
109 case Geometry_LA:
110     mDelayFunction = Helpers::ComputeFocusDelayLA;
111     break;
112 case Geometry_CLA:
113     mDelayFunction = Helpers::ComputeFocusDelayCLA;
114     break;
115 default:
116     LOG_ERROR("Not a valid geometry for 1D beamforming");
117     return false;
118 }
```

Listing E.6: Modified beamformer_1p25d.cpp file (Part 1)

```
106 // For Skolmen hack
107 float thBeg, thEnd;
108
109 // Set the delay function
110 switch(iGeometryLF.GetType())
111 {
112 case Geometry_LA:
113     mDelayFunction = Helpers::ComputeFocusDelayLA;
114
115     // For Skolmen hack
116     thBeg = 0;
117     thEnd = 0;
118     break;
119 case Geometry_CLA:
120     mDelayFunction = Helpers::ComputeFocusDelayCLA;
121
122     // For Skolmen hack
123     thBeg = 0;
124     thEnd = 0;
125     break;
126 case Geometry_PA:
127     mDelayFunction = Helpers::ComputeFocusDelayLA;
128
129     // For Skolmen hack
130     thEnd = -45*IPP_PI/180.0f;
131     thBeg = 45*IPP_PI/180.0f;
132     break;
133 default:
134     LOG_ERROR("Not a valid geometry for 1D beamforming");
135     return false;
136 }
```

Listing E.7: Original beamformer_1p25d.cpp file (Part 2)

```

180     // Compute center HF element
181     iCenterHF_el = iScanLine*iElementIncrementHF;
182     iVirtualCenterLF_el = iCenterHF_el/iNumHFE1PerLF;
183     iCenterLF_el = (int)ceil(iVirtualCenterLF_el);
184     iVirtualCenterLF_el += 1.0f - iCenterZeroJustify;
185
186     // Add two elements for the baffle
187     iCenterLF_el += iGeometryLF.GetActiveBaffle();
188     iVirtualCenterLF_el += iGeometryLF.GetActiveBaffle();

```

Listing E.8: Modified beamformer_1p25d.cpp file (Part 2)

```

192     float dTheta = (thEnd - thBeg)/((float)(iEndScanLine -
193         iStartScanLine - 1));
194     float thSteer;
195
196     //Step one pattern width at the time over the frame
197     for(int iScanLine = iStartScanLine ;
198         iScanLine <= iEndScanLine ;
199         iScanLine++)
200     {
201         // for each beam(line) in the pattern
202
203         thSteer = dTheta*((float)(iScanLine-1)) + thBeg;
204
205         for(int n=0;n<iLines.size();n++)
206         {
207             // Compute center HF element
208             if (iGeometryLF.GetType() == Geometry_PA)
209             {
210                 // PA beam is always centered at the centre of the array
211                 iCenterHF_el = (iNumElementsAzimHF - 1.0f)/2.0f;
212                 iCenterLF_el = (int)((iNumElementsAzimLF)/2.0f);
213                 iVirtualCenterLF_el = iNumElementsAzimLF/2.0f;
214             }
215             else
216             {
217                 iCenterHF_el = iScanLine*iElementIncrementHF;
218                 iVirtualCenterLF_el = iCenterHF_el/iNumHFE1PerLF;
219                 iCenterLF_el = (int)ceil(iVirtualCenterLF_el);
220                 iVirtualCenterLF_el += 1.0f - iCenterZeroJustify;
221
222                 // Add two elements for the baffle
223                 iCenterLF_el += iGeometryLF.GetActiveBaffle();
224                 iVirtualCenterLF_el += iGeometryLF.GetActiveBaffle();
225             }
226         }
227     }

```

Listing E.9: Original beamformer_1p25d.cpp file (Part 3)

```

222     ComputeFocusDelays(iLoLF_el, iHiLF_el, iCenterLF_el,
                       iAzimPitchLF_um, iFocusDepthLF_um, iSteeringAngle,
                       iGeometryLF, iBeam, iMaxBeamDelay, iMinBeamDelay);

```

Listing E.10: Modified beamformer_1p25d.cpp file (Part 3)

```

270     ComputeFocusDelays(iLoLF_el, iHiLF_el, iCenterLF_el,
                       iAzimPitchLF_um, iFocusDepthLF_um, (iSteeringAngle +
                       thSteer), iGeometryLF, iBeam, iMaxBeamDelay,
                       iMinBeamDelay);

```

Listing E.11: Original helperfunctions.h file

```

181 UTILS_API inline float ComputeFocusDelayLA(const float a, const
182       float roc, const float F, const int c0, const float angle)
183 {
184     static const float iPI = (float)IPP_PI;
185
186     if(F == 0.0f)
187         return (1e3f*a*std::tan(angle)/(float)c0);
188
189     float aF, zF;
190
191     aF = a - F*std::cos(0.5f*iPI - angle);
192     zF = F*std::sin(0.5f*iPI - angle);
193
194     float ds = sqrt(aF*aF + zF*zF) - F;
195
196     return std::ceil(1e3f*ds/(float)c0); //in nanoseconds

```

Listing E.12: Modified helperfunctions.h file

```

181 UTILS_API inline float ComputeFocusDelayLA(const float a, const
182       float roc, const float F, const int c0, const float angle)
183 {
184     static const float iPI = (float)IPP_PI;
185     // Changed from tan to sin OFM
186     if(F == 0.0f)
187         return (1e3f*a*std::sin(angle)/(float)c0);
188
189     float aF, zF;
190
191     aF = a - F*std::cos(0.5f*iPI - angle);
192     zF = F*std::sin(0.5f*iPI - angle);
193
194     float ds = sqrt(aF*aF + zF*zF) - F;
195
196     return std::ceil(1e3f*ds/(float)c0); //in nanoseconds

```

E.3 LF Pulser Driver

The final modification that was made to the code in the SURF library, was to a single line in the driver of the LF pulser, the `surflftxfe.cpp` file. Due to the lay-out of a former PCB interface, the output channels of the LF pulser and the channels in the software did not have a one-to-one mapping. The driver therefore remapped the channels in the software. After a considerable amount of debugging and electrical testing, the following line of code was found, and corrected to comply with the mapping of the channels on the new PCB interface.

Listing E.13: Original `surflftxfe.cpp` file

```
74 mReMap = ConfigFile::ParseRange("56:-1:49 64:-1:57 40:-1:33  
48:-1:41 24:-1:17 32:-1:25 8:-1:1 16:-1:9", iDummy);
```

Listing E.14: Modified `surflftxfe.cpp` file

```
74 // Vora remap of channels, to "compensate" for interface between  
LF pulser and the probe  
75 mReMap = ConfigFile::ParseRange("56:-1:49 64:-1:57 40:-1:33  
48:-1:41 24:-1:17 32:-1:25 8:-1:1 16:-1:9", iDummy);  
76 // Skolmen uses a different interface between the LF pulser and  
the probe. Remap is therefore not required  
77 mReMap = ConfigFile::ParseRange("1:64", iDummy);
```

Measurement Parameters

The following sections show the user-defined pre-sets that were used to obtain various measurements presented in Ch. 4 and App. G. In Sec. F.1, the pre-set file that was used to measure the 2D beam profiles of the HF and LF arrays in *Skolmen* is shown.

Parameters that were not set in the pre-set files presented in this chapter, were set by the file `GEN-General (Skolmenmm).xml`, listed in Sec. C.1.2. Parameters that were not set by neither of the two files were set to their default values, listed in `parameters.default.xml`.

F.1 2D Pressure Measurement

The following listing shows the pre-set that was used when measuring the pressure fields emitted by *Skolmen* (App. G).

Listing F.1: The `GEN-Meas_2D_Field (Skolmenmm).xml` configuration file

```

1 <?xml version="1.0" encoding="UTF-8" standalone="no" ?>
2 <preset app="6" factory="0" master="0" probe="4" research="1" version="2"
  xmlns="" xmlns:xsi="http://www.w3.org/2001/XMLSchema-instance"
  xsi:noNamespaceSchemaLocation="../presets.xsd">
3
4   <variables>
5     <variable id="4d-depth" value="109"/>
6     <variable id="4d-roi pixels" value="[R] 142, 405, 217, 572"/>
7     <variable id="b-deviation" value="1250"/>
8     <variable id="b-focus count" value="1"/>
9     <variable id="b-gain" value="900"/>
10    <variable id="b-image rect" value="[R] 0, 540, 0, 63"/>
11    <variable id="color-deviation" value="1250"/>
12    <variable id="focus depth" value="70460"/>
13    <variable id="focus span" value="30000"/>

```

```

14     <variable id="hd-ldensity" value="128"/>
15     <variable id="m-mline pos" value="55"/>
16     <variable id="prf-adjust" value="20000"/>
17     <variable id="pw-gate depth" value="65858"/>
18     <variable id="rx aperture curve 2" value="[C] 1, 0, 0, 50"/>
19     <variable id="soundvelocity" value="1490"/>
20     <variable id="surf-center active lf" value="1"/>
21     <variable id="surf-enable indep focus lf" value="1"/>
22     <variable id="surf-focus depth lf" value="70000"/>
23     <variable id="surf-iq demod freq a" value="2800000"/>
24     <variable id="surf-iq demod freq b" value="2800000"/>
25     <variable id="surf-iq demod lp cutoff" value="1000000"/>
26     <variable id="surf-iq demod lp len" value="50"/>
27     <variable id="surf-lf plane wave" value="1"/>
28     <variable id="surf-outputbits" value="1"/>
29     <variable id="surf-relative apt sz lf" value="150"/>
30     <variable id="surf-rf decimation" value="0"/>
31     <variable id="surf-tx apt max lf" value="16"/>
32     <variable id="surf-tx freq lf" value="500000"/>
33     <variable id="surf-tx voltage lf" value="10"/>
34     <variable id="surf-zero adjust" value="-200"/>
35     <variable id="trigger out" value="1"/>
36     <variable id="trigger out 2" value="2"/>
37     <variable id="tx aperture curve" value="[C] 0, 51, 100, 49"/>
38     <variable id="tx curve depth" value="70000"/>
39     <variable id="tx-delay" value="133"/>
40 </variables>
41
42 <optimizations>
43     <optimization id="b frame rate" value="FrRate High">
44         <variable id="b-ldensity" value="64"/>
45     </optimization>
46     <optimization id="b image" value="General">
47         <variable id="b-tgc" value="[C] 4, 40, 75, 52"/>
48         <variable id="b-voltage [+]" value="15"/>
49         <variable id="b-voltage [-]" value="15"/>
50         <variable id="max fr" value="200"/>
51         <variable id="power" value="5"/>
52     </optimization>
53 </optimizations>
54
55 </preset>

```

F.2 Phantom Recordings

The following listing shows the preset that was used when recording the pulse echo data from the CIRS phantom (Ch. 4).

Listing F.2: The GEN-Phantom (Skolmenmm).xml configuration file

```

1 <?xml version="1.0" encoding="UTF-8" standalone="no" ?>
2 <preset app="6" factory="0" master="0" probe="4" research="1" version="2"
  xmlns="" xmlns:xsi="http://www.w3.org/2001/XMLSchema-instance"
  xsi:noNamespaceSchemaLocation="../presets.xsd">

```

```
3
4 <variables>
5   <variable id="4d-depth" value="14"/>
6   <variable id="4d-roi" value="[R] 22, 178, 14, 63"/>
7   <variable id="4d-roi pixels" value="[R] 17, 56, 386, 449"/>
8   <variable id="b frame rate" value="FrRate Max"/>
9   <variable id="b-depth" value="150"/>
10  <variable id="b-gain" value="1200"/>
11  <variable id="b-image rect" value="[R] 0, 1948, 0, 63"/>
12  <variable id="b-iq-bottom freq depth" value="150"/>
13  <variable id="b-persistence" value="0"/>
14  <variable id="b-reject" value="5"/>
15  <variable id="focus boundaries" value=""/>
16  <variable id="m-mline pos" value="62"/>
17  <variable id="mru filtering" value="Clarity Off"/>
18  <variable id="prf-adjust" value="10000"/>
19  <variable id="pw-gate pos" value="62"/>
20  <variable id="surf-center active lf" value="1"/>
21  <variable id="surf-enable indep focus lf" value="1"/>
22  <variable id="surf-focus depth lf" value="70000"/>
23  <variable id="surf-hf pos" value="40"/>
24  <variable id="surf-iq demod freq a" value="2800000"/>
25  <variable id="surf-iq demod lp cutoff" value="500000"/>
26  <variable id="surf-lf plane wave" value="1"/>
27  <variable id="surf-mode on" value="1"/>
28  <variable id="surf-outputbits" value="1"/>
29  <variable id="surf-process type" value="1"/>
30  <variable id="surf-relative apt sz lf" value="150"/>
31  <variable id="surf-rf decimation" value="0"/>
32  <variable id="surf-tx apt depth lf" value="70000"/>
33  <variable id="surf-tx apt max lf" value="16"/>
34  <variable id="surf-tx freq lf" value="500000"/>
35  <variable id="surf-tx voltage lf" value="100"/>
36  <variable id="surf-win len" value="3000"/>
37  <variable id="surf-zero adjust" value="360"/>
38  <variable id="trigger out" value="1"/>
39  <variable id="trigger out 2" value="2"/>
40  <variable id="tx-delay" value="70"/>
41 </variables>
42
43 <optimizations>
44   <optimization id="b image" value="General">
45     <variable id="b-iq-bottom freq" value="2800000"/>
46     <variable id="b-iq-cutoff freq" value="5"/>
47     <variable id="b-iq-top freq" value="3200000"/>
48     <variable id="b-iq-window factor" value="7"/>
49     <variable id="b-tgc" value="[C] 0, 0, 100, 25"/>
50     <variable id="max fr" value="0"/>
51     <variable id="power" value="14"/>
52   </optimization>
53 </optimizations>
54
55 </preset>
```


Measurements

Measurements of the fields emitted by *Skolmen* were measured in a water tank in order to verify pulse forms and increase simulation accuracy. A number of measurements of the scanner and electronics were also made to verify This chapter describes the measurement methods, discusses their validity, and presents the results.

Good simulations of the transmitted field from a SURF transducer are essential to setting up transmit situations which produce highly linear development of non-linear propagation delay. As mentioned, the linearity of this parameter with depth is advantageous to suppress acoustic noise.

It has previously been observed that simulated and measured non-linear propagation delays deviate when using simplified near-field pressure fields for simulation initialisation, for instance when using *xTrans* [51] to create such an initial field. The discrepancy between simulations and measurements may be attributed to several factors, including

- Intra-array element variation (not included in *WaveSim* or *xTrans*)
- Element vibration patterns (only piston models are used)
- Element directivity (not included in *WaveSim* or *xTrans*)
- Inter-array and intra-array cross-coupling between elements (Not included in any simulation software).

To more accurately estimate the expected development of non-linear propagation delay, the fields emitted by *Skolmen*'s HF and LF arrays were measured in a water tank. The measurements were made as closely as possible to the transducer surface, and the pressure amplitudes were kept moderately low to minimize

non-linear propagation effects through the water while preserving a satisfactory signal-to-noise ratio in the measured signal. The measurement procedure and results are presented in Sec. G.3.

It was hypothesised that using measured pressure pulses from a two-dimensional grid directly in front of the transducer as an initial field in *WaveSim* would provide a better simulated estimate of non-linear propagation delay. As an added benefit, the technique could be used to increase the fidelity of non-linear pulse form distortion correction filters.

The manipulation pulses from the LF array were also measured close to the transducer in order to evaluate the frequency content of the transmitted pulses. Jahren [51] pointed out that the presence of HF components in the LF pulse could be detrimental to estimation of non-linear propagation delay, and therefore also to the suppression of reverberation noise. The measurements were taken according to the method described in Sec. G.4, and the results are also presented there.

G.1 Equipment List

The following list of equipment was used to take the measurements in Sec. G.3 and Sec. G.4.

- An Ultrasonix SonixMDP scanner in Research mode, with SURF software library
- The SURF Technology Two-Tone LF pulser
- SURF probe interface
- SURF ultrasound probe *Skolmen*
- LeCroy WaveSurfer 44Xs oscilloscope
- A $0.45 \times 0.45 \times 0.30\text{m}$ container of degassed water
- Onda HGL-0200 hydrophone, S/N 1426
- Onda AH 2010 hydrophone preamplifier, S/N 1223
- Onda AH-2010-DCBNS DC block S/N 0310
- 3 Physik Instruments 513.51S stepper motors (positioning robot)
- Desktop computer with ProbeLab 1.5
- A vice to hold the probe

G.2 LF Pulser Voltage

A real concern when using *Skolmen* to perform measurements was that it is an expensive prototype transducer, and there was not a lot of information available about its efficiency or what kind of voltages that could be used without damaging the probe. The first dataset that was acquired from measurements in a phantom proved to be of little interest since the LF voltage that was used was not high enough that non-linear propagation effects were observed.

The LF pressure was measured in the near-field of the LF array, when using different voltages to drive the array. The results of the measurements are shown in Fig. G.1. Jahren [51] obtained satisfactory estimates of non-linear propagation delay when using near-field pressures of 400 kPa to 500 kPa. However, these pressures were achieved when using excitation voltages in the range of 30 V to 50 V. Using *xTrans*, the design stack of Jahren's probe was simulated for comparison with *Skolmen*. The absolute values of the electro-acoustic transfer functions at the centre frequency of both the probes were compared, and it was found that the expected pressure from *Skolmen* was 45% of the expected pressure from Jahren's transducer. This corresponded well with the comparison of measurements in Fig. G.1 and corresponding measurements that were done by Jahren [51].

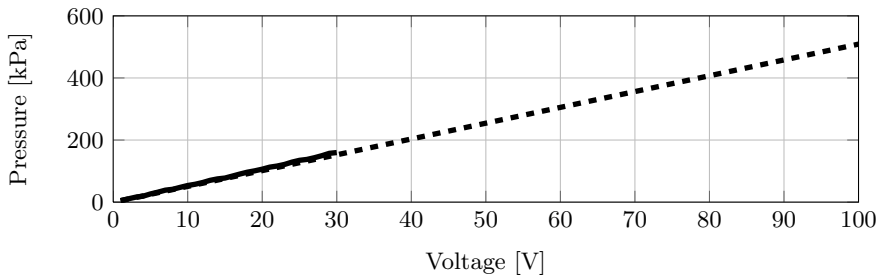


Figure G.1: LF near-field spatio-temporal peak pressure amplitude as a function of pulser voltage. The excitation frequency was set to 0.5 MHz, and the pulse length was 5 half-cycles. The solid line indicates the measured pressure, and the dashed line is the linear extrapolation of the data.

It has been reported [75] that an average power per unit area of an imaging transducer above approximately $\bar{I}_{el} = 2.2 \text{ W cm}^{-2}$ is not recommended when transducer efficiency is around 20%. When so much of the input energy is dissipated as heat in the transducer, the risk of temperature-induced damage to the probe is very real. Therefore, the value reported by deBruijn was used as a benchmark for how much power could be used with the LF array in *Skolmen*, since the efficiencies of the LF elements were estimated to be around 20%.

The estimated efficiency of a single LF element is shown in Fig. G.2, as a function of frequency. The curve has been band-pass filtered around the main

band of the excitation pulse, which was a 0.5 MHz sine wave with a length of two periods. To calculate the efficiency, the pressure field emitted by the element was measured in water, in a large plane approximately perpendicular to the propagation direction. The voltage at the channel input was also measured, and the power in the pressure field was compared to the electrical input power. It was assumed that electrical losses and absorption were negligible.

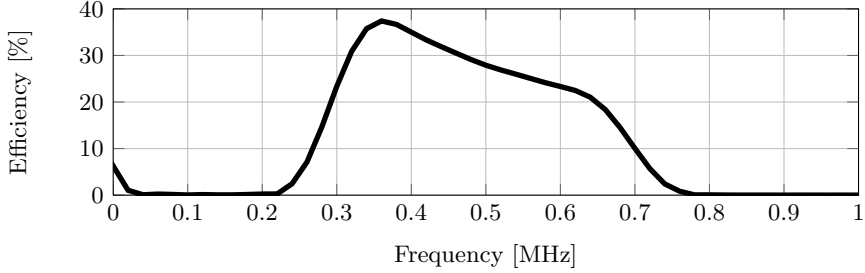


Figure G.2: Estimated LF element efficiency as a function of frequency. A band-pass filter with -3 dB cut-off frequencies at 300 kHz and 700 kHz.

With an element area A_{LF} , an average input power of \bar{P}_i , and a duty cycle D , the following constraint was formulated

$$\bar{I}_{el} A_{LF} > D \bar{P}_i \quad (\text{G.1})$$

Using that the duty cycle of the voltage is determined by the maximum imaging depth, the frequency of the transmitted pulse, and the number of half-cycles in the excitation, one can write that $D = T_{on}/T_{tot} = N_{HC} T_p c_0 / 2z_{max}$, where N_{HC} is the number of half-cycles, T_p is the period of the excitation pulse, c_0 is the average speed of sound in the target tissue, and z_{max} is the maximum imaging depth.

Furthermore, the average power in a rectangular pulse can be calculated as $\bar{P}_i = (V_{pp}/4)^2 / Z_i$, where V_{pp} is peak-to-peak voltage amplitude, and Z_i is the input impedance of the LF channel. By using these calculations, Eq. (G.1) can be rewritten, associating minimum imaging depth with excitation voltage and length.

$$z_{max} > \frac{N_{HC} T_p V_{pp}^2 c_0}{64 Z_i \bar{I}_{el} A_{LF}} \quad (\text{G.2})$$

Doing the calculation in Eq. (G.2) with 200 V peak-to-peak excitation voltage, an excitation length of 5 half-cycles, and $Z_i = 200 \Omega$ yields a minimum imaging depth of 9.11 cm. In other words, the peak-to-peak voltage could safely be increased to 200 V, when imaging down to a depth of 15 cm, providing a near-field peak LF pressure of around 500 kPa.

In Fig. G.3, the minimum requirement on the maximum imaging depth is shown, as a function of pulser voltage amplitude.

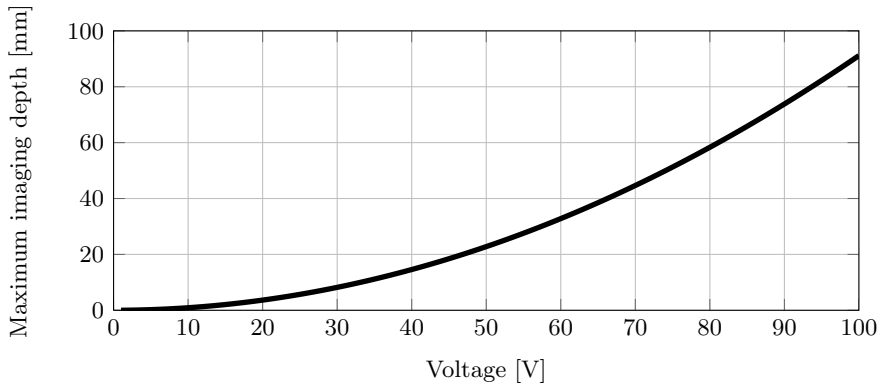


Figure G.3: The minimum required maximum imaging depth as a function of pulser voltage, to limit the average power per area to $\bar{I}_{el} = 2.2 \text{ W cm}^{-2}$. The formula in Eq. (G.2) is used with $N_{HC} = 5$, $T_p = 2 \mu\text{s}$, $c_0 = 1540 \text{ m s}^{-1}$, $Z_i = 200 \Omega$, $\bar{I}_{el} = 2.2 \text{ watt/cm}^2$, and $A_{LF} = 0.24 \text{ cm}^2$

G.3 2D Near-Field Pressure

The following section details the measurement of the near-field pressure emitted by *Skolmen's* HF and LF arrays.

All the pressure measurements were performed in a water tank at the ultrasound lab at the Department of Circulation and Medical Imaging (ISB) at St. Olavs Hospital in Trondheim.

The lab has a hydrophone logging system which ensures that all hydrophones are calibrated at regular intervals. It also uses an in-house software module for MATLAB called ProbeLab, which simultaneously controls three robotic arms and communicates with an oscilloscope so that hydrophone positioning and oscilloscope readings are associated with one another. The hydrophone and robot are positioned so that the robot depth axis is perpendicular to the water surface, and the other two axes are parallel to the surface. Thereby, the movement axes of the hydrophone constitute a right-hand oriented coordinate system. These axes will be referred to as the depth, azimuth and elevation axes of the robot.

All the measurements in the water tank were taken using ProbeLab to control hydrophone positions and to retrieve data from the oscilloscope. A full list of the parameter values that were used on the SonixMDP scanner can be found in Sec. F.1.

G.3.1 Measuring the HF and LF near-field

In order to measure the near-fields of the arrays as accurately as possible, the orientation of the probe was assiduously adjusted so that the surface of the probe was perceived to be parallel to the water surface. The hydrophone was then placed disconcertingly close to the transducer surface by measuring the relative relation between an emitted pulse and the hydrophone-transducer-hydrophone reverberation noise. Looking at Fig. G.7, the reverberation between the hydrophone and the probe can be seen on the tail of the main pulse. Increasing the distance between the probe and the hydrophone increased the distance between the main pulse and the tailing pulse by an amount of time proportional to the increase in distance. Therefore, it was concluded that this tailing pulse was indeed reverberation between the source and the receiver.

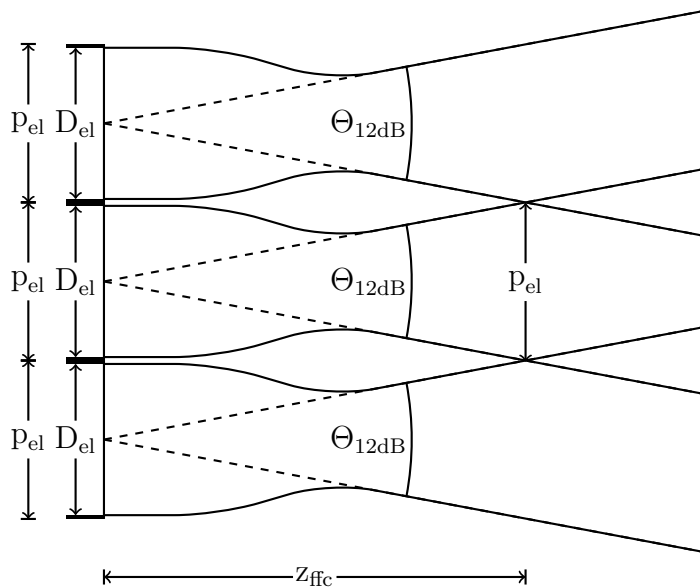


Figure G.4: The figure shows how the 12 dB beam profiles of three closely spaced elements overlap as the distance from the element increases. A good way of measuring the near field profile of an array transducer would be to use z_{ffc} as the measurement depth and step transversally in steps of p_{el} . In practice it is difficult to achieve this when the distance from the elements to the front face of the transducer, and the materials in between are unknown.

One-dimensional beam profile scans were performed in order to confirm that the probe was sufficiently parallel to the surface and the azimuthal and elevational axes of the robot. This was done by comparing the time delay from pulse trigger signal to the arrival of the pulse at the hydrophone, for each measurement position along the line. The probe was set to transmit plane waves, using the entire array

Table G.1: 2D near-field measurement grid specification.

	HF	LF
Azimuth start	-11.00 mm	-16.00 mm
Azimuth end	9.00 mm	14.00 mm
Azimuth precision	0.25 mm	0.50 mm
Elevation start	-9.00 mm	-11.00 mm
Elevation end	7.00 mm	9.00 mm
Elevation precision	0.50 mm	0.50 mm
Depth	0.00 mm*	0.00 mm*
Number of points	2673	2108

*In the coordinate system of the positioning robot, *i.e.* as close to the front face of the probe as possible.

width. The results for the HF and LF arrays can be seen in Fig. H.1 and H.2, respectively.

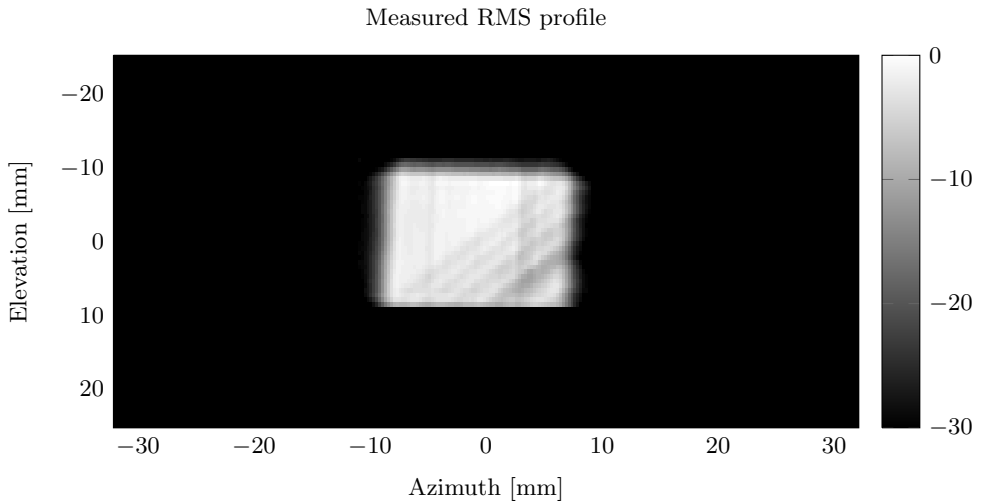
After obtaining satisfactory probe position, two 2D measurement grids were defined to measure the near-field pressure emitted by the two arrays. The details of the grids can be seen in Tab. G.1. The positions are given in millimetres relative to the defined origin of the robot coordinate system.

Measurements were taken at each point in the grid as beam number 31 of 64 was fired. At each point the pulse was measured a number of times and averaged in order to improve signal-to-noise ratio, *i.e.* the pulses were averaged over a number of frames. In the case of the HF array, the averaging number was 32, whereas only 8 pulses were needed for the LF pulses. This was because a 3 bit low pass noise filter with -3 dB at $f = 1.6$ MHz was applied by the oscilloscope on each measured pulse. The HF pulses were sampled by the oscilloscope at 500 MHz and the LF pulses were sampled at 200 MHz, and all stored signals consisted of 10 000 time samples.

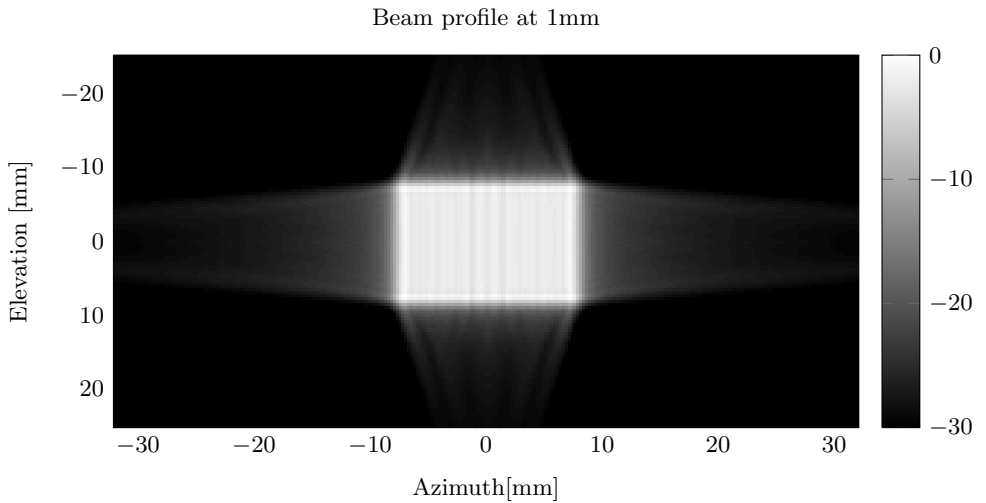
The 2D beam profiles of the arrays are shown alongside simulated beam profiles in Fig. G.5 and Fig. G.6. The beam profiles were simulated by using a combination of the simulation tools *xTrans*, *Field II* [76, 77] and *WaveSim*.

G.3.2 The Influence of Non-linear Effects

As shown by Muir and Carstensen [37], water is a highly non-linear fluid in which shock formation occurs rapidly in transmitted waves. The paper shows that the source intensity must be larger than 1 kW cm^{-2} for a plane wave with a centre frequency of 3 MHz to develop weak shock formation after travelling a distance of less than 1 cm. In the measurement set-up, the distances between the

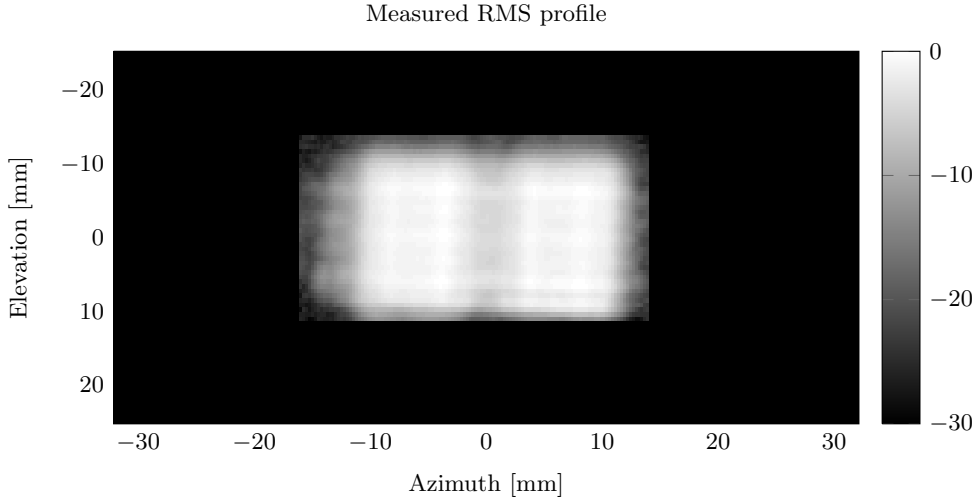


(a) The measured beam profile of the HF array

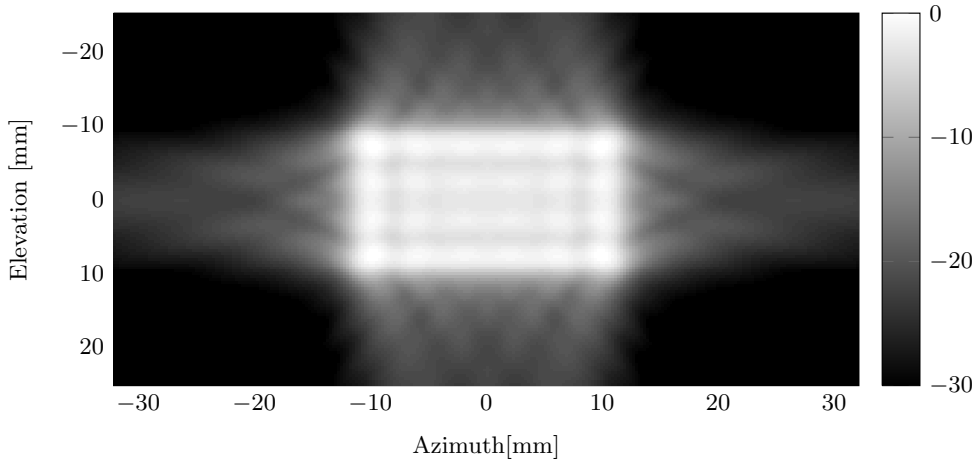


(b) The simulated beam profile of the HF array.

Figure G.5: Measured and simulated RMS beam profiles of the HF array. The scale is in desibels, and the measured profile has been padded with zeros to have the same grid size as the simulated array profile.



(a) The measured beam profile of the LF array
Beam profile at 1mm



(b) The simulated beam profile of the LF array.

Figure G.6: Measured and simulated RMS beam profiles of the LF array. The scale is in desibels, and the measured profile has been padded with zeros to have the same grid size as the simulated array profile.

transmitting arrays and the hydrophone were significantly less than 1 cm and the source intensities were less than 100 mW cm^{-2} .

In Fig. G.7, an example of the received signal on the hydrophone is shown. The high frequency noise in front of the main pulse was assumed to be electrical cross-coupling from the array to the hydrophone, indicating the time at which the array was excited. The pulse arrived approximately $0.5 \mu\text{s}$ later, which corresponds to a distance of $0.75 \mu\text{m}$ in water at 23.6°C . That is equivalent to $1.4\lambda_c$ when $f_c = 2.8 \text{ MHz}$.

The same distance between the probe surface and the hydrophone was used when measuring the near-field profile of the LF array. In Fig. G.8, the signal that was recorded by the hydrophone when the LF array was excited is shown. The high frequency noise at the beginning of the signal was located at the same position and had the same magnitude, regardless of the position of the hydrophone. It was therefore concluded that the noise occurred due to electrical coupling from the low frequency array electrodes to the hydrophone electronics. Furthermore, the number of noise pulses varied with the number of half-cycles of the LF excitation voltage. Therefore, the a conclusion was drawn that the noise pulses were products of the zero-crossings in the excitation voltage. This theory was not pursued or verified since the observations fell outside the scope of the project.

With the help of Muir and Carstensen [37], it was concluded that the pressure pulses measured by hydrophone in a plane close to the transducer surface were representative of the pressure pulses at the surface of the transducer. The measurements were carried out so that non-linear effects were negligible, and would thus provide a good basis on which to do field simulations.

G.4 Verification of Pulse Forms

Based on the observations in Jahren [51], the spectra of the transmitted pulse forms have been of interest prior to recording phantom data. The HF components in the LF pulses must be negligible in order for the SURF technique to be effective, particularly around strong scatterers. HF components in the LF pulse will disrupt the estimation of non-linear propagation delay, making it much more difficult to *e.g.* suppress reverberations.

The measured near field pulse forms are shown in Fig. G.7 and G.8.

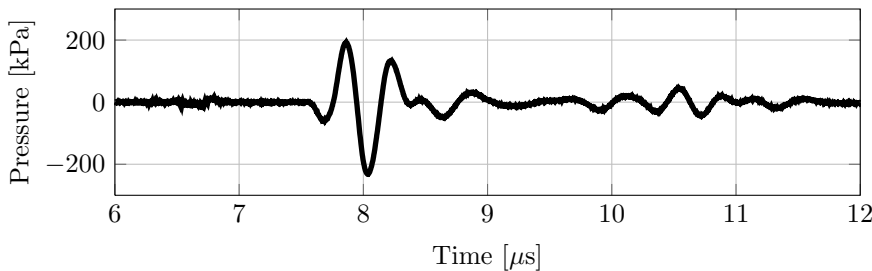


Figure G.7: Measured HF pulse in the near field of the transducer

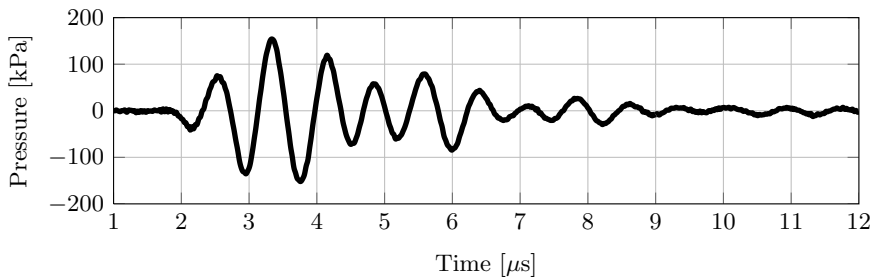


Figure G.8: Measured LF pulse in the near field of the transducer

The spectrum of the HF pulse, shown in Fig. G.9, reveals that the HF pulse has a main frequency band centered at 2.5 MHz, with a bandwidth of 2.2 MHz, *i.e.* a relative bandwidth of 88 %. The spectrum has been calculated by using a sharp Tukey window around the main pulse in Fig. G.7 and applying the fastfourier transform (FFT) on the remaining pulse. The signal was windowed to avoid using reverberation noise in the calculation, and the result was a smoother magnitude response.

Similarly, the spectrum of the LF pulse in Fig. G.8 was calculated after applying a 100th order digital low pass filter with a cut-off frequency at 10 MHz. The MATLAB functions `fir1` and `filter` were used in the implementation of the filter. The resulting spectrum can be seen in Fig. G.10. The main lobe of the spectrum is centered around 0.5 MHz with a bandwidth of approximately

0.1 MHz. As the frequency increases into the range of the HF band, the LF spectrum magnitude drops off towards the noise floor of the measurement.

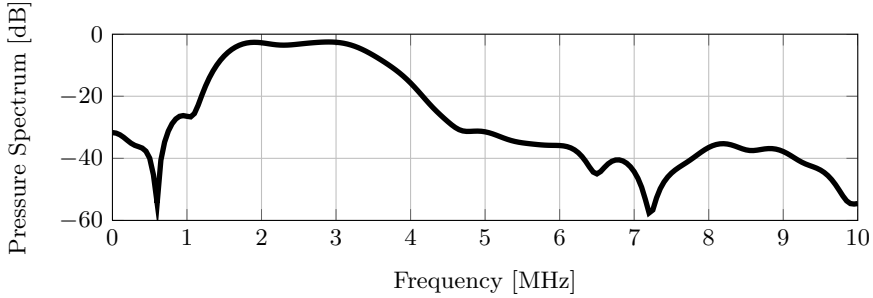


Figure G.9: Pressure spectrum of the windowed measured HF pulse in the near field of the transducer. The reference value, 0 dB, is defined as the maximum value in the spectrum of the original HF pulse.

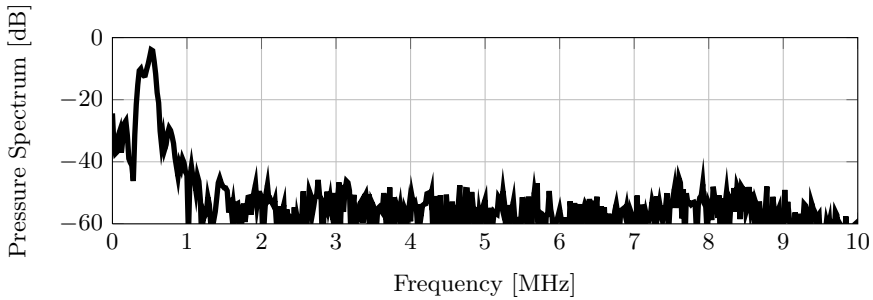


Figure G.10: Pressure spectrum of the windowed measured LF pulse in the near field of the transducer. The reference value, 0 dB, is defined as the maximum value in the spectrum of the original HF pulse.

G.5 Experiments on Array Function

By using a combination of the *FieldII* and *xTrans* simulation tools, it was expected that the discrepancy between measured and simulated RMS pressure profiles would be small. Some deviation from simulations can always be expected in a measurement situation since simulations rarely paint complete pictures of physical situations. However, the profiles in Fig. G.5 and G.6 were sufficiently contrasting that further measurements were taken to examine the functionality of the arrays. The LF array was of particular interest because of the software adjustments that were made in order for the system to function properly.

G.5.1 Persuing the Elements

A couple of simple azimuthal near field beam profile measurements were taken to inspect the RMS pressure and the curvature of the emitted LF pressure pulses. As in Sec. G.3, the probe was held still, with its face submerged in the water tank, and the hydrophone was moved in equidistant increments by the positioning robot. 64 pressure measurements were made at each point, and averaged. Each pressure measurement was triggered by a trig signal from the SonixMDP scanner, marking the transmission along the 31st scan line of the frame. All the parameters are listed in Sec. F.1, and the results can be seen in Fig. G.11. The HF profile was not investigated further since no modifications were made to the software controlling the steering and beam-forming of the array.

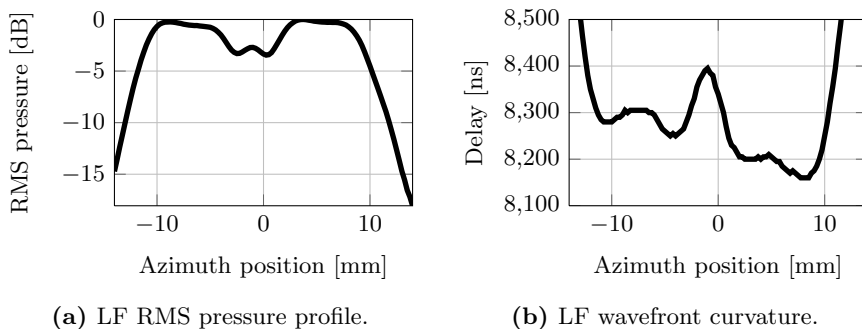


Figure G.11: The azimuthal RMS pressure profile of the LF array, and the curvature of the emitted wave front. The measurements were taken approximately one millimetre from the front face of the probe. The curvature of the wave front is measured as the delay between the scanner pulse trig and the arrival time of the peak pressure at each hydrophone position.

The 3.5 dB drop in RMS pressure in the centre of the pressure field emitted from the array, along with the increase in delay at the same position indicated that there could be a malfunctioning element in the centre of the array. Measuring the voltage on the output of the LF pulser showed that the voltage over a central element (element no. 9) exhibited much longer and more vigorous ringing than the other elements in the array, further supporting the theory that the element was out of order. The voltages over each LF element, while exciting all of the elements simultaneously with the LF pulser, are shown in Fig. G.12.

Further investigation of the elements was done by using a Tabor WW2741 arbitrary waveform generator to excite each element individually, and thereby independently of one another. The generator was connected to each channel of the LF array in turn by using a DLP-408 receptacle, and a custom made measurement rig [64] as an interface between the generator's BNC output and the DLP-408 connector. The voltage on the output of the generator was monitored using the LeCroy 44Xs Wave Surfer oscilloscope, which was triggered by the internal trigger

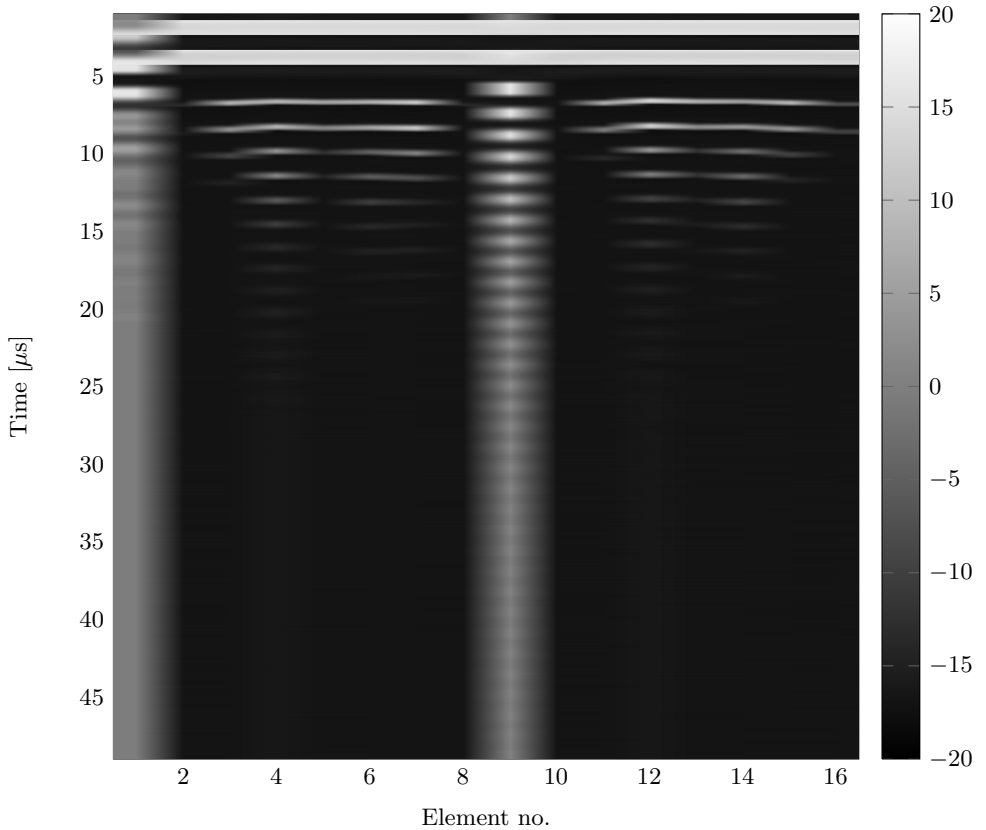


Figure G.12: Voltage over the channels of the LF array as a function of time, when exciting all of the elements equally and simultaneously with the LF pulser. Excitation voltage is 16 V and the color scale is in Volts. In this case, the excitation pulse was limited to four half cycles in order to compare the results with the voltages in Fig. G.13, where an arbitrary wave form generator was used to excite each element individually.

of the wave form generator. The resulting voltage over each individual element can be seen in Fig. G.13.

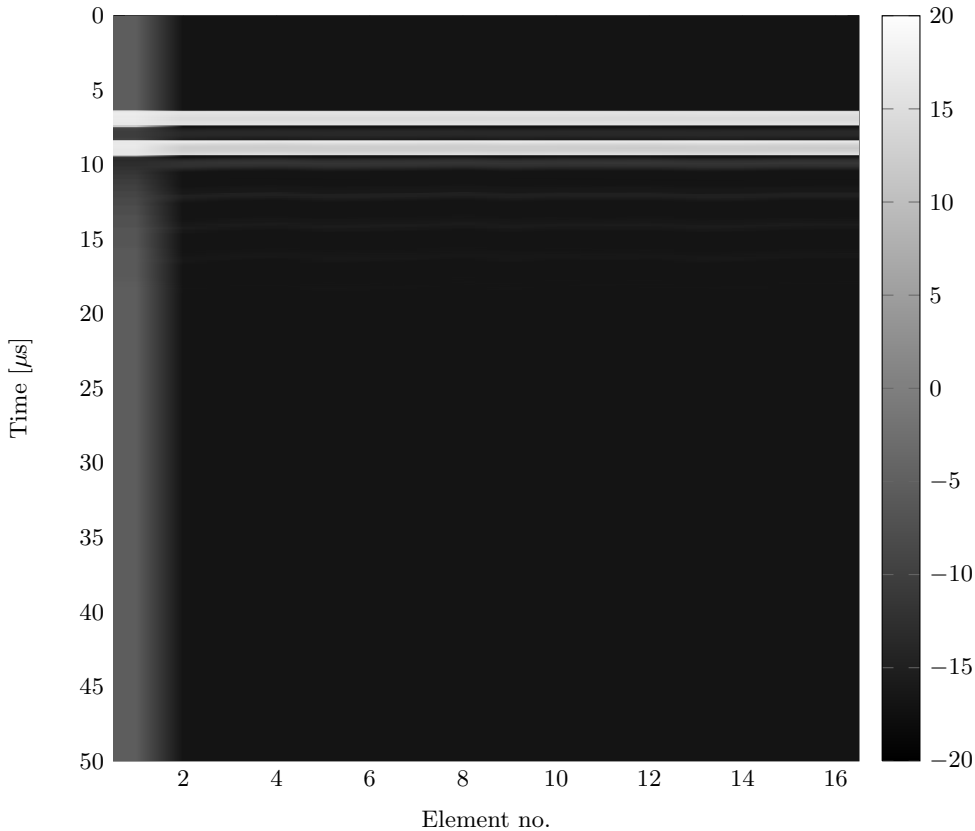


Figure G.13: Voltages over the channels of the LF array as a function of time, when exciting each element individually and at separate time points. Excitation voltage is 16 V, and the pulse is four half cycles long. The color scale on the right is in Volts.

The results from these two measurements disproved the hypothesis that the ninth element of the LF array was broken. In fact, all the components of the system from the connector to the elements themselves were proven to be operating in approximately the same manner by the results in Fig. G.13¹. Further confirmation that elements in the centre of the array were functioning normally in an acoustic manner as well as electrically, was obtained in beam profile measurements of two neighbouring elements. The RMS pressure was measured in the same manner as the profiles in Fig. G.11, and are shown in Fig. G.14.

It was concluded that the elements and other components in the peripheral

¹Excepting LF element number 1, but this element was known to be malfunctioning [64].

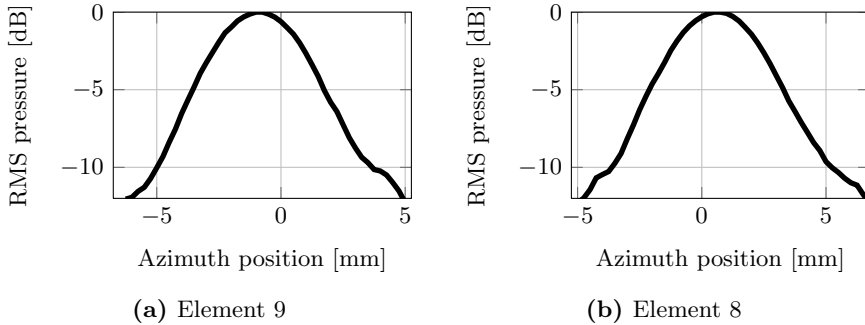


Figure G.14: The azimuthal RMS pressure profiles of the eighth and ninth elements in the LF array. A wave form generator was used to excite each element individually, at different points in time.

part of the system, beyond the front-end electronics, were not to blame for the observed variation in transmitted LF pressure and delay. No measurements were taken to verify the fidelity of the probe interface PCB, because of its simple design. The next step was to examine the output of the LF pulser itself more thoroughly.

G.5.2 Purging the Pulser

Having ruled out the possibility that the transducer and other components peripheral to the output of the LF pulser were to blame for the discrepancy in the LF pressure profile and wave front, the voltages that were produced by the LF pulser were examined.

The pulser output channels were disconnected from the ultrasound probe interface PCB and an electrical probe was connected to each transmitting channel of the pulser in turn. The electrical probe was terminated in a $50\ \Omega$ load, with an oscilloscope connected to the same node as well. A high impedance was selected on the oscilloscope, so that the total load on the pulser was approximately $50\ \Omega$, while the front-end electronics of the oscilloscope was protected.

The LF pulser was set to start transmitting via the imaging software on the SonixMDP, as if it were connected to *Skolmen*. The pulser and the oscilloscope were simultaneously triggered by the frame and pulse triggers from the SonixMDP, in the same manner as when taking pressure measurements with a hydrophone. Each channel was loaded with the $50\ \Omega$ load in turn, and the voltage over the load was measured 64 times for each channel, and averaged.

The voltages produced by each transmit channel were identical, and each channel was excited with the same delay, relative to the trig from the SonixMDP. The resulting pulse forms were very similar to those measured by Rau [50]. Thus,

the pulser was not only operating as it should electrically, it was also being triggered correctly. This indicated that neither the drive circuits of the LF pulser, nor the software adjustments were to blame for the effects seen in Fig. G.6.

G.5.3 LF Cross Coupling

As shown in Fig. A.4, the data that is received by the LF pulser suggests that the beams that are emitted by the LF array should be steered in the same direction as the HF beams. However, initial recordings with a phantom suggested that this was not the case. The non-linear propagation delay that was calculated from the initial phantom data exhibited substantial transversal variation, indicating that the LF pressure observed by the HF pulse varied with beam direction. Transversal variation in non-linear propagation delay is, in itself, not a problem with respect to reverberation suppression as long as the radial accumulation of delay is sufficiently linear and has sufficient magnitude. It does, however, cause issues with the quality of the beam interpolation that speeds up data acquisition, as will be discussed in Ch. 5.

The transversal variation suggested that something could be seriously wrong with the beam-forming, but this hypothesis was rejected as soon as the LF pulser memory could be studied. Further investigation of the output voltages of the LF pulser revealed that the wave forms on certain channels became strange as the steering angle was increased. Since Myhre [64] only investigated the cross-coupling between the central element of the LF array and the other elements of the array, the DC resistance between neighbouring channels of the LF array were measured at the probe connector. The measurements revealed a substantial amount of electrical coupling between individual array elements. The results can be seen in Tab. G.2.

By using the knowledge that the first LF element is shorted to ground in the probe housing and that the DC impedance of the elements is very large, one can conclude that a $50\ \Omega$ DC resistance between two channels implies that the electrodes of two elements are shorted together. The serial DC resistance of the channels is defined by a series inductor and a coaxial cable, which is known to be $22\ \Omega$ from Tab. G.2. If two electrodes are coupled together, the DC resistance will be twice as high. The situation is illustrated in Fig. G.15, and the DC resistance between CH1+ and CH2+ can be approximated as

$$R_{DC} \approx 2(Z_{T,DC} + Z_0) \quad (\text{G.3})$$

Although the figure only shows two elements in parallel, the amount of elements connected in parallel is arbitrary and does not affect the measured impedance. Thus, a single impedance measurement does not relate how many elements are connected in parallel in the probe housing.

The measurements in Tab. G.2 show that subsets of the LF array are connected in parallel in the probe housing. This means that elements 2–5, 10–14,

Table G.2: The inter-element DC resistance in ohms, between the elements in the *Skolmen* LF array. The X denotes invalid combinations, and Z denotes an impedance in excess of 10 M Ω .

CH	GND	1	2	3	4	5	6	7	8	9	10	11	12	13	14	15	16	
1	22	X	Z	Z	Z	Z	444	44	Z	Z	Z	Z	Z	Z	Z	Z	Z	
2	Z	Z	X	50	54	56	Z	Z	Z	Z	Z	Z	Z	Z	Z	Z	Z	
3	Z	Z	50	X	50	50	Z	Z	Z	Z	Z	Z	Z	Z	Z	Z	Z	
4	Z	Z	54	50	X	48	Z	Z	Z	Z	Z	Z	Z	Z	Z	Z	Z	
5	Z	Z	56	50	48	X	Z	Z	Z	Z	Z	Z	Z	Z	Z	Z	Z	
6	444	444	Z	Z	Z	Z	X	444	Z	Z	Z	Z	Z	Z	Z	Z	Z	
7	22	44	Z	Z	Z	Z	444	X	Z	Z	Z	Z	Z	Z	Z	Z	Z	
8	Z	Z	Z	Z	Z	Z	Z	Z	X	Z	Z	Z	Z	Z	Z	Z	Z	
9	Z	Z	Z	Z	Z	Z	Z	Z	Z	X	Z	Z	Z	Z	Z	Z	Z	
10	Z	Z	Z	Z	Z	Z	Z	Z	Z	X	52	48	49	50	Z	Z	Z	
11	Z	Z	Z	Z	Z	Z	Z	Z	Z	Z	52	X	47	48	49	Z	Z	
12	Z	Z	Z	Z	Z	Z	Z	Z	Z	Z	48	47	X	48	48	Z	Z	
13	Z	Z	Z	Z	Z	Z	Z	Z	Z	Z	49	48	48	X	47	Z	Z	
14	Z	Z	Z	Z	Z	Z	Z	Z	Z	Z	50	49	48	47	X	Z	Z	
15	Z	Z	Z	Z	Z	Z	Z	Z	Z	Z	Z	Z	Z	Z	Z	X	47	
16	Z	Z	Z	Z	Z	Z	Z	Z	Z	Z	Z	Z	Z	Z	Z	Z	47	X

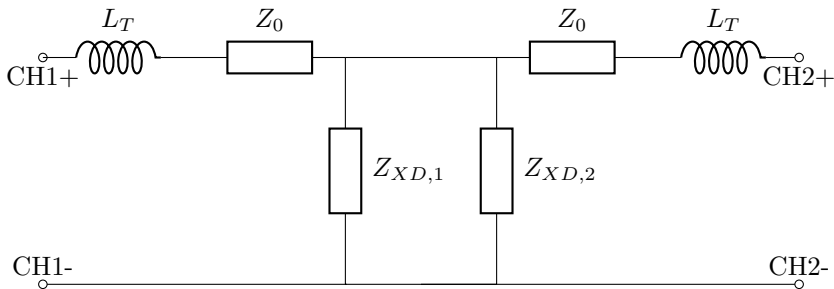


Figure G.15: A circuit diagram showing two elements that are coupled together in the probe housing.

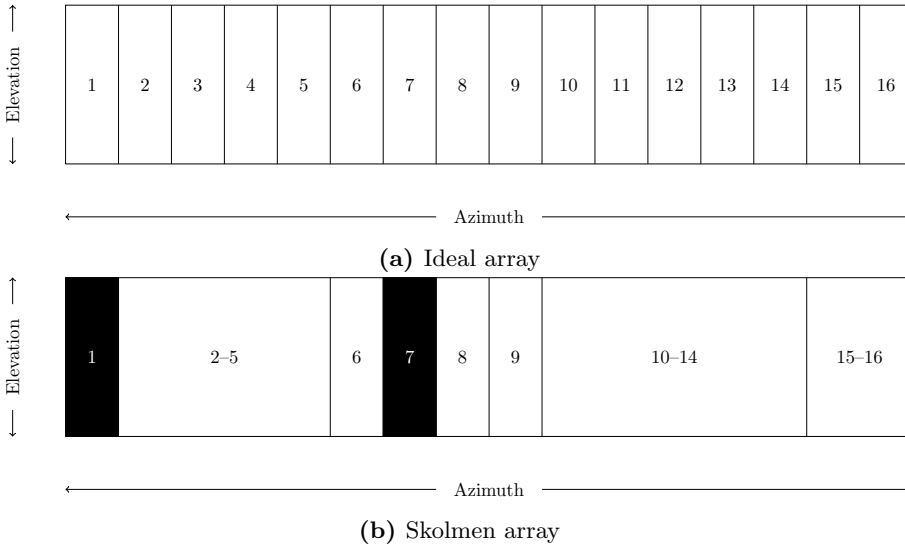


Figure G.16: Illustration of the elements constituting an array. White areas indicate functioning elements, whereas black areas indicate dead elements. The top figure shows how the LF array in *Skolmen* was expected to be partitioned into elements, and the lower figure shows the division and function that is indicated by the DC resistance measurements.

and 15–16 vibrate in unison when the entire LF array is excited in a plane wave, with no steering angle or focusing. Therefore, the measurements presented in Sec. G.3, G.4, and G.5, which were all conducted with the LF array radiating a plane wave straight forward, could not detect the presence of such cross-coupling. An illustration of the expected array function, and the measured array function is shown in Fig. G.16.

As the array is steered, the individual elements are excited subsequently. This means that the elements that are coupled in parallel with one another, are excited with multiple pulses while they are still vibrating due to previous excitations. The beam profile of the transmitted wave will thus be dependent on the delays that are applied to the excitation pulses. Additionally, the variation in effective element size across the width of the transducer will cause the spatial impulse response to change. In short, the transducer will not function as expected, and the result is that the HF and LF waves will only co-propagate as intended when the transmit beam is directed straight forward, without LF focusing.

G.5.4 Concluding Remarks

Careful troubleshooting of the front-end electronics uncovered no serious errors with any of the individual components. Furthermore, the delay settings done by

the new software adjustments were found to be correct. Explaining the effects that were observed in Fig. G.6 is difficult beyond concluding that the most likely culprit is cross-coupling effects within the LF array. A less likely explanation could be that the probe interface PCB has a fault.

The final measurement presented in this chapter uncovered serious deficiencies with the LF array elements. These were not discovered when doing cross-coupling measurements because cross-coupling was only measured with relation to LF element 8, which is one of the few well-functioning elements in the array.

Additional Measurements

The performance of the *Skolmen* probe was thoroughly investigated prior to the phantom measurements to ensure that the software adjustments of App. E were functioning properly, and to acquire measurement data for the purpose of simulating the non-linear forward propagation more accurately. Not all the measurement data was presented in App. G, because of the limited relevance to the project. However, the measurements are included to illustrate that the function of the array was satisfactory.

The measurements presented in this chapter are measurements of the curvature of the wave fronts from the HF and LF arrays. Section H.1 comments on the measurements. The azimuth and elevation beam profiles of the LF array are shown in Sec. H.2, for three different depths.

All the measurements were made in the same session as the water tank measurements in App. G, with the same set-up. Beam focusing was turned off as the measurements were made, *i.e.* all transmitted waves were plane waves.

H.1 Wave Front Curvatures

Figure H.1 and H.2 show the measured curvatures of the wave fronts emitted by the HF and LF arrays, respectively. The linear components in these figures can be attributed to the possibility that the scanning plane of the robot was not parallel to the arrays. However, the difference in the slope of the linear components is surprising. This suggests that at least one of the following statements is true:

1. The LF and HF array are not parallel to one another.
2. The HF and LF beams are not steered in the same direction.

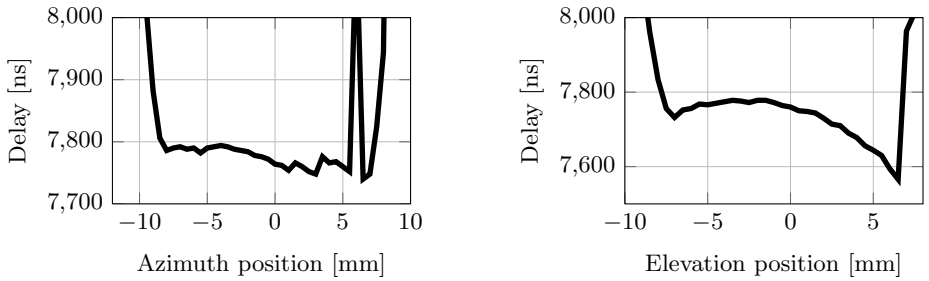


Figure H.1: HF wave front curvatures. The linear slope in azimuth is approximately $\Delta t_{HF,a}/\Delta s_{HF,a} = 3.125 \text{ ns mm}^{-1}$, and in elevation it is $\Delta t_{HF,e}/\Delta s_{HF,e} = 10.9 \text{ ns mm}^{-1}$

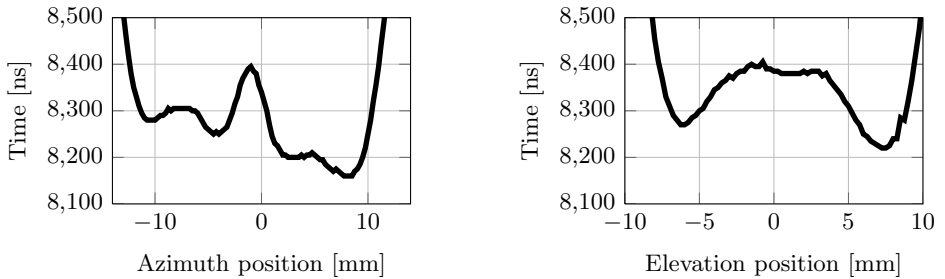


Figure H.2: LF wave front curvatures. The linear slope in azimuth is approximately $\Delta t_{LF,a}/\Delta s_{LF,a} = 5.5 \text{ ns mm}^{-1}$, and in elevation it is $\Delta t_{LF,e}/\Delta s_{LF,e} = 3.125 \text{ ns mm}^{-1}$

The consequences of this misalignment should not be very great. Using simple trigonometry the misalignment of a beam at a depth z can be calculated as

$$\delta h = z c_0 \frac{\Delta t}{\Delta s} \quad (\text{H.1})$$

where $\Delta t/\Delta s$ is the slope of the linear components in the wave front curvature. c_0 is the speed of sound. By taking the measurement plane as a reference and calculating the deviation of the beams from the measurement plane normal at $z = 70$ mm, one finds that

$$\delta h_{HF,a} = z c_0 \frac{\Delta t_{HF,a}}{\Delta s_{HF,a}} = 337 \mu\text{m} \quad (\text{H.2})$$

$$\delta h_{HF,e} = z c_0 \frac{\Delta t_{HF,e}}{\Delta s_{HF,e}} = 1200 \mu\text{m} \quad (\text{H.3})$$

$$\delta h_{LF,a} = z c_0 \frac{\Delta t_{LF,a}}{\Delta s_{LF,a}} = 593 \mu\text{m} \quad (\text{H.4})$$

$$\delta h_{LF,e} = z c_0 \frac{\Delta t_{LF,e}}{\Delta s_{LF,e}} = 337 \mu\text{m} \quad (\text{H.5})$$

A difference in the alignment of the HF and LF beams which is less than 1 mm at a depth of 70 mm should be insignificant with respect to the development of non-linear effects, due to the width of the LF beam.

H.2 LF RMS Pressure Profiles

The development of the LF RMS beam profiles of *Skolmen* with depth are shown in Fig. H.3 through Fig. H.5. The measurements were taken in order to assess whether or not element in the centre of the array were malfunctioning when excited by the LF pulser. Figure G.14, which shows the azimuth beam profiles of single elements, verified that the elements were functioning properly individually, but the somewhat strange profile of Fig. G.11 was cause enough to check that all the elements were functioning together as well.

According to the Fraunhofer approximation, a malfunctioning element can be detected by studying the far-field or focal beamprofile of an array. If an element is not working, the azimuth profile should exhibit some sinusoidal component in addition to the expected sinc characteristic. Studying the profile in Fig. H.5, one can see that this is not the case for the LF array. In azimuth and elevation, the profiles are smoothed, almost gaussian-looking, sinc functions, as one would expect from a pulsed wave emanating from a rectangular source [58]. The figures thus support the conclusion that the LF array does not have any malfunctioning elements in the centre of the array.

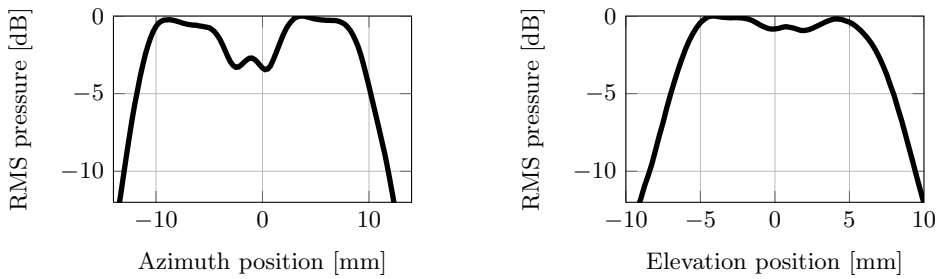


Figure H.3: The beam profiles of the LF array, at a depth of 0 mm

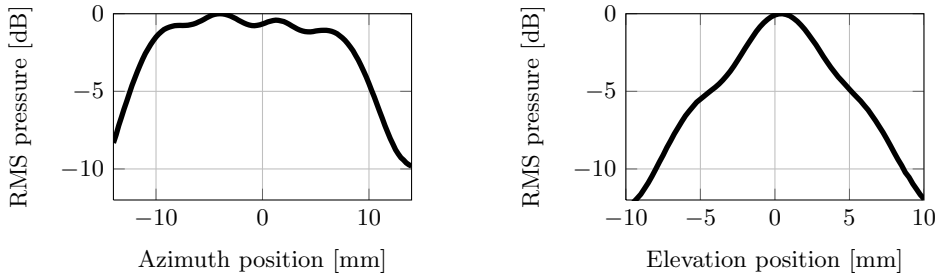


Figure H.4: The beam profiles of the LF array, at a depth of 20 mm

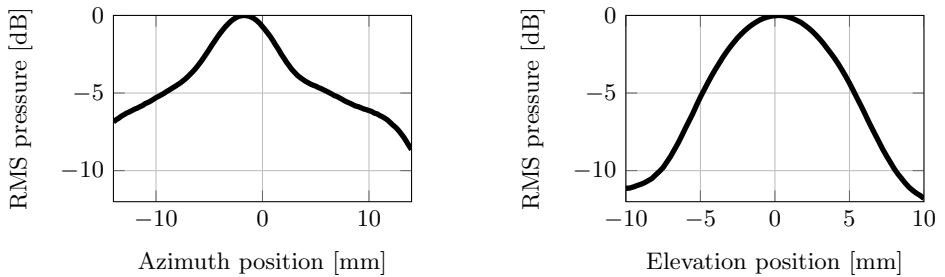


Figure H.5: The beam profiles of the LF array, at a depth of 40 mm